PHOTORESIST-BASED POLYMER RESONATOR ANTENNAS (PRAS) WITH LITHOGRAPHIC FABRICATION AND DIELECTRIC RESONATOR ANTENNAS (DRAS) WITH IMPROVED PERFORMANCE

A Thesis Submitted to the College of
Graduate Studies and Research
In Partial Fulfillment of the Requirements
For the Degree of Doctor of Philosophy
In the Department of Electrical and Computer Engineering
University of Saskatchewan
Saskatoon

By

Atabak Rashidian

April 2011

Permission to Use

In presenting this thesis in partial fulfilment of the requirements for a Postgraduate degree from the University of Saskatchewan, I agree that the Libraries of this University may make it freely available for inspection. I further agree that permission for copying of this thesis in any manner, in whole or in part, for scholarly purposes may be granted by the professor or professors who supervised my thesis work or, in their absence, by the Head of the Department or the Dean of the College in which my thesis work was done. It is understood that any copying or publication or use of this thesis or parts thereof for financial gain shall not be allowed without my written permission. It is also understood that due recognition shall be given to me and to the University of Saskatchewan in any scholarly use which may be made of any material in my thesis.

Requests for permission to copy or to make other use of material in this thesis in whole or part should be addressed to:

Head of the Department of Electrical and Computer Engineering
University of Saskatchewan
Saskatoon, Saskatchewan, Canada
S7N 5A9

To the memory of my father, Hossein
who taught me to never stop learning

to my mother, Fatemeh

and to my wife and daughter, Zohreh and Athena

Abstract

The demand for higher bit rates to support new services and more users is pushing wireless systems to millimetre-wave frequency bands with more available bandwidth and less interference. However at these frequencies, antenna dimensions are dramatically reduced complicating the fabrication process. Conductor loss is also significant, reducing the efficiency and gain of fabricated metallic antennas. To better utilize millimetre-wave frequencies for wireless applications, antennas with simple fabrication, higher efficiency, and larger impedance bandwidth are required.

Dielectric Resonator Antennas (DRAs) offer many appealing features such as large impedance bandwidth and high radiation efficiency due to the lack of conductor and surface wave losses. DRAs also provide design flexibility and versatility. Different radiation patterns can be achieved by different geometries or resonance modes, wideband or compact antennas can be provided by different dielectric constants, and DRAs can be excited by a wide variety of feeding structures. Nevertheless, compared to their metallic counterparts, fabrication of DRAs is challenging since they have traditionally been made of high permittivity ceramics, which are naturally hard and extremely difficult to machine and cannot be easily made in an automatic way. The fabrication of these three dimensional structures is even more difficult at millimetre-wave frequencies where the size of the antenna is reduced to the millimetre or sub-millimetre range, and tolerances to common manufacturing imperfections are even smaller. These fabrication problems restrict the wide use of DRAs, especially for high volume commercial applications.

A new approach to utilize the superior features of DRAs for commercial applications, introduced in this thesis, is to exploit polymer-based resonator antennas (PRAs), which dramatically simplifies fabrication due to the natural softness and results in a wide impedance bandwidth due to the low permittivity of polymers. Numerous polymer types with exceptional characteristics can be used to fulfill the requirements of particular applications or achieve extraordinary benefits. For instance, in this thesis photoresist polymers facilitate the fabrication of PRAs using lithographic processes. Another advantage derived from this approach is the capability of mixing polymers with a wide variety of fillers to produce composite materials with improved or extraordinary characteristics.

The key contributions of this thesis are in introducing SU-8 photoresist as a radiating material, developing three lithographic methods to fabricate photoresist-ceramic composite structures, introducing a simple and non-destructive measurement method to define electrical properties of the photoresist composites, and demonstrating these structures as improved antenna components.

It is shown that pure SU-8 resonators can be highly efficient antennas with wideband characteristics. To achieve more advantages for RF applications, the microwave properties of photoresists are modified by producing ceramic composite materials. X-ray lithography fabrication is optimized and as a result one direct and two indirect methods are proposed to pattern ultra thick (up to 2.3 mm) structures and complicated shapes with an aspect ratio as high as 36:1. To measure the permittivity and loss tangent of the resulting materials, a modified ring resonator technique in one-layer and two-layer microstrip configurations is developed. This method eliminates the requirement to metalize the samples and enables characterization of permittivity and dielectric loss in a wide frequency range from 2 to 40 GHz. Various composite PRAs with new designs (e.g. frame-based and strip-fed structures) are lithographically fabricated, tested, and discussed. The prototype antennas offer -10 dB bandwidths as large as 50% and gain in the range of 5 dBi.

Acknowledgements

I would like to thank my supervisor, Professor David M. Klymyshyn for his support, encouragement, and guidance throughout this work. I would also like to thank my committee members, especially Professor Sven Achenbach for their valuable comments.

I thank the personnel at the Institut für Mikrostrukturtechnik (IMT), Forschungszentrum Karlsruhe in Germany, especially Dr. Martin Boerner for all their guidance and efforts supporting lithography fabrication during my stay in Germany.

Also, I would like to thank TRLabs for providing financial support for this project. I wish to express my appreciation to Mr. Garth Wells of the Canadian Light Source (CLS) for his assistance during the experiments.

Finally, a special thank is given to my family and my dear friend, Mohammadreza Tayfeh Aligodarz for their support and encouragement.

Contents

List of Tables

List of Figures

List of Abbreviations

ANKA	Angstroemquelle Karlsruhe
Be	Beryllium
BPO	benzoyl peroxide
BW	bandwidth
CDRA	cylindrical dielectric resonator antenna
CPW	coplanar waveguide
dB	decibel
DMA	dimethylaniline
DRA	dielectric resonator antenna
DWM	dielectric waveguide model
EDC	effective dielectric constant
ESEM	environmental scanning electron microscope
FDTD	finite difference time domain
FEM	finite element method
FIT	finite integration technique
GeV	giga electron volt
GHz	gigahertz
HEM	hybrid electromagnetic
HFSS	high frequency structure simulator
HV	high vacuum
LCP	liquid crystal polymer
MEMO	Methacryloxypropyl Trimethoxy Silane
mm	millimetre
MMA	Methylmethacrylate
MMIC	monolithic microwave integrated circuit
PDMS	Polydimethylsiloxane

PEC	perfect electric conductor
PGMEA	Propylene Glycol Monoether Acetate
PMMA	Polymethylmethacrylate
POM	Polyoxymethylene
PRA	polymer resonator antennas
Q	quality factor
Q_D	dielectric quality factor
Q_U	unloaded quality factor
SEM	scanning electron microscope
SOLT	short-open-load-through
T	Tesla
TE	transverse electric
Ti	Titanium
TM	transverse magnetic
TSDRA	two segmented dielectric resonator antenna
UHV	ultra high vacuum
UV	ultraviolet

Chapter 1

Introduction

1.1 Motivation

Dielectric Resonator Antennas (DRAs) are attractive candidates for a wide variety of wireless applications from military to medical usages, from low frequency to very high frequency bands, and from on chip to large array applications [1-8]. These advancements are due to both intrinsic appealing features of DRAs and efforts which have been done to intensify these features since their first appearance in 1983 [9]. DRAs provide, compared to other low gain or small metallic structure antennas, larger impedance bandwidth, compact size, good mechanical stability, and higher radiation efficiency due to the lack of surface wave and conductor losses. A typically designed DRA with dielectric constant of 10 offers around 10 percent impedance bandwidth while a typical microstrip metallic patch antenna provides a few percent impedance bandwidth at most. The overall size of DRAs can be significantly reduced by $\varepsilon_r^{-1/2}$, where ε_r is the dielectric constant of the resonator material. Therefore, very compact antennas can be achieved by choosing a high value of ε_r. The higher radiation efficiency of DRAs is especially attractive for millimetre-wave applications, where the loss in metal fabricated antennas is significant. Fig. 1.1 shows the impact of dielectric loss on DRA performance. The antenna efficiency varies from 98% for extremely low loss materials to 91% for medium loss materials. The radiation efficiency of the medium loss DRA is still better than the radiation efficiency of microstrip patch antennas which is typically around 80% [10]. DRAs also offer design flexibility and versatility. Different radiation patterns can be achieved by different

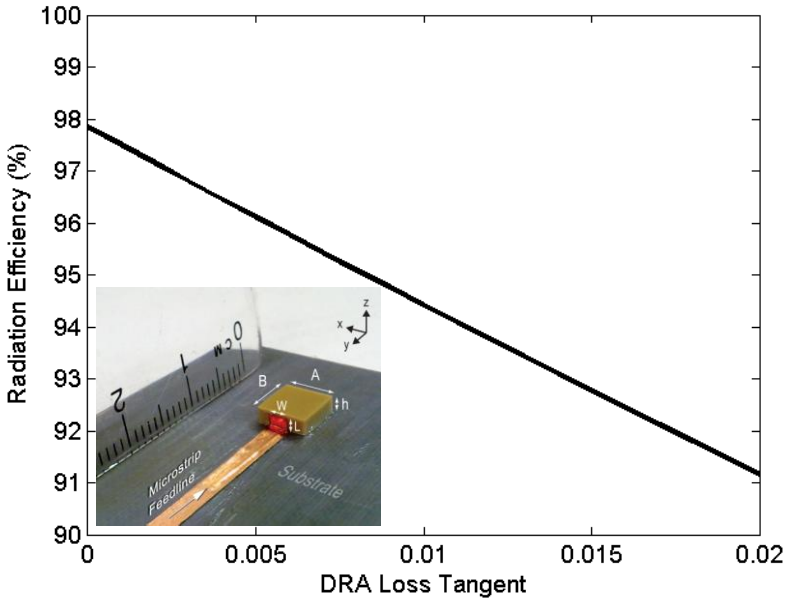

Fig. 1.1. Simulated radiation efficiency of a strip-fed DRA with different dielectric loss tangents at around 30 GHz.

geometries or resonance modes, wideband or compact antennas can be provided by different dielectric constants, and DRAs can be excited by a wide variety of feeding structures.

Despite all the superior properties of DRAs, the microstrip antennas are the most extensively used antennas for low-gain microwave and millimetre-wave applications [11]. The microstrip antenna consists of a metallic strip/patch placed above a grounded substrate and usually fed through a coaxial probe or an aperture. The large popularity of the microstrip antenna is due to this fact that it is inexpensive to manufacture using modern printed-circuit technology. In comparison, DRAs involve a more complex and costly fabrication process. While microstrip patch antennas can be produced in various complicated shapes by lithographic processes, DRAs are mostly limited to simple structures (e.g. rectangular and circular shapes). Batch fabrication, for instance by cutting machines, is questionable since the hardness of ceramic is comparable to the diamond cutting blades. Array structures are even more difficult to fabricate due to the requirement of individual element placement and bonding to the substrate. The problems become worse at millimetre-wave frequencies where the size of the

antenna is reduced to the millimetre or sub-millimetre range, and tolerances to common manufacturing imperfections are even smaller. In fact, fabrication of DRAs is challenging since they have traditionally been made of high permittivity ceramics, which are naturally hard and extremely difficult to machine and cannot be easily made in an automatic way. These fabrication problems restrict the wide use of DRAs, especially for high volume commercial applications.

A new approach to utilize the superior features of DRAs for commercial applications is to explore polymer-based resonator antennas (PRAs), which dramatically simplifies fabrication due to the natural softness and results in wide impedance bandwidth due to the very low permittivity of polymers. A PRA with dielectric loss tangent around 0.02 has more than 90 percent radiation efficiency, as shown in Fig. 1.1, and since its dielectric constant is more than 1, it involves miniaturization, although this tends to be less important at millimetre-wave frequencies. Polymers can be used with a wide variety of fillers to produce polymer composites. If properly mixed, these composites offer extraordinary performances which can be attributed to the polymer or to the filler and some to the polymer and filler interaction. For instance, inhomogeneous distribution of fillers can be used to make electrically anisotropic structures and special features of polymers (e.g. flexibility [12]) can be utilized for particular applications. If photosensitive polymers are used, the lithographic fabrication process can be performed to demonstrate antenna structures with precise features.

Over several decades, photolithography has evolved to enable fabrication of passive devices with small features. But extension of this technique to fabricate high performance passive microwave components, which typically account for more than 75% of circuit elements in wireless transceivers [13], has been hindered since the penetration depth of UV light is not sufficient for patterning tall structures in thick materials. While thick structures can improve the performance of various metallic components (e.g. by making tall, low-loss compact structures [14]), it is a necessity for dielectric components which are especially attractive at

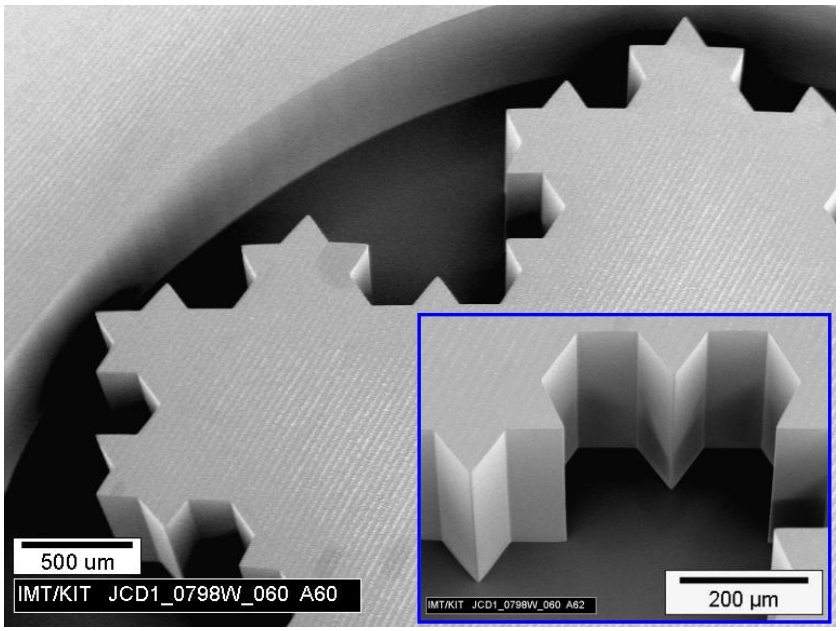

Fig. 1.2. SEM micrographs of a third order Koch Island fractal structure fabricated with deep X-ray lithography. The 1.8 mm-thick polymer-based antenna element has excellent sidewall verticality better than 89.7° and roughness in the order of 26 ± 12 nm. The inset shows details of the sidewall structure [18].

millimeter-wave frequencies due to the absence of surface currents and metallic loss but difficult to fabricate due to their tiny structures and three dimensionality. One potential solution to overcome this problem and batch fabricate high precision DRAs is X-ray lithography.

X-ray lithography is a technique that utilizes synchrotron radiation to build 3D structures with height up to a few millimetres and minimum structural detail in the micrometer range [15-17]. Compared to other techniques (e.g. UV lithography), X-ray lithography can produce much taller structures (up to a few millimetres) with better sidewall verticality and finer features, and has introduced many improvements in the area of microfabrication. Fig. 1.2 shows a representative scanning electron microscope (SEM) image of a newly developed polymer-based fractal antenna element, demonstrating the capability of X-ray lithography in fabrication of high quality miniature structures. Although this technique has been used to fabricate capacitors, filters, transmission lines, cavity resonators, and couplers in the past [14, 19-24], no research was reported for structuring dielectric antennas.

1.2 X-ray Lithography Processing

X-ray lithography uses more energetic and higher frequency radiation than more traditional optical lithography to produce very tall structures with minimum dimension sizes smaller than a micron. The most efficient way to create this radiation is by a ring of accelerated relativistic electrons named a synchrotron or electron storage ring, although research to develop new and simple light sources is in progress [25]. The essential steps in the X-ray lithography fabrication include coating the photoresist material on a substrate, exposing the synchrotron radiation through a mask, and developing the material by an appropriate solvent or developer. X-ray lithography is the first step of the LIGA process. The electroforming of metals and moulding of plastics are the following steps in the complete LIGA process, all of which is not necessarily applicable for producing dielectric structures. The acronym LIGA is derived from the German words of lithographie, galvanoformung, and abformung which are respectively equivalent to lithography, electrodeposition, and moulding in English. The process was developed during the 1980's at the Nuclear Research Center (later Research Center Karlsruhe, Forschungszentrum Karlsruhe), in Karlsruhe, Germany, in order to be able to produce very small and precise separation nozzles for uranium isotopes [26].

X-ray lithography fabrication is a complicated process which must be modified and optimized for different material and structural requirements. Therefore, all steps and their special adjustments should be carefully determined. Preparing a suitable material is very important and has a great impact on the fabrication process. The material should satisfy electrical properties requirements for antenna applications and properties required for X-ray lithography fabrication. Two important electrical characteristics of each material are permittivity and dielectric loss. To be attractive for antenna applications, materials should have a dielectric loss as low as possible. Usually values less than 0.02 for loss tangent

will result in more than 90% radiation efficiency for antennas. The useful material permittivity is considered to be between 8 and 100 depending on applications; however, we show in the present research that permittivity as low as 4 can also be used to fabricate dielectric antennas with improved performance [18, 27-28]. To be recognized as an attractive material for X-ray lithography microfabrication, a material should satisfy many requirements. Some of these requirements are that its deposition process should be as simple as possible and sensitive to X-rays so that it will be easily patterned. Regarding electrical and microfabrication requirements, two groups of materials can be used in the fabrication process.

Pure photoresist materials, which are ideal for X-ray lithography fabrication but perhaps not optimal for antenna applications, are considered as the first group. Two photoresist materials are primarily used in X-ray lithography applications, Polymethylmethacrylate (PMMA) and Epon SU-8.

PMMA is a positive one-component resist used in electron beam and X-ray lithography. Although it has poor sensitivity requiring high exposure doses to be patterned, its selectivity (contrast) with specific developers is very high resulting in excellent structure quality. Very thick PMMA layers can be applied to a substrate by gluing. However, patterning thick layers requires very deep X-rays and special adjustments for beamline mirrors and filters. Too little absorption in the ultraviolet range makes PMMA unattractive for optical lithography. Meanwhile, excellent optical transparency in the visible light range, has made this material ideal for micro-optics applications [29].

Initial measurements of electrical properties of PMMA are shown in Fig. 1.3. Although the loss is always kept under 0.01, the maximum permittivity is less than 2.8 for all frequencies between 10 and 1500 MHz. The very low permittivity of this material is the main drawback in dielectric antenna applications. The test setup used to obtain Fig. 1.3 is based on parallel plate capacitance measurement. Electrical properties higher than 1.5 GHz could not be measured, and therefore a new setup should be developed to measure higher frequencies.

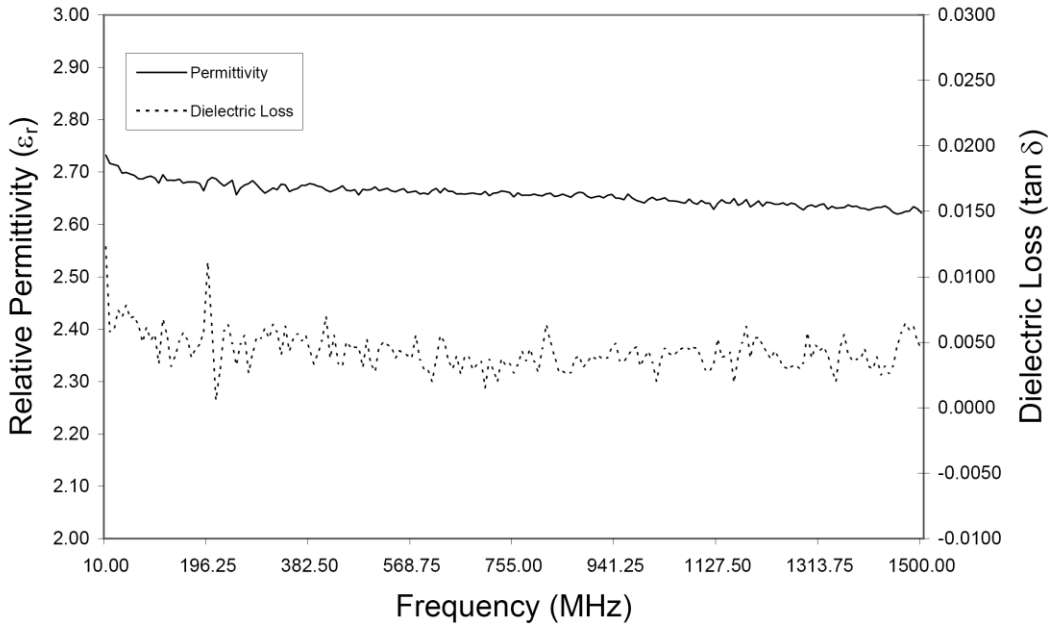

Fig. 1.3. Measured electrical properties of PMMA.

Epon SU-8 is a negative three-component resist used in ultraviolet and X-ray lithography. This material has a maximum sensitivity between λ = 350 and 400 nm. Since very low exposure doses are required due to its chemical amplification, it is also applicable to other wavelengths including X-ray wavelengths in the range of λ = 0.01 to 10 nm. Very thick layers of Epon SU-8 can be cast or spincoated in multiple steps due to its high viscosity. However, side effects like T-topping as a result of unwanted dose contributions at the resist top, stress induced by shrinking during crosslinking, and incompatibility with electroplating have limited its applications.

Different values for the dielectric properties of SU-8 have been reported in the existing literature [30-33]. For instance, the dielectric constant of SU-8 is measured to be around 4 in [30], 3.3 in [32], and 2.8 in [33]. These variations in electrical properties are likely due to several factors, including different commercial types of SU-8 [34] (e.g. SU-8(5), SU-8(10), SU-8(100), etc.) used in the fabrication process, pre-bake and post-bake conditions (e.g. time and temperature), and exposure dose. Extensive electrical measurements and careful

selection of an appropriate kind of Epon SU-8 along with designing fabrication steps and their special adjustments are necessary before performing the fabrication.

The photoresist materials are not optimal for microwave and antenna applications and it is desirable to improve their electrical properties. For instance, micro and nano microwave materials (e.g. micropowder ceramics) can be added to low viscous photoresist/polymer materials in a direct or an indirect (i.e. micro powder injection moulding) fabrication process. Therefore, the second group of viable materials is photoresist/polymer composites which have been produced using microwave micro and nano fillers. In this case the material may not be ideal for X-ray lithography fabrication and additional steps or special adjustments may be required.

In the direct fabrication process, microstructure components have been made by X-ray lithography without an intermediate moulding step. A new process sequence has to be evaluated for the photoresist composite materials. As a direct consequence of increasing material viscosity due to adding fillers, for instance, a new coating technique should be developed. Moreover, in order to pattern the composite material and find an appropriate bottom dose, special consideration of X-ray absorption is required for the exposing step. This widely depends on the type and quantity of filler, as well as the size of particles. In the indirect fabrication process, mould inserts are made by exposing pure photoresist using X-ray lithography. Subsequently, the polymer composite material is injected into the cavity. Demoulding can be performed at the end of process to produce final structures.

Various research has been previously reported on X-ray lithography fabrication of microstructures using composite materials [35-37]. All of these approaches are complicated by the requirement for debinding and sintering to make pure metallic or ceramic structures from composite materials for harsh environment applications where the hardness of metal or ceramic is required. The thickness of structures is

mainly limited to a few hundred microns and debinding and sintering steps are the main reasons for degradation of the final structures. Since most of these works have not involved microwave applications, only a few groups have evaluated electrical properties of composite materials, mostly in low frequencies.

There is a trade-off between the sintering step and other steps in the fabrication process. To have successful sintering a high portion of filler content (more than 70 wt%) should be added to the polymer (or photoresist) material. Due to increased viscosity and decreased sensitivity of the resulting material, this leads to problems in mixing, casting, and exposure steps in direct lithography methods, and problems in the mixing, moulding, and demoulding steps in indirect methods such as powder injection moulding. On the other hand, lowering the amount of filler content to avoid these problems creates cracks and shrinkages in the final structure during the sintering step. For antenna and microwave applications where the electrical properties (not the mechanical properties) of the material are the first priority, it is feasible to correct these properties by adding micro or nano materials to the photoresist/polymer material and maintain the high quality of the final structures by avoiding debinding and sintering steps. This also allows the fabrication of polymer composite components along with other circuit elements (e.g. transmission lines and feeding systems) on a common substrate since the high temperature applied in the sintering step, which could damage or distort non-ceramic circuit elements due to the thermal expansion mismatch, is no longer required.

1.3 Thesis Objectives

The feasibility of X-ray lithography for batch fabrication of dielectric antenna structures with improved performance characteristics is investigated in this research. The specific objectives are divided into three main parts; improving antenna performance characteristics, investigating viable fabrication processes and materials, and introducing and testing novel antennas.

Improving antenna performance characteristics, as the first part, not only introduces ideas to improved antenna performance but also is a prerequisite for X-ray lithography fabrication of proposed antennas. In fact, the improvements are mostly achieved by considering properties enforced and/or enabled by X-ray lithography fabrication, and therefore improved antenna structures suitable for X-ray lithography fabrications are attained. In this part, the focus is on the investigation, design, and analysis of various DRA configurations exhibiting enhanced performance by either altering the geometry (e.g. high aspect ratio structures) or material properties (e.g. very low permittivity photoresists).

The objective of the second part of this research is to investigate materials and develop a fabrication process. For material research, electrical properties and properties required for X-ray lithography fabrication should be examined. This includes preparing different polymer composites, measuring electrical properties up to 40 GHz, exposing materials to X-ray radiation to analyze exposure parameters and problems, and modifying the materials to either improve the antenna performance or facilitate the microfabrication process. For the fabrication part, the number of essential steps in the process and the adjustments of each step should be determined for different materials, structures and sizes.

Finally, testing the resulting structures is performed to introduce novel antennas. This involves determination of the antenna characteristics, and comparing them with the simulation results. Discussions and conclusions on radiation characteristics and impedance properties are provided for different antennas having different materials and fabrication processes.

1.4 Thesis Organization

The organization of this thesis is as follows.

Chapter 2 presents the basic theory of DRAs. The operation and the properties of the cylindrical and rectangular dielectric resonator antennas are examined, their modes are classified and their resonance frequencies and radiation *Q*-factors are

determined based on approximation models. Near field distributions of different modes are shown and used to predict the far field radiation patterns. The most commonly-used feeding schemes are reviewed and the coupling mechanisms to the various DRA modes are discussed.

Chapter 3 provides several solutions to improve DRA performance. These solutions exploit high-aspect-ratio high-permittivity, anisotropic (multisegment), slot-fed low-permittivity, and strip-fed low-permittivity dielectric structures to show antennas with enhanced performance. Theories of the proposed solutions are discussed and detailed parametric studies of the resulting antennas are given. In some cases measurements of fabricated prototypes are provided and compared with Ansoft HFSS^{TM} simulation results. Comparisons and discussions on miniaturization, bandwidth enhancement, near field distributions, and far field radiation patterns are presented.

In Chapter 4, direct and indirect X-ray lithography fabrication methods are proposed using both positive (PMMA) and negative tone (SU-8) resists to produce polymer composite antenna structures. In the direct fabrication method the structures are lithographically fabricated avoiding an intermediate molding step. In the indirect fabrication methods a very precise plastic frame is produced by X-ray lithography and filled with polymer/photoresist composites. The plastic frame can remain in the final structure or be removed at the end of process. The resulting antennas are examined regarding their structural qualities using an environmental scanning electron microscope (ESEM). Optimized fabrication parameters allow for the production of high quality antenna structures as thick as 2.3 mm.

In Chapter 5, a new technique is developed to measure electrical properties of the photoresist composite materials. The technique utilizes a combination of a one-layer and two-layer microstrip ring resonator measurement. Microstrip ring resonators with different characteristics are designed and fabricated on microwave substrates with known electrical properties. Photoresist composite slabs are

prepared and superimposed on the microstrip ring resonators to construct a two-layer microstrip structure. The differences in *Q* factor and resonant frequency before and after slab insertion are used to determine the dielectric constant and loss tangent of the photoresist composite slabs. This method eliminates the requirement to metalize the samples and enables characterization of permittivity and dielectric loss in a wide frequency range from 2 to 40 GHz. Discussions on electrical properties of the photoresist composites are provided and the accuracy of the measurement technique are validated using two standard methods (cavity resonator and long stripline methods).

Chapter 6 investigates the radiation properties and impedance characteristics of lithographically patterned pure photoresist and photoresist composite resonator antennas. A plastic resonator antenna fabricated using bulk SU-8 photoresist is realized. Strip-fed and slot-fed SU-8/alumina composite antennas are introduced, measured and their characteristics are discussed when the amount of ceramic (alumina) is changed. The effects of dielectric loss on antenna efficiency and gain are addressed. Impedance bandwidths are examined by merging resonances of different appropriate modes of the polymer-based resonators and/or an aperture antenna. Finally, a PMMA composite antenna having permanent plastic frame is tested and the impact of plastic frame on antenna properties is investigated.

Chapter 7 concludes the work, summarizes the most important achievements of this thesis, and provides several suggestions for future work.

References

[1] P. V. Bijumon, Y. M. M. Antar, A. P. Freundorfer, and M. Sayer, "Integrated dielectric resonator antennas for system on-chip applications," *IEEE Int. Conf on Microelectronics*, pp. 275-278, December 2007.

[2] Z. Wang, S. Kamalraj, C. C. Chiau, X. Chen, B. S. Collins, and S. P. Kingsley, "Dual-band dielectric antenna for WLAN applications," *IEEE Int. workshop on antenna technology*, pp. 151-154, March 2007.

[3] I. A. Eshrah, A. A. Kishk, A. B. Yakovlev, and A. W. Glisson, "Dielectric resonator antenna excited by waveguide slot for radar applications," *IEEE Int. Antennas and Propagation Symposium (AP-S)*, pp. 492-495, 2003.

[4] M. Rotaru, L. Y. Ying, H. Kuruveettil, Y. Rui, A. P. Popov, and C. Chee-Parng, "Implementation of packaged integrated antenna with embedded front end for bluetooth applications," *IEEE Transactions on Advanced Packaging*, vol. 31, no. 3, pp. 558-567, August 2008.

[5] J. Svedin, L. G. Huss, D. Karlen, P. Enoksson, and C. Rusu, "A micromachined 94 GHz dielectric resonator antenna for focal plane array applications," *IEEE Int. Microwave Symposium*, pp. 1375-1378, June 2007.

[6] O. Oestreich, A. Lambrecht, J. Pontes, and W. Wiesbeck, **"**Dually polarized DRAs for UMTS applications," *IEEE Int. Antennas and Propagation Symposium (AP-S)*, pp. 545-548, June 2007.

[7] H. Wei and A. A. Kishk, "Compact dielectric resonator antenna array for microwave breast cancer detection," *IEEE Region 5 Technical Conf.*, pp. 9-12, 2007.

[8] A. Lambrecht, O. Oestreich, J. Pontes, and W. Wiesbeck, "Dielectric resonator antennas for polarization diversity in base station array applications," *IEEE Int. Conf on Electromagnetics in Advanced Applications*, pp. 527-530, 2007.

[9] S. A. Long, M. McAllister and L. C. Shen, "The resonant cylindrical dielectric cavity antenna," *IEEE Transactions on Antennas and Propagation*, vol. AP-31, pp. 406-412, May 1983.

[10] Q. Lai, G. Almpanis, C. Fumeaux, H. Benedickter, and R. Vahldieck, "Comparison of the radiation efficiency of the dielectric resonator antenna and microstrip antenna at Ka band," *IEEE Transactions on Antennas and Propagation*, vol. 56, no. 11, pp. 3589-3592, November 2008.

[11] C. A. Balanis, Antenna Theory: Analysis and Design. New Jersey: Wiley, 2005.

[12] S. Koulouridis, G. Kiziltas, Z. Yijun, D. J. Hansford, and J. L. Volakis, "Polymer-ceramic composites for microwave applications: fabrication and performance assessment," *IEEE Trans. Microw. Theory Tech.*, vol. 54, no. 12, pp. 4202-4208, Dec. 2006.

[13] H. J. De Los Santos, G. Fischer, H. A. C. Tilmans, and J. T. M. Van Beek, "RF MEMS for ubiquitous wireless connectivity: part 2-applications," *IEEE Microwave Magazine*, vol. 5, no. 4, pp. 50-65, Dec. 2004.

[14] A. Kachayev, D. M. Klymyshyn, S. Achenbach, and V. Saile, "High vertical aspect ratio LIGA microwave 3-dB coupler," *Int. Conf on MEMS, NANO, and Smart Systems*, pp. 38-43, 2003.

[15] E. Spiller, "Early history of X-ray lithography at IBM," *IBM J. RES. DEVELOP.*, vol. 37, no. 3, pp. 291-297, May 1993.

[16] W. Menz, J. Mohr, and O. Paul, *Microsystem Technology*. Weinheim: Wiley-VCH, 2001.

[17] Mark J. Madou, Fundamentals of Microfabrication: the Science of Miniaturization. Boca Raton, FL: CRC Press, 2002.

[18] A. Rashidian, D. M. Klymyshyn, M. Tayfeh Aligodarz, M. Boerner, and J. Mohr, "Characterization of photoresist-based microcomposites for polymer resonator antennas," to be submitted to *IEEE Transactions on Antennas and Propagation*.

[19] D. M. Klymyshyn, H. C. Jayatilaka, M. Boerner, and J. Mohr, "High-aspect-ratio coplanar waveguide wideband bandpass filter with compact unit cells," *IEEE Trans. Microw. Theory Tech.*, vol. 57, no. 11, pp. 2753-2760, Nov. 2009.

[20] T. L. Willke and S. S. Gearhart, "LIGA micromachined planar transmission lines and filters," *IEEE Trans. Microw. Theory Tech.*, vol. 45, no. 10, pp. 1681-1688, Oct. 1997.

[21] Z. Ma, D. M. Klymyshyn, S. Achenbach, M. Börner, N. Dambrowsky, and J. Mohr, "An ultra-deep high-Q microwave cavity resonator fabricated using

deep X-ray lithography," *IEICE Trans. Electron.*, vol. E90-C, no. 12, pp. 2192-2197, Dec. 2007.

[22] D. M. Klymyshyn, D. T. Haluzan, M. Boerner, S. Achenbach, J. Mohr, and T. Mappes, "High aspect ratio vertical cantilever RF-MEMS variable capacitor," *IEEE Microwave & Wireless Component Letters*, vol. 17, no. 2, pp. 127-129, 2007.

[23] D. M. Klymyshyn, M. Boerner, D. T. Haluzan, E. G. Santosa, M. Schaffer, S. Achenbach, and J. Mohr, "Vertical high-*Q* RF-MEMS devices for reactive lumped-element circuits," *IEEE Trans. Microw. Theory Tech.*, vol. 58, no. 11, pp. 2976-2986, Nov. 2010.

[24] M. A. Forman, "Low-loss LIGA-fabricated coplanar waveguide and filter," *Asia-Pacific Microwave Conf*, pp. 1905-1907, 2006.

[25] S. R. Das, "A new light source for EUV lithography," *IEEE Spectrum*, p. 14, March 2008.

[26] E. W. Becker, W. Ehrfeld, D. Munchmeyer, H. Betz, A. Heuberger, S. Pongratz, W. Glashauser, H. J. Michel, and V. R. Siemens, "Production of separation nozzle systems for uranium enrichment by a combination of X-ray lithography and galvanoplastics," *Naturwissenschaften*, vol. 69, pp. 520-523, 1982.

[27] A. Rashidian, D. M. Klymyshyn, M. Tayfeh Aligodarz, M. Boerner, and J. Mohr, "Photoresist-based polymer resonator antennas: lithography fabrication, strip-fed excitation, and multimode operation," *IEEE Antennas and Propagation Magazine*, Accepted for publication Nov. 27, 2010.

[28] A. Rashidian, D. M. Klymyshyn, M. Tayfeh Aligodarz, M. Boerner, and J. Mohr, "Development of polymer-based dielectric resonator antennas for millimeter-wave applications," *Progress In Electromagnetics Research C (PIER C)*, vol. 13, pp. 203−216, 2010.

[29] Y. B. Gianchandani, O. Tabata, and H. Zappe, *Comprehensive Microsystems*. Elsevier, 2008.

[30] J. R. Thorpe, D. P. Steenson, and R. E. Miles, "High frequency transmission line using micromachined polymer dielectric," *IET (IEE) Electronics Letters*, vol. 34, no. 12, pp. 1237-1238, June 1998.

[31] R. Osorio, Micromachined transmission lines for microwave applications, Ph.D. dissertation, Freiburg University, Germany, 2003.

[32] F. D. Mbairi and H. Hesselbom, "High frequency design and characterization of SU-8 based conductor backed coplanar waveguide transmission lines," *Proceeding of International Symposium on Advanced Packaging Material: Processes, Properties, and Interfaces,* pp. 243-248, March 2005.

[33] A. Ghannam, C. Viallon, D. Bourrier, and T. Parra, "Dielectric microwave characterization of the SU-8 thick resin used in an above IC process," *Proceedings of the 39th European Microwave Conference*, Rome, Italy, pp. 1041-1044, September 2009.

[34] MicroChem Corporation, USA, webpage http://www.microchem.com.

[35] T. Gietzelt, V. Piotter, R. Ruprecht, and J. Hausselt, "Manufacturing of isolated ceramic microstructures," *Microsystem Technologies*, no. 9, pp. 99-103, 2002.

[36] C. Muller, T. Hanemann, G. Wiche, C. Kumar, and J. Goettert, "Fabrication of ceramic microcomponents using deep X-ray lithography," *Microsystem Technology*, no. 11, pp. 271-277, 2005.

[37] L. Merz, S. Rath, V. Piotter, R. Ruprecht, and J. Hausselt "Powder injection molding of metallic and ceramic microparts," *Microsystem Technology*, no. 10, pp. 202-204, 2004.

Chapter 2

Dielectric Resonator Antennas

Unshielded dielectric resonators are potentially beneficial antenna elements [1]. They provide appealing features such as high radiation efficiency due to the lack of surface wave and conductor losses, simple structure, capability of integration with MMICs, wide impedance bandwidth and compact size. Different modes having specific internal and associated external field distribution can be excited in dielectric resonator antennas (DRAs). These modes result in various antenna characteristics and radiation patterns for a wide variety of applications. The first systematic theoretical and experimental investigation on a specific DRA by Long et al. in 1983 was a beginning for numerous research to introduce and intensify DRA characteristics [2]. The most popular shapes studied for practical antenna applications in the literature have been the cylindrical and rectangular geometries. Approximate analytical solutions, developed for these structures, have been a base to analyze more complicated antennas (e.g. multisegment structures). However, to achieve more accurate results, estimate input impedance and radiation patterns, and predict the effects of feeding mechanisms on DRA performance, numerical techniques should be used.

In this chapter, general facts and principles on dielectric resonators are reviewed in order to understand how these structures operate. Cylindrical and rectangular DRAs are analyzed based on these principles. The resonant frequencies and radiation Q-factors of fundamental modes are derived. The near fields and radiation characteristics are discussed. In addition, commonly used schemes for excitation of DRAs are discussed.

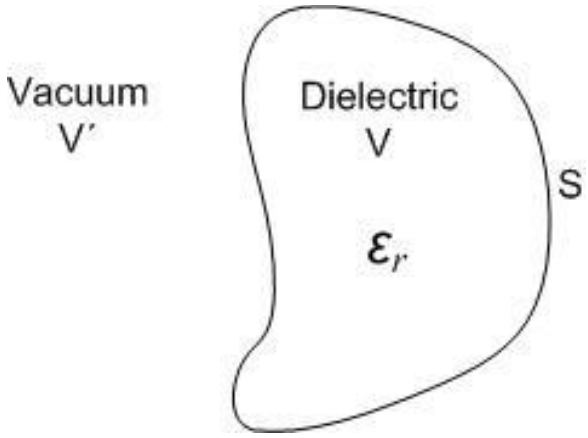

Fig. 2.1. Structure of an arbitrary shape dielectric resonator excited by an electric current source.

2.1 Basic Principles of Dielectric Resonators

An exact solution for dielectric resonators exists for only simple shapes, e.g. the spherical geometries, for which separation of variables is possible. For a dielectric resonator of arbitrary shape, general conclusions can be achieved to approximately find the solutions. Most of these conclusions are based on the fundamental work of Van Bladel and are summarized here [3-4].

Fig. 2.1 shows an isolated arbitrary shape dielectric resonator excited by an electric current source. It is proven that even if the permittivity is considered infinity the boundary surface *S* does not generally behave as a magnetic wall in which the tangential components of the magnetic field and the normal components of the electric field are equal to zero. As a result, electromagnetic waves penetrate into the vacuum region (V'), even for ε_r equal to infinity. It might be also concluded that the electromagnetic fields are confined in the vicinity of the resonator and they decrease exponentially with distance from the resonator. However, Richtmyer proved that the exponential decrease could not hold for all directions since it leads to the wrong conclusion, that the radiation quality factor (explained further in Section 2.3.1) is infinity [5]. This fact makes dielectric resonators useful as antenna elements.

To avoid complicated problems in some investigations, it is supposed that the lateral surfaces are magnetic walls and the flat ends (in case of cylindrical geometry) allow fields to leak out [6]. This can achieve acceptable results for some specific modes. For an arbitrarily-shaped dielectric resonator of high permittivity, a general mode classification is presented by Van Bladel. Based on this classification, modes of a dielectric resonator can be of a confined type (the boundaries of the dielectric are considered as perfect magnetic walls and thus electromagnetic waves are considered to be confined in the dielectric) or nonconfined type (none of the dielectric boundaries are perfect magnetic walls, thus electromagnetic waves can leak outside). The following equations, which are the magnetic wall boundary conditions, are satisfied at the surfaces of the resonator for confined modes

$$\vec{E}.\hat{n}=0, \tag{2.1}$$

$$\hat{n}\times\vec{H}=\vec{0} \tag{2.2}$$

In these equations $\vec{E}$ and $\vec{H}$ are the electric and magnetic field intensity respectively, and $\hat{n}$ is the normal to the surface of the resonator.

Modes of a dielectric resonator which only satisfy Equation (2.1) are defined as nonconfined modes. According to Van Bladel's theory, only dielectric bodies of revolution such as spheres or cylinders can support confined modes. One example of a confined mode is the lowest order mode of a cylindrical resonator, $TM_{01\delta}$. A rectangular resonator can only support the nonconfined modes since it is not a body of revolution. It has also been shown by Van Bladel that the lowest order confined modes (e.g. $TM_{01\delta}$ in a cylindrical resonator) radiate like an electric dipole and the lowest order nonconfined modes (e.g. $TE_{01\delta}$ in a cylindrical resonator or TE_{111} in a rectangular resonator) radiate like a magnetic dipole.

Based on the latest mode classification for spherical- and cylindrical-shaped resonators that is also proven by numerous experiments in the literature, the modes of a spherical dielectric resonator are of transverse electric (*TE)* or transverse magnetic (*TM)* type and the modes of a cylindrical dielectric resonator

are of (*TE)*, (*TM)*, or hybrid electromagnetic (*HEM*) type. However, no rigorous mode classification is provided for rectangular dielectric resonators so far. In 1962, Okaya and Barash divided the modes of a rectangular resonator into two kinds of *TE(H)* and *TM(E)* modes [7]. Extensive experiments by Mongia et al. have shown that not all the *TM* modes predicted by Okaya and Barash are observed [8]. This result is consistent with Van Bladel's theory about existence of only nonconfined modes in rectangular dielectric resonators.

An exact analytical closed-form solution does not exist for dielectric resonator geometries except hemispherical resonators. Numerical techniques such as Finite Element Method (FEM) or Finite Difference Time Domain (FDTD) explored in later sections can produce better electromagnetic solutions for these dielectric structures. Approximate solutions based on the above principles are useful in developing a conceptual understanding for different geometries. In the following sections, the two most used geometries in the literature, cylindrical and rectangular shapes, are investigated.

2.2 The Cylindrical Dielectric Resonator Antenna

Fig. 2.2 shows a typical configuration of an isolated cylindrical dielectric resonator antenna (CDRA) with dielectric constant of ε_r, height of $2d$, and radius of a. The lowest order mode of a CDRA can be one of these three modes, the $TM_{01\delta}$, $TE_{01\delta}$, and $HEM_{11\delta}$, depending on aspect ratio and feeding parameters of the CDRA. The subscripts denote the variation of fields along the azimuthal (φ), radial (r), and axial (z) directions respectively, inside the resonator. The value of δ ranges between zero and one, and approaches one for high values of dielectric constant where most of the fields are contained in the z direction. These modes also show the lowest value for radiation Q-factor, providing wider impedance bandwidth for the antenna.

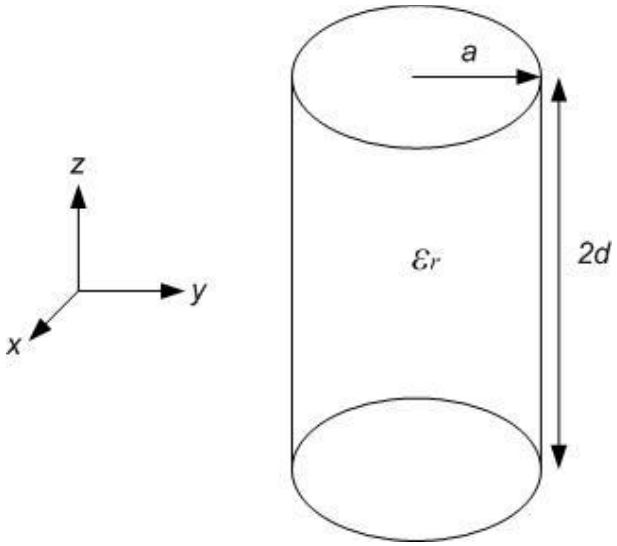

Fig. 2.2. Structure of an isolated cylindrical dielectric resonator antenna.

2.2 .1 Resonance Frequency and Radiation Q-Factor

The approximate analysis is based on the principles mentioned in the first section of this chapter. For instance, in one simple analysis for *TM* modes of a CDRA, it is supposed that the CDRA surfaces are perfect magnetic conductors and the wave function is derived as follows [2]

$$\psi_{TM_{npm}} = J_n\left(\frac{X'_{np}}{a}\rho\right)\begin{Bmatrix}\sin n\phi\\ \cos n\varphi\end{Bmatrix}\cos\left[\frac{(2m+1)\pi z}{2d}\right] \tag{2.3}$$

where J_n is the Bessel function of the first kind. From the separation equation ($k_\rho^2 + k_z^2 = k^2 = \omega^2\mu\varepsilon$), the resonant frequency of $TM^z{}_{npm}$ (transverse magnetic in the z direction: $H_z = 0$) is achieved

$$f_{npm} = \frac{1}{2\pi a\sqrt{\mu\varepsilon}}\sqrt{X'^2_{np} + \left[\frac{\pi a}{2d}(2m+1)\right]^2} \tag{2.4}$$

In other studies, the DWM and effective dielectric constant (EDC) methods are developed to determine the electromagnetic wave components inside the CDRA for different modes and consequently predict the resonant frequency and radiation Q-factor [9-10]. The DWM method assumes that the fields in the radial direction inside the resonator vary in a similar way as in an infinite dielectric

waveguide with the same radius and permittivity as those of the resonator. Moreover, in the axial direction the fields have a standing wave pattern similar to that of an infinite radial dielectric slab guide of the same height and permittivity as those of the resonator. The EDC method is similar to the DWM method, but gives an improved approximation for the wavenumbers inside the resonator. These two methods lead to fairly accurate results for the resonant frequencies of the various modes.

Based on rigorous numerical analysis closed-form empirical expressions have also been developed for the resonant frequency and the radiation Q-factor of the lower order CDRA modes [11]. These expressions, which are reorganized in [12], are simple to use and provide high degree of accuracy for the resonant frequency and moderate accuracy for the radiation Q-factor. For the $TM_{01\delta}$ mode, the expressions are as follows

$$k_0 a = 0.8945\left(1 + 3.017x^{0.881} + e^{0.962-1.6252x}\right) / \varepsilon_r^{0.45} \tag{2.5}$$

$$Q = 10.9x\left(1 + 217.96x^{3.4796}e^{-3.67x}\right) \tag{2.6}$$

where $x = a/2d$, $k_0 = 2\pi f_0/c$ is the free-space wavenumber corresponding to the resonant frequency f_0, and c is the velocity of light in free space. For the $TE_{01\delta}$ mode, the expressions are given as

$$k_0 a = \left(2.1439 + 0.6604x + 0.2733x^2 - 0.1919x^3\right) / \varepsilon_r^{0.475} \tag{2.7}$$

$$Q = 5.72x\left(1 + 18.387x^{-0.3795}e^{-1.64x}\right) \tag{2.8}$$

For the $HEM_{11\delta}$ mode, the expressions are as follows

$$k_0 a = \left(1.6 + 0.513x + 1.392x^2 - 0.575x^3 + 0.088x^4\right) / \varepsilon_r^{0.42} \tag{2.9}$$

$$Q = x\varepsilon_r^{1.2}\left(0.01893 + 2.925e^{-2.08x(1-0.08x)}\right) \tag{2.10}$$

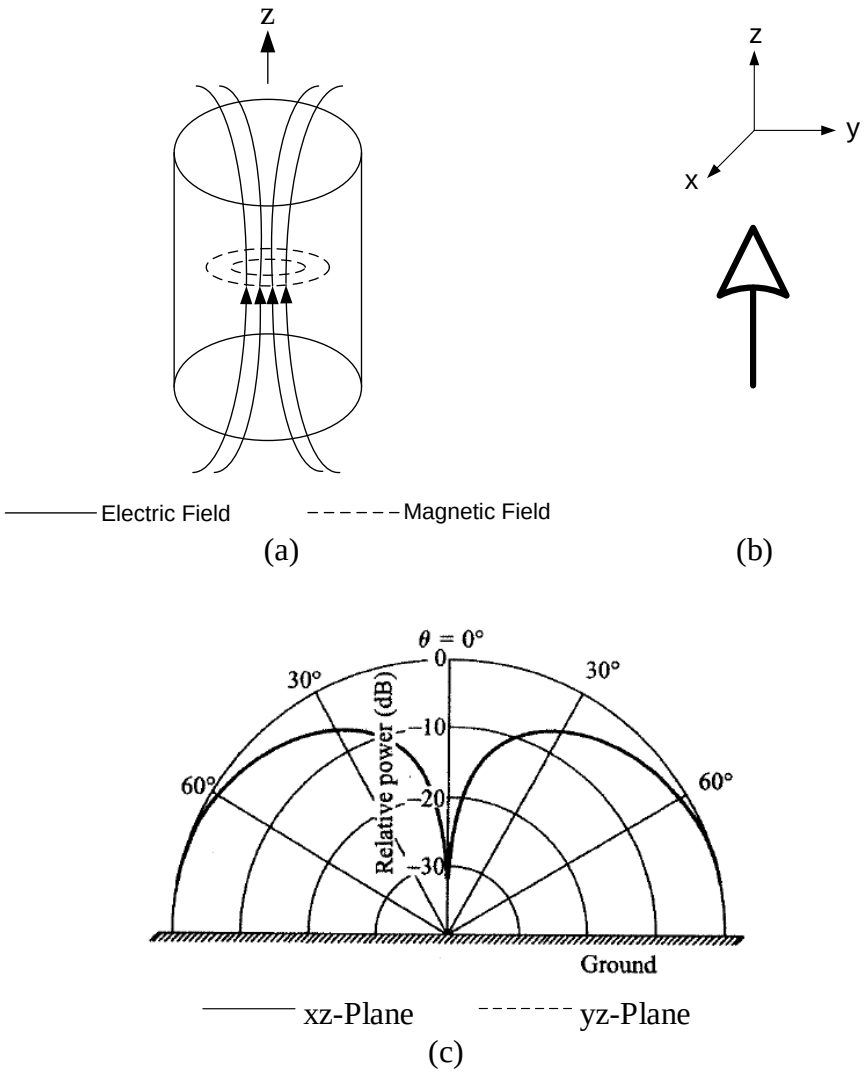

Fig. 2.3. (a) Electromagnetic field distributions of the $TM^{z}_{01\delta}$ mode inside the isolated cylindrical dielectric resonator; (b) Vertical short electric dipole equivalence; (c) Ideal far field radiation patterns above an infinite ground plane. The patterns in both planes are the same and overlapped.

2.2.2 Radiation Model

The field configurations inside the CDRA for the three lowest order modes of cylindrical resonators: $TM_{01\delta}$, $TE_{01\delta}$, and $HEM_{11\delta}$, are discussed and plotted in this subsection. These plots are very useful in understanding the modes of a CDRA, to predict the far field radiation patterns, and to design coupling schemes for various modes.

Fig. 2.3(a) shows the electric and magnetic field lines in two perpendicular planes for $TM^{z}_{01\delta}$ mode. This corresponds to a vertical electric dipole in the *z*

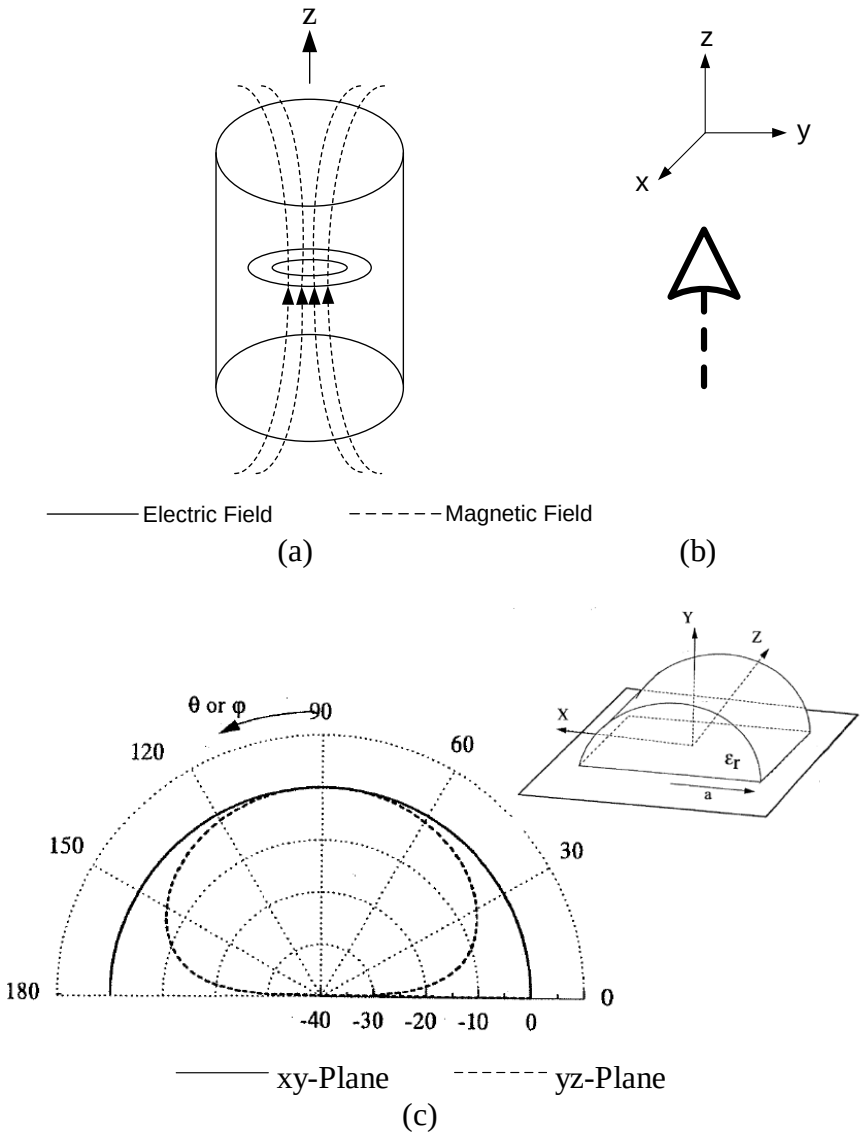

Fig. 2.4. (a) Electromagnetic field distributions of the $TE^{z}_{01\delta}$ *mode* inside the isolated cylindrical dielectric resonator; (b) Equivalent short magnetic dipole along the z axis; (c) Ideal far field radiation patterns above an infinite ground plane.

direction (Fig. 2.3(b)). Consequently, the far field radiation of $TM_{01\delta}$ should be similar to that of the electric dipole as depicted in Fig. 2.3(c).

The field distribution inside the cylindrical resonator is sketched in Fig. 2.4(a) for $TE^{z}_{01\delta}$ mode. This is equivalent to a magnetic dipole aligned along the z-axis (Fig. 2.4(b)). Therefore the far field radiation pattern, as shown in Fig. 2.4(c), is

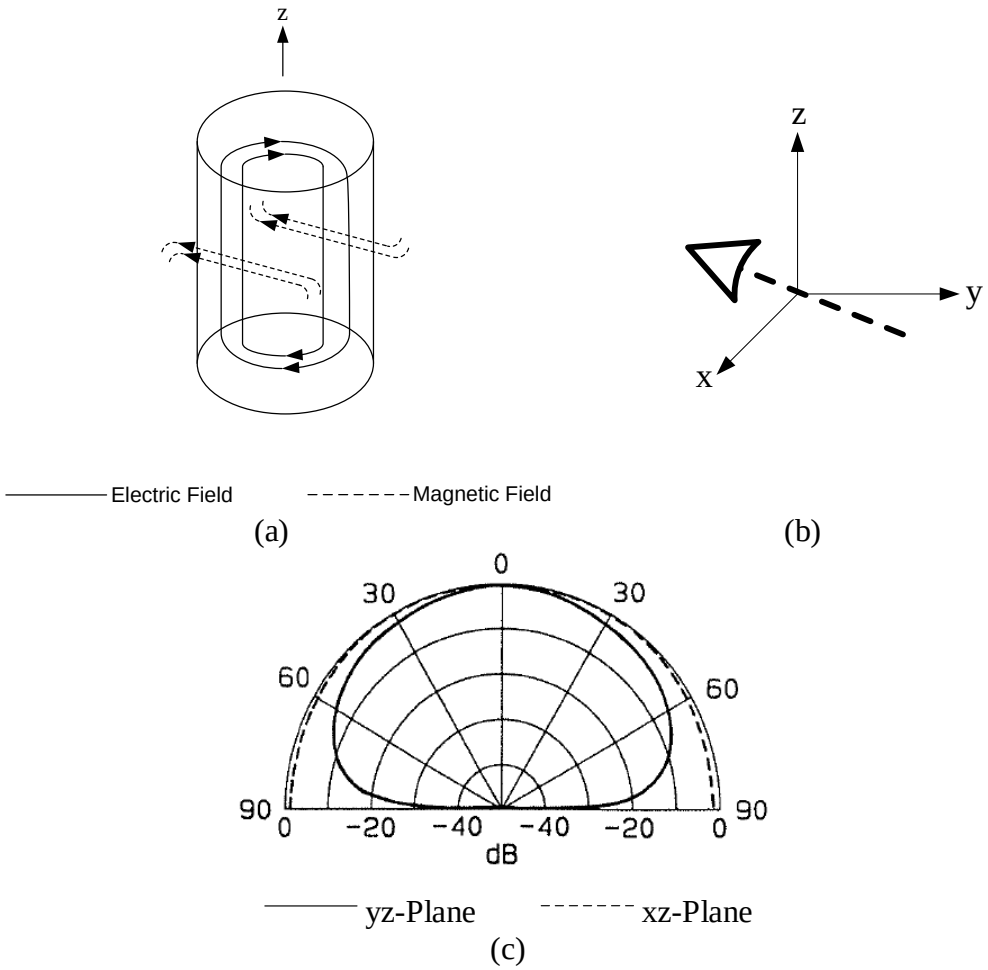

Fig. 2.5. (a) Electromagnetic field distributions of the $HEM_{11\delta}$ *mode* inside the isolated cylindrical dielectric resonator; (b) Equivalent horizontal short magnetic dipole; (c) Ideal far field radiation patterns above an infinite ground plane.

similar to that of the magnetic dipole. It should be noted that the perfect electric conductor (PEC) plane of symmetry is any φ = constant *rz* plane.

Fig. 2.5 shows near field distributions, equivalent dipoles, and approximate radiation patterns for $HEM_{11\delta}$ mode. $HEM_{11\delta}$ corresponds to a horizontal magnetic dipole as depicted in Fig. 2.5(b). The resulting radiation patterns (Fig. 2.5(c)) are similar to those of magnetic dipole.

More details on near field distributions of dielectric resonators can be find in [13]. It is worth mentioning that the above-stated nature of the radiated fields of different modes is generally independent of the dielectric constant of the resonator material [11].

2.3 The Rectangular Dielectric Resonator Antenna

The rectangular DRA has shown some advantages over the other shapes of DRAs. For example, the three available dimensions provide two degrees of freedom more than the hemispherical shaped DRA and one degree of freedom more than the cylindrical shaped DRA. This can be manipulated to design an antenna with better performance. Mode degeneracy which limits antenna performance by increasing cross-pol levels and always exists in spherical and hybrid modes of cylindrical DRAs can be avoided by properly choosing the three dimensions of the resonator in the case of rectangular DRA. Furthermore, two aspect ratios of rectangular structures (height/length and width/length) can be managed to enhance the bandwidth of DRAs.

Although there is no rigorous analysis for a simple rectangular DRA, the rough analysis is mostly composed of the Dielectric Waveguide Model (DWM) of Marcatili [14] and the mode definition theory of Okaya and Barash [8] based on Van Bladel's boundary conditions theories [3-4]. This composite method was first used by Mongia and Ittipiboon [15] for the dominant mode of the rectangular DRA. It can, however, be generalized to define all modes of the rectangular DRA. A summary for TE^{x}_{mnl} (transverse electric in the x direction: $E_x = 0$) modes is as follows.

2.3.1 Resonance Frequency and Radiation Q-Factor

The field components inside an isolated rectangular DRA (shown in Fig. 2.6) can be obtained from the electric vector potential at the x direction, F_x [16].

$$E_x = 0 \tag{2.11}$$

$$E_y = -\frac{1}{\varepsilon}\frac{\partial F_x}{\partial z} \tag{2.12}$$

$$E_z = \frac{1}{\varepsilon}\frac{\partial F_x}{\partial y} \tag{2.13}$$

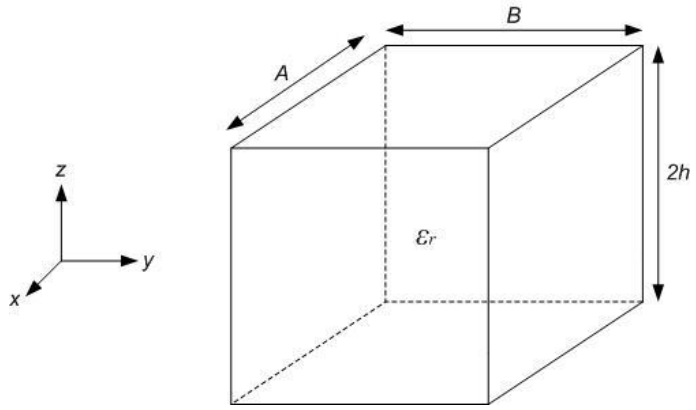

Fig. 2.6. Structure of an isolated rectangular dielectric resonator antenna.

$$H_x = -j\frac{1}{\omega\mu\varepsilon}\left(\frac{\partial^2}{\partial x^2} + k^2\right)F_x \tag{2.14}$$

$$H_y = -j\frac{1}{\omega\mu\varepsilon}\frac{\partial^2 F_x}{\partial x \partial y} \tag{2.15}$$

$$H_z = -j\frac{1}{\omega\mu\varepsilon}\frac{\partial^2 F_x}{\partial x \partial z} \tag{2.16}$$

Where F_x must satisfy the scalar wave equation of

$$\nabla^2 F_x(x,y,z) + k^2 F_x(x,y,z) = 0 \tag{2.17}$$

A solution to Equation (2.17) for the rectangular dielectric resonator is

$$F_x(x,y,z) = f(x)\times\left[C_2\cos(k_y y) + D_2\sin(k_y y)\right]\times\left[C_3\cos(k_z z) + D_3\sin(k_z z)\right] \tag{2.18}$$

If we also suppose a standing wave in the x direction

$$f(x) = C_1\cos(k_x x) + D_1\sin(k_x x) \tag{2.19}$$

Enforcing (2.1) at $y = 0$ and $z = 0$ boundaries gives

$$E_y\,(y = 0) = 0 \tag{2.20}$$

$$E_z\,(z = 0) = 0 \tag{2.21}$$

These two conditions lead to $C_2 = C_3 = 0$, Therefore F_x is reduced to

$$F_x(x,y,z) = f(x)\times\left[D\sin(k_y y)\sin(k_z z)\right] \tag{2.22}$$

In which $D = D_1 D_2$.

Enforcing (2.1) at the other two boundaries, $y = B$ and $z = 2h$, leads to

$$E_y(y=B)=0 \Rightarrow \sin(k_y B)=0 \Rightarrow k_y=\frac{n\pi}{B},\ n=1,2,... \tag{2.23}$$

$$E_z(z=2h)=0 \Rightarrow \sin(2hk_z)=0 \Rightarrow k_z=\frac{l\pi}{2h},\ l=1,2,... \tag{2.24}$$

Now, based on the DWM of Marcatili

$$k_x\left(\frac{A}{2}\right)=\tan^{-1}\left(\frac{\left[k_0^2(\varepsilon_r-1)-k_x^2\right]^{\frac{1}{2}}}{k_x}\right)+\frac{1}{2}(m-1)\pi \qquad m=1,2,... \tag{2.25}$$

The separation equation can be derived from (2.17)

$$k_x^2+k_y^2+k_z^2=\varepsilon_r k_0^2 \tag{2.26}$$

or

$$f_r=\frac{c}{2\pi\sqrt{\varepsilon_r}}\sqrt{k_x^2+k_y^2+k_z^2} \tag{2.27}$$

The resonant frequency of TE^x_{mnl} can be derived using the last five equations. The resonant frequency of TE^y_{mnl} and TE^z_{mnl} modes can be derived in the same manner.

The radiation Q factor of a rectangular DRA can be determined by finding the total stored energy and the radiated power. It is supposed that the rectangular DRA is made of a dielectric material with very low dielectric loss.

$$Q_{rad}=2\omega_0\frac{Stored\ Energy}{Radiated\ Power} \tag{2.28}$$

Since the electric and magnetic field inside the rectangular resonator are derived, the total stored energy can be computed by integration of the power density [16],

$$W_e=\frac{\varepsilon_0\varepsilon_r ABh}{16}\left(1+\frac{\sin k_x A}{k_x A}\right)\left(k_y^2+k_z^2\right) \tag{2.29}$$

According to Van Bladel's theory, the lowest order mode of a rectangular DRA (TE_{111}) radiates like a magnetic dipole, therefore based on the standard relation for the power radiated by a magnetic dipole of moment p_m [15],

$$P_{rad} = 10k_0^4 \left| \frac{-8j\omega\varepsilon_0(\varepsilon_r - 1)}{k_x k_y k_z} sin\left(\frac{k_x A}{2}\right) \right|^2 \tag{2.30}$$

Consequently, the radiation Q factor of the TE^x_{111} of the rectangular DRA shown in Fig. 2.6 can be approximated as:

$$Q_{rad} = \frac{\varepsilon_r A k_x^2 (k_y^2 + k_z^2)}{5\left[\frac{8k_0}{\pi}\right]^4 Bh\omega_0\varepsilon_0(\varepsilon_r - 1)^2} \frac{\left[1 + \frac{sin(k_x A)}{(k_x A)}\right]}{sin^2(\frac{k_x A}{2})} \tag{2.31}$$

The Q_{rad} is one of the most important antenna parameters and provides an estimate of the antenna's impedance bandwidth [11],

$$BW = \frac{S-1}{Q_{rad}\sqrt{S}} \tag{2.32}$$

In this equation S is the maximum acceptable VSWR and BW denotes the antenna's bandwidth.

It can be concluded that as the dielectric permittivity increases, the Q-factor increases and fields become more and more confined inside the dielectric resonator. In other words, a low Q-factor corresponds to larger radiated power and wide impedance bandwidth antenna.

2.3.2 Radiation Model

To excite the appropriate mode in the DRA and achieve maximum possible coupling between (magnetic or electric) source and dielectric resonator, it is necessary to have knowledge of the field distribution of the modes of the isolated DRA. In other words, the near field distribution can help us to determine the proper method to couple to a particular mode. The far field propagation of dielectric resonators can be predicted by field distributions inside resonators. Here, the lower order modes of the rectangular DRA are investigated. However, the procedure would be similar for all other modes of DRAs.

The lowest order mode of a rectangular dielectric resonator is TE_{111}. The mode subscripts refer to field variation in the x, y, and z directions respectively, in

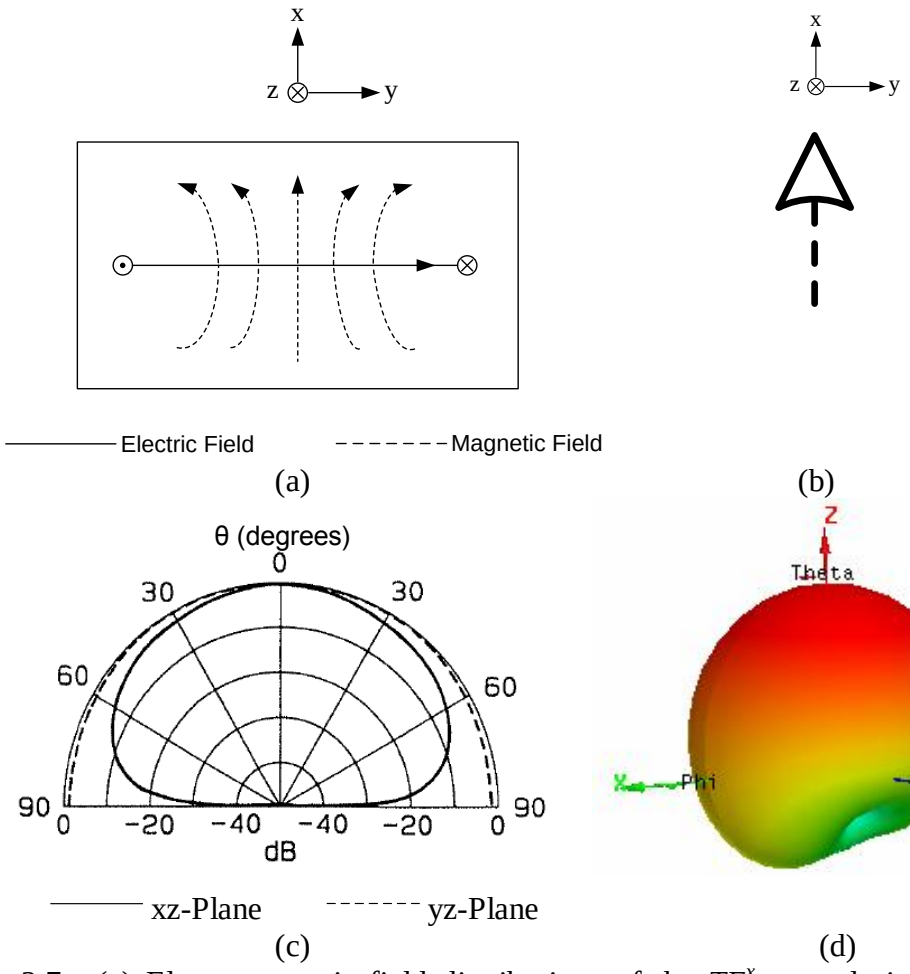

Fig. 2.7. (a) Electromagnetic field distributions of the TE^{x}_{111} mode inside the isolated rectangular dielectric resonator; (b) Horizontal short magnetic dipole equivalence; (c) Ideal far field radiation patterns above an infinite ground plane; (d) three dimensional radiation pattern above a finite ground plane.

rectangular coordinates. Fig. 2.7 shows the equivalent model for a rectangular DRA in the TE^{x}_{111} mode. The electric and magnetic field distribution is shown in Fig. 2.7(a) and corresponds to a horizontal magnetic dipole in the *x* direction (Fig. 2.7(b)). As a result, the radiation pattern generated by DRA in the TE^{x}_{111} mode can be approximated using the short magnetic dipole (Fig. 2.7(c)).

The analysis of higher order modes would be straightforward and follows the same manner. For instance, TE^{x}_{131} mode is equivalent to three magnetic dipoles, two of them in $+x$ direction and the other in $-x$ direction, as shown in Fig. 2.8. This mode radiates like the dominant mode of the rectangular DRA (explained further in Sections 3.1 and 3.4).

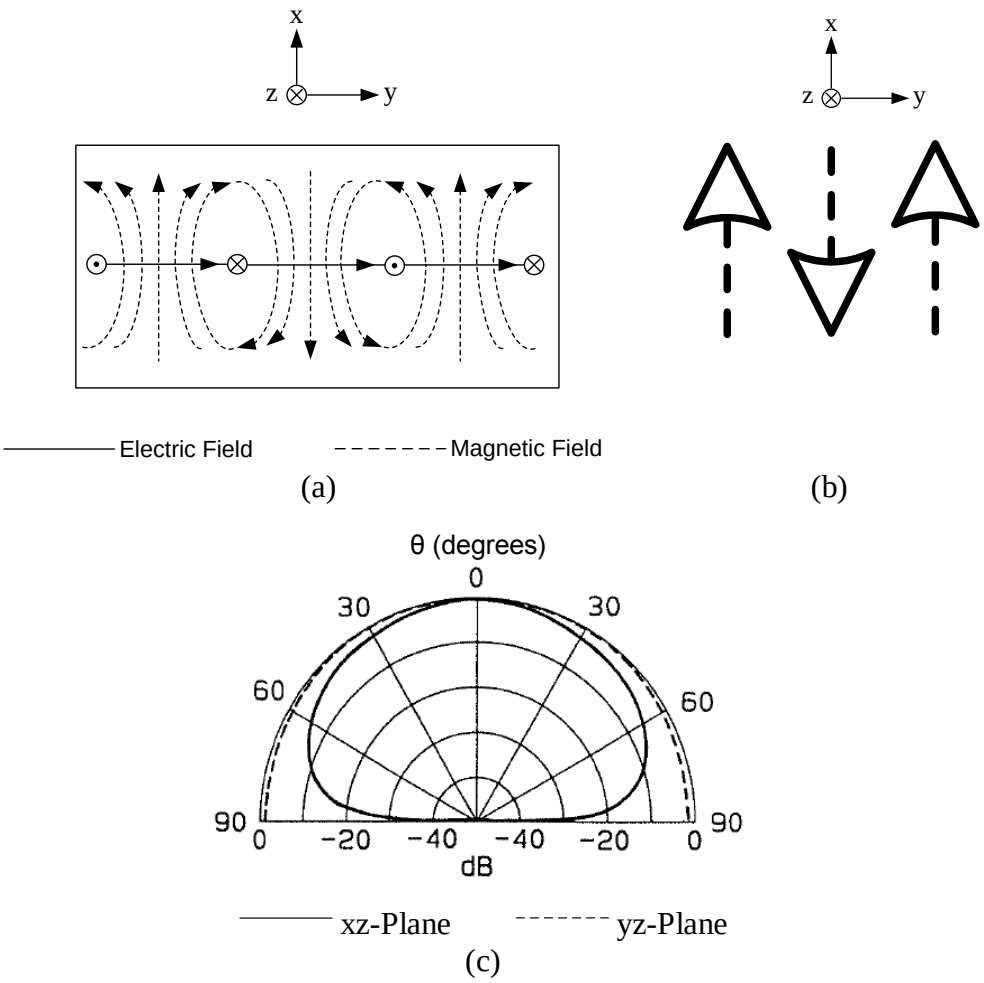

Fig. 2.8. (a) Electromagnetic field distributions of the TE^{x}_{131} mode inside the isolated rectangular dielectric resonator; (b) Horizontal short magnetic dipole equivalence; (c) Ideal far field radiation patterns above an infinite ground plane.

2.4 Excitation Schemes

Energy coupling is an important part of antenna design and fabrication. It affects all the antenna characteristics including impedance bandwidth, radiation patterns, and polarization. Each type of coupling scheme positioned in a particular place with respect to the antenna can result in exciting a specific mode and consequently creating specific antenna characteristics. To optimize the antenna performance, knowledge of different excitation schemes is necessary.

DRAs offer simple coupling schemes to nearly all transmission lines used at microwave applications. This fact makes DRAs suitable for integration into different planar technologies. The coupling can be easily controlled by varying the position of the resonator with respect to the transmission line. To achieve higher coupling, other excitation schemes such as aperture, probe, and many other methods which were previously applied on microstrip patch antennas can be used. The mechanism to achieve strong coupling for a desired mode is based on the Reciprocity Theorem which conveys that the electric current source should be located in an area of strong electric fields and the magnetic current source should be positioned in an area of strong magnetic fields. In the following subsections examples of different coupling methods are presented. To appropriately excite the desired (usually dominant) mode of DRAs, field distributions studied in the previous section is considered.

2.4.1 Microstrip Line Coupling

Direct microstrip coupling is one of the simple methods to excite a DRA. This method has received much attention especially for array applications due to its simplicity and reproducibility by lithographic technology. Fig. 2.9 shows this feeding scheme applied to excite the dominant mode of the rectangular DRA. As depicted in Fig. 2.9(a), the magnetic field in the DRA should coincide with that of the microstrip line to achieve a strong coupling. The degree of coupling depends on DRA permittivity and the distance of the DRA from the microstrip line end, ΔL, (shown in Fig. 2.9(b)). The microstripline coupling can be used to excite the $HEM_{11\delta}$ mode of the CDRA as well. The impedance bandwidth of the microstrip-fed antenna can be enhanced by combining the DRA resonances and microstrip patch which is also used to feed DRA [17].

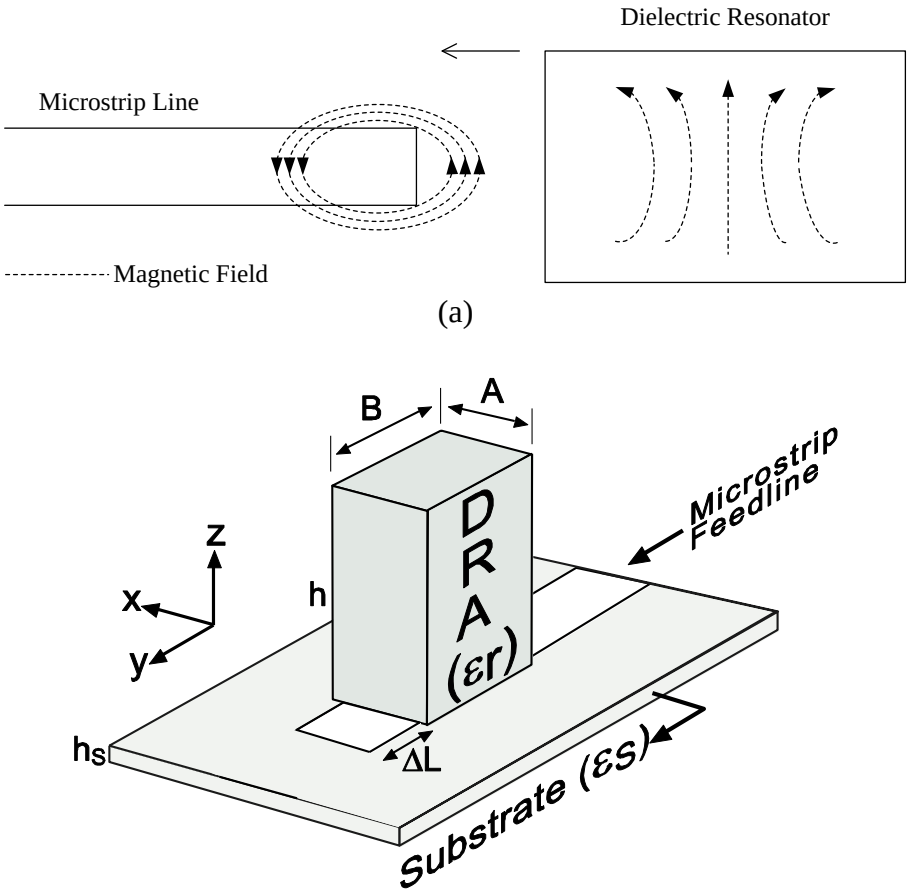

Fig. 2.9. (a) Magnetic field distributions of the microstripline and dominant mode of the rectangular DRA; (b) Structure of a microstrip-fed rectangular dielectric resonator antenna.

2.4.2 Coplanar Waveguide (CPW) Coupling

DRAs fed by CPW feedline have potential applications in MMIC technology and offer several advantages including low back radiation without using a back conductor and simple geometry. This feeding method can provide further control on impedance matching by adding different stub shapes at the end of the CPW line. For instance Fig. 2.10 shows the coplanar slot loop which can be used to feed different modes of the cylindrical DRA. The degree of coupling can vary by changing the dimensions of the loop and position of the loop with respect to the CDRA. The $HEM_{11\delta}$ mode and $TM_{01\delta}$ mode of the CDRA can be effectively excited if the loop position is kept around the boundary and middle of the

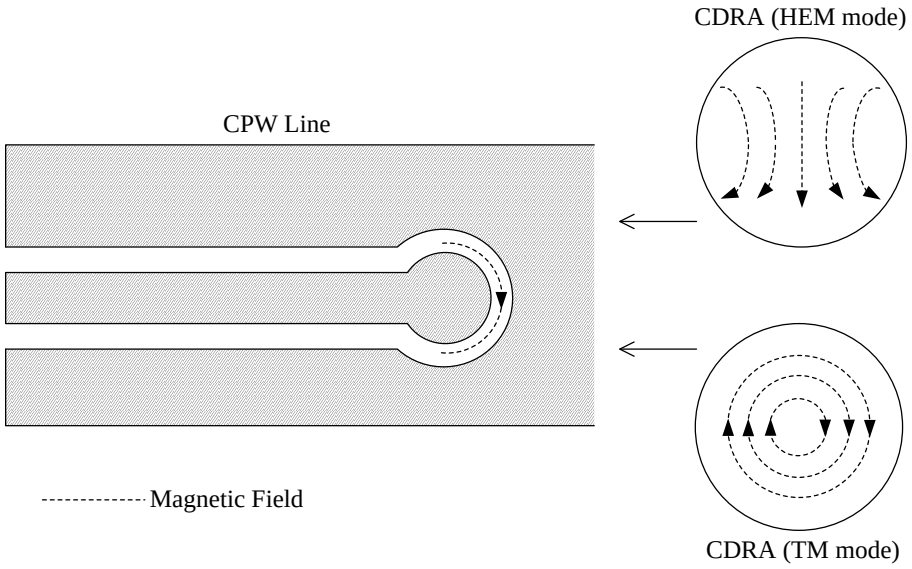

Fig. 2.10. Excitation of cylindrical dielectric resonator antenna using CPW line. Magnetic field distributions of the line and two different modes of the cylindrical DRA are shown.

resonator respectively. This can be concluded based on the magnetic field distributions of the coplanar slot loop and modes of the CDRA, as shown in Fig. 2.10.

2.4.3 Aperture Coupling

Aperture coupling is an extensively used feeding method because it is easy to implement at higher frequencies and is capable to provide enough coupling even for very low permittivity DRAs. Electromagnetic energy is transferred from a transmission line through the aperture etched in the ground plane to the DRA. The microstrip transmission line is placed on the other side of the board without interfering with the radiated field. Fig. 2.11 illustrates a typical configuration of aperture (slot)-fed DRA. The aperture acts like a horizontal magnetic dipole and should be positioned in the vicinity of maximum magnetic fields of the desired mode in the DRA to achieve optimum coupling. The coupling between the DRA and aperture can be controlled by varying the shape, size, and position of the aperture with respect to the DRA. The microstrip stub length, ΔL, has also a

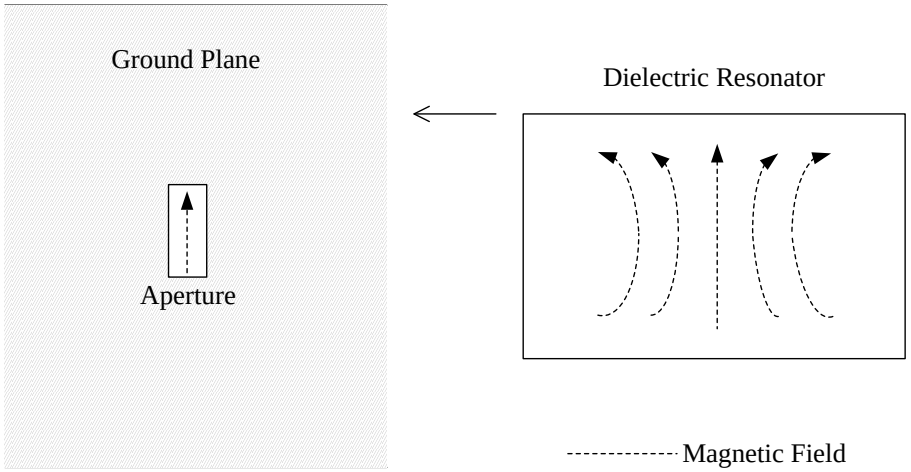

(a)

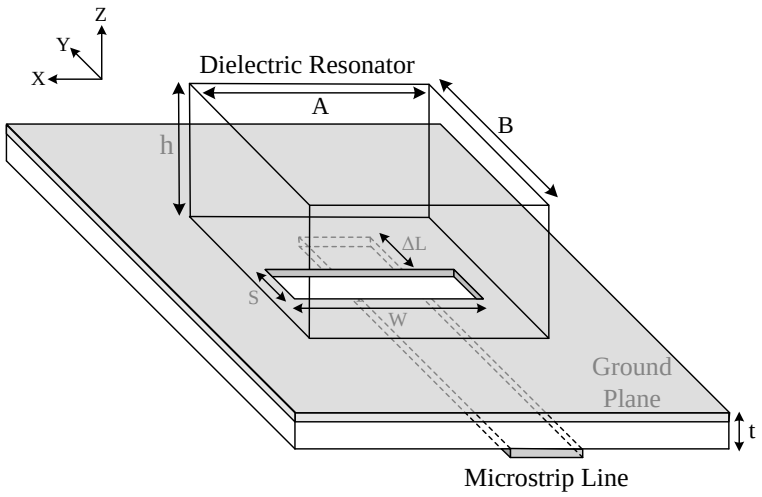

(b)

Fig. 2.11. Aperture coupling for the excitation of the TE_{111} mode of the rectangular DRA. (a) Magnetic field distributions of the aperture and TE_{111} mode of the rectangular DRA; (b) Structure of the slot-fed rectangular dielectric resonator antenna.

significant impact on the coupling value. Using an appropriate design, the DRA resonance can be merged with the slot resonance to achieve a wideband hybrid antenna. Circular polarization can also be produced when the DRA is inclined with respect to the aperture.

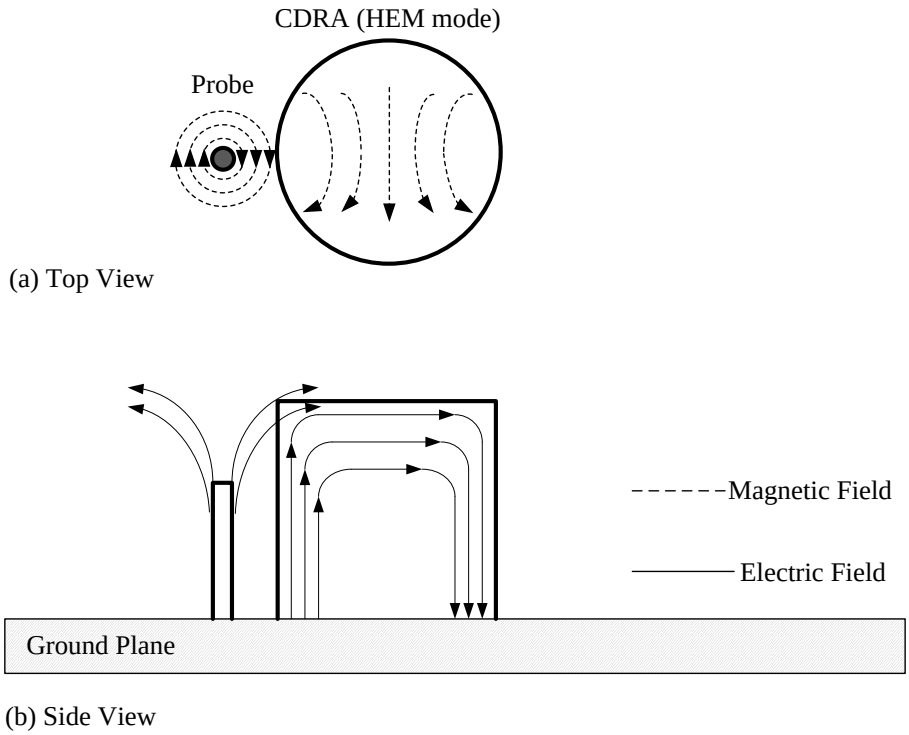

Fig. 2.12. Probe coupling for the excitation of the $HEM_{11\delta}$ mode of the cylindrical DRA. (a) Top view; (b) Side view.

2.4.4 Coaxial Probe Coupling

The coaxial probe is a low-cost simple coupling method and a good alternative to aperture-fed coupling at lower frequency bands in which the size of the aperture is unreasonably large to provide enough coupling. A typical probe-coupled cylindrical DRA configuration is shown in Fig. 2.12. To achieve maximum coupling for the $HEM_{11\delta}$ mode of the CDRA, the probe (which behaves like a vertical electric current) should be placed at the maximum electric field intensity location (at the border of the resonator), according to field distribution shown in Fig. 2.12. The degree of coupling can be controlled by varying the length and position of the probe. In some investigations on probe-coupled DRAs, the probe is placed inside the DRA by drilling a hole to further increase the coupling value. Depending on the position of the probe, various modes of the DRA can be excited and different polarizations can be achieved. For instance a

rectangular DRA excited with a probe in the corner of the resonator shows circular polarization. Finally, an important advantage of the probe coupling is that the impedance bandwidth of the antenna can be significantly enhanced by combining the resonances of DRA and monopole antenna. As a result, an ultra wideband hybrid circular DRA/monopole antenna is designed and fabricated in [18].

2.4.5 Strip Coupling

There are some drawbacks in using coaxial probe, microstrip line, and coplanar waveguide excitation methods. To provide a good match, the probe must be located inside the DRA, which requires drilling a hole in the resonator. To avoid drilling and simplify the fabrication, the probe is located at the outer edge of the resonator. However, the required match may not be achieved and a small uncontrolled air gap between the resonator and probe creates intensive matching problems. On the other hand, microstripline and coplanar waveguide couplings provide optimal match only for high permittivity (usually higher than 20) DRAs. The high permittivity DRAs provide narrow impedance bandwidths which are not sufficient for most applications.

To solve these problems and improve impedance matching, a flat metal strip can be attached onto the sidewall of the resonator and connected to the transmission line at the bottom side, as shown in Fig. 2.13 for microstripline excitation. The width, height, and thickness of the strip can be adjusted to improve the match significantly.

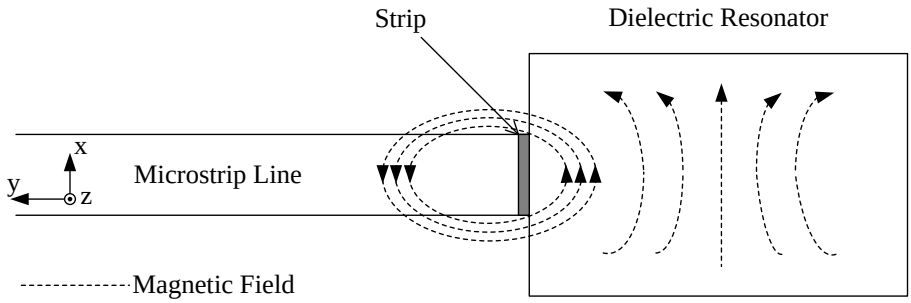

(a)

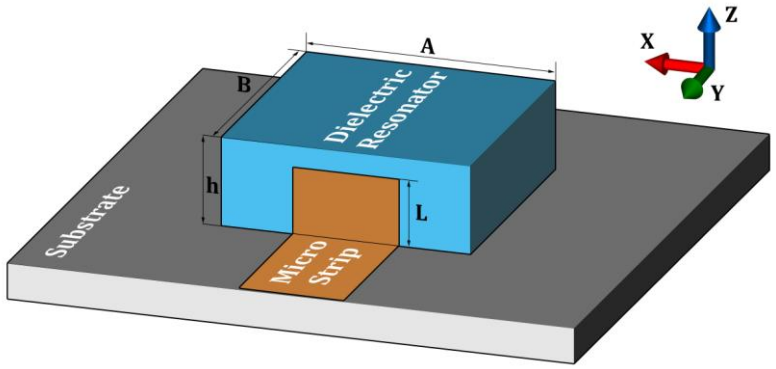

(b)

Fig. 2.13. (a) Magnetic field distributions of the strip and dominant mode of the rectangular DRA; (b) Structure of a strip-fed rectangular dielectric resonator antenna.

References

[1] A. Petosa, *Handbook of Dielectric Resonator Antennas*. Boston: Artech House, 2007.

[2] S. A. Long, M. McAllister, and L. C. Shen, "The resonant cylindrical dielectric resonator antenna," *IEEE Trans. Antennas & Prop.*, vol. 31, no. 3, pp. 406-412, May 1983.

[3] J. Van Bladel, "On the resonances of a dielectric resonator of very high permittivity," *IEEE Trans. On Microwave Theory and Techniques*, vol. MTT-23, no. 2, pp. 199-208, February 1975.

[4] J. Van Bladel, "The excitation of dielectric resonators of very high permittivity," *IEEE Trans. On Microwave Theory and Techniques*, vol. MTT-23, no. 2, pp. 208-215, February 1975.

[5] R. D. Richtmyer, "Dielectric resonator," *J. Appl. Phys.*, vol. 10, pp. 391-398, June 1939.

[6] K. K. Chow, "On the solution and field pattern of cylindrical dielectric resonators," *IEEE Trans. On Microwave Theory and Techniques*, vol. MTT-14, p. 439, September 1966.

[7] A. K. Okaya and L. F. Barash, "The dielectric microwave resonator," *Proc. IRE*, vol. 50, pp. 2081-2092, October 1962.

[8] R. K. Mongia, "Theoretical and experimental resonant frequencies of rectangular dielectric resonators," *IEE Proceeding*, vol. 139, pp. 98-104, February 1992.

[9] R. K. Mongia and B. Bhat, "Effective dielectric constant technique to analyze cylindrical dielectric resonators," *Arch. Elek. Ubertragung*, vol. 38, pp. 161-168, May 1987.

[10] R. K. Mongia, "On the accuracy of approximate methods for analyzing cylindrical dielectric resonators," *Microwave Journal*, vol. 34, pp. 146-150, October 1991.

[11] R. K. Mongia and P. Bhartia, "Dielectric resonator antennas- a review and general design relations for resonant frequency and bandwidth," *International Journal of Microwave and Millimeter-Wave Computer-Aided Engineering*, vol. 4, no. 3, pp. 230-247, 1994.

[12] K. M. Luk and K. W. Leung, *Dielectric Resonator Antennas*. Hertfordshire, England: Research Studies Press, 2002.

[13] D. Kajfez and P. Guillon, *Dielectric Resonators*. Norwood, Ma.: Artech House, 1986.

[14] E. A. J. Marcatili, "Dielectric rectangular waveguide and directional couplers for integrated optics," *The Bell System Technology Journal*, pp. 2071-2102, September 1969.

[15] R.K. Mongia, and A. Ittipiboon, "Theoretical and experimental investigations on rectangular dielectric resonator antennas," *IEEE Trans Antennas Propagat,* vol. 45, no. 9, pp. 1348-1356, September 1997.

[16] C. A. Balanis, *Advanced engineering electromagnetics.* New York, NY: Wiley, 1989.

[17] K. P. Esselle and T. S. Bird, "A hybrid resonator antenna: experimental results," *IEEE Trans Antennas Propagat,* vol. 53, no. 2, pp. 870-871, February 2005.

[18] M. Lapierre, Y. M. M. Antar, A. Ittipiboon, and A. Petosa, "Ultra wideband monopole/dielectric resonator antenna," *IEEE Microwave and Wireless Components Letters,* vol. 15, no. 1, pp. 7-9, January 2005.

Chapter 3

Improved Dielectric Resonator Antenna Performance

Improvements of DRA performance characteristics can be achieved by changing either the antenna structure or material properties. Several solutions are provided and discussed in this Chapter [1-7].

3.1 High-Aspect-Ratio High-Permittivity DRA

There are different ways to miniaturize antennas. Using fractal shapes, mostly applied for microstrip patch antennas, is one of these methods [8]. Applying an extra metallic plate which acts as an electric wall, if certain field symmetry exists, allows a part of the antenna to be removed, resulting in miniaturization [9]. The main disadvantages of this method are degradation of radiation pattern and antenna efficiency. Another method is to use high permittivity materials in the antenna structure [10]. Typically, the higher the dielectric constant, the more compact the size. However, high permittivity materials dramatically decrease antenna bandwidth.

High aspect ratio structures with high surface to volume ratio and dual-resonance characteristics are discussed in this section as an efficient way to maintain wide impedance bandwidth in a compact high dielectric constant microstrip-fed DRA. Because only one segment of high permittivity material is used in this approach, it is potentially simpler to fabricate compared to the multi-segment structures [11]. The dominant mode of high aspect ratio DRA along with a higher order mode is exploited to design a wideband antenna. Both modes have

similar radiation patterns and therefore ensure a stable radiation pattern and low cross polarization levels over the entire bandwidth.

The technique of merging resonant frequencies to achieve wideband operation has previously been studied in different ways. For instance, in [12] and [13] the resonant frequency of the DRA is mixed with another type of antenna; in [14] the resonant frequencies of two DRAs are merged; and in [15] and [16] the resonant frequencies of different modes of one DRA are considered. However, these techniques typically had to sacrifice other desirable properties to obtain wideband operation. The current work is distinguished by simultaneously realizing simple feed structure, wide impedance bandwidth, stable radiation pattern over the entire bandwidth, and miniaturization.

3.1.1 Theory and Concept

A photograph of a high aspect ratio microstrip-fed rectangular DRA is shown in Fig. 3.1. The dielectric resonator with a cross section of $A \times B$ and height of h has a dielectric constant of ε_r, and is situated on top of an open-circuit microstrip feedline designed to have a characteristic impedance of 50 Ω. The distance between the far end of the microstrip line and the DRA, ΔL, is changed to achieve maximum coupling. Although in this configuration both the TE^x modes and TE^y modes of the DRA are excited, it is found that the dominant mode along with several other lower order modes all belong to the TE^x modes of the DRA. Fortunately, coupling to these lower order modes is also much stronger than to the higher order modes.

To find the resonant frequency of TE^x_{mnl} modes, the structure is modeled with doubled height, based on Image Theory, and the hybrid method discussed in Chapter 2 is used. With reference to Fig. 3.1, the magnetic wall boundary conditions are assumed at $|y| = B/2$ and $|z| = h$, and the continuity of the tangential fields is supposed at $|x| = A/2$. By applying these boundary conditions

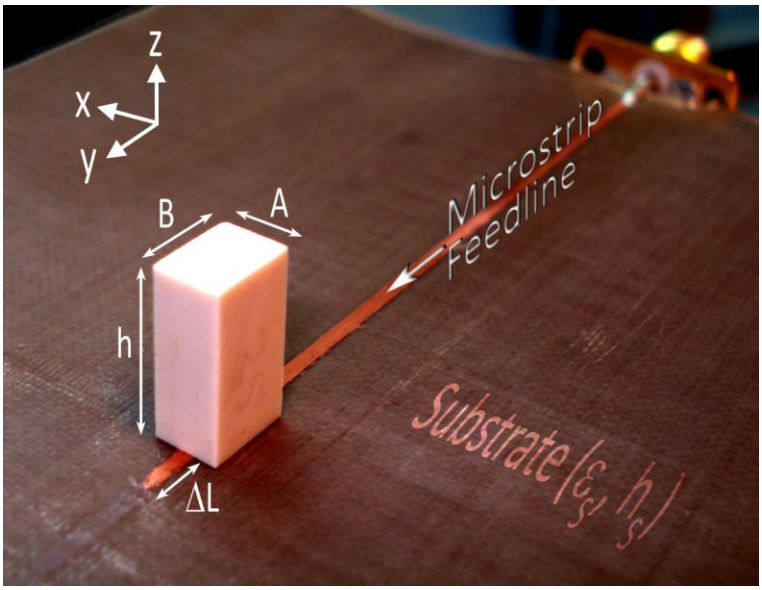

Fig. 3.1. Photograph of the fabricated high aspect ratio antenna.

on the field components inside the resonator, three equations for the wavenumbers k_x, k_y, and k_z are achieved

$$k_x\left(\frac{A}{2}\right) = tan^{-1}\left(\frac{\left[k_0^2(\varepsilon_r - 1) - k_x^2\right]^{\frac{1}{2}}}{k_x}\right) + \frac{1}{2}(m-1)\pi \qquad m = 1,2,\ldots \tag{3.1}$$

$$k_y = \frac{n\pi}{B} \quad , \quad n = 1,2,\ldots \tag{3.2}$$

$$k_z = \frac{l\pi}{2h} \quad , \quad l = 1,2,\ldots \tag{3.3}$$

The wavenumbers also satisfy the separation equation

$$f_r = \frac{c}{2\pi\sqrt{\varepsilon_r}}\sqrt{k_x^2 + k_y^2 + k_z^2} \tag{3.4}$$

in which f_r is the resonant frequency and c is the wave velocity in free space.

With reference to Fig. 3.1, when one dimension, h, is much bigger than the other two dimensions, k_z in Equation 3.3 becomes much smaller than k_x and k_y. Consequently, higher order modes of TE^x_{11l} when l = 2, 3, . . . will be much closer to the dominant mode of TE^x_{111}. In other words, when A is smaller than B and B is much smaller than $2h$, the dominant mode of the resonator is TE^x_{111} and the

following higher-order modes are TE^{x}_{112} and TE^{x}_{113}. However, the special boundary conditions due to the ground plane at the bottom surface and the air at the top surface of the resonator enforces excitation of only TE^{x}_{111} and TE^{x}_{113} modes. The resonant frequency of these two modes, based on the above mentioned equations and the geometry of the antenna, is mostly determined by *A*, *B*, and ε_r, while *h* is used to control the frequency distance between the two resonant modes. In fact, the bigger the *h*, the smaller the frequency distance between two resonant modes.

3.1.2 Design Analysis and Simulations

A high aspect ratio dielectric resonator with $(A \times B)$ of 4.6 mm by 6.4 mm cross section and dielectric constant of 25 is expected to resonate between 6 GHz to 8 GHz. To investigate the effect of various aspect ratios, $2h/A$, on the impedance bandwidth operation, different aspect ratios from 4.3:1 to 6.5:1 are considered. In Fig. 3.2(a), the variation of Ansoft™ HFSS simulated reflection coefficient values is shown while ΔL is maintained constant. The lower resonance which results from TE^{x}_{111} mainly stays fixed at the same frequency while the upper resonance which results from TE^{x}_{113} shifts down with increasing resonator height. Therefore, as predicted by equations, the frequency distance between two resonances increases with decreasing height. To have as wide as possible -10 dB impedance bandwidth, the aspect ratio should be kept around 5.2:1 in this case.

Another example is a high aspect ratio structure with $(A \times B)$ of 3 mm by 4.5 mm cross section and dielectric constant of 37. This structure is supposed to resonate between 7 GHz to 9 GHz. In Fig. 3.2(b), the variation of simulated reflection coefficient values is shown as the resonator aspect ratio is changed from 6:1 to 7.9:1. All other parameters such as ΔL are kept constant. To have a wide -10 dB impedance bandwidth in this case, the aspect ratio should be maintained around 7:1.

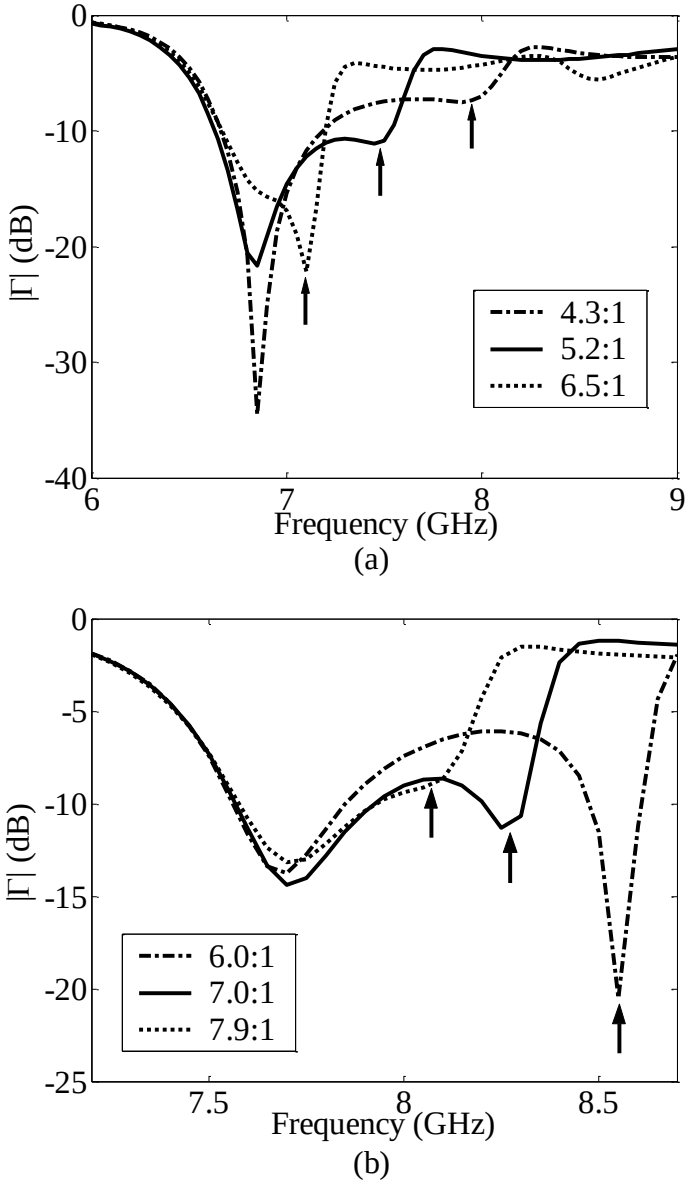

Fig. 3.2. Deviations of reflection coefficient values of the DRAs when the aspect ratio (*2h/A*) is changed. The TE^{x}_{113} resonances are indicated by arrows. (a) ε_r = 25 and $A \times B$ = 4.6 × 6.4 mm; (b) ε_r = 37 and $A \times B$ = 3.0 × 4.5 mm.

As shown in Fig. 3.2, to have a wide impedance bandwidth, the aspect ratio should be kept in a specific range depending on the dielectric constant of the resonator. Furthermore, when higher permittivity materials are chosen for the resonator, higher aspect ratio structures are required to have a wideband instead of dual band operation. In fact, the impedance bandwidth for individual modes

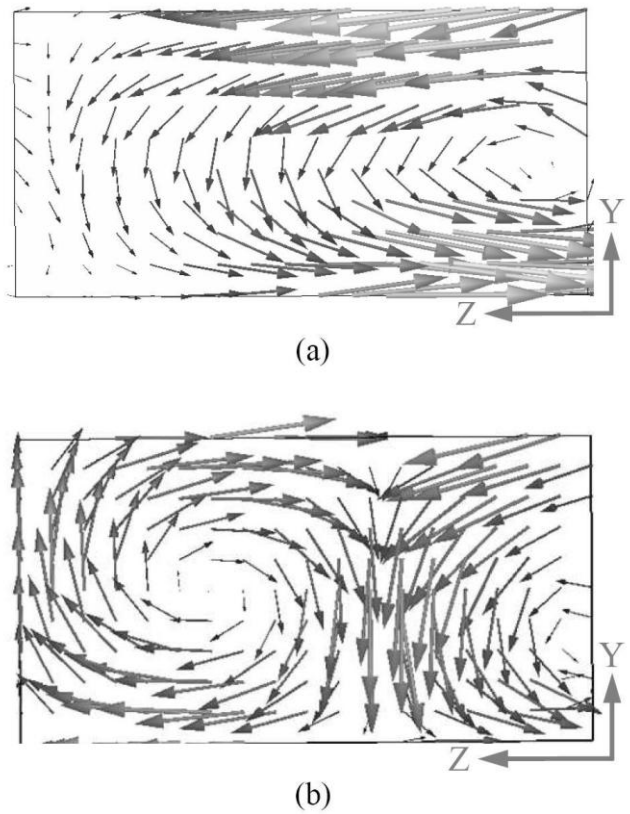

Fig. 3.3. Electric field distributions inside the dielectric resonator for (a) TE^{x}_{111} and (b) TE^{x}_{113} mode.

decreases with increasing dielectric constant and therefore the frequency distance between the end of the -10 dB bandwidth of the first resonance mode and the beginning of the -10 dB bandwidth of the second resonance mode increases. Therefore, higher aspect ratio structures are required to decrease the frequency distance between the two resonance modes. Increasing aspect ratio also slightly widens the bandwidth of individual modes. This is discussed in more details in Section 3.1.4. Simulation results for other structures with different permittivities have confirmed the above conclusion.

Fig. 3.3 illustrates the simulated electric field vectors inside the resonator for TE^{x}_{111} and TE^{x}_{113} modes. As shown, both modes have satisfied the boundary conditions (the continuity of the tangential component and the discontinuity of the normal component of the electric field) at $z = 0$, the interface between the ground plane and resonator, and $z = h$, the interface between the air and resonator.

However, electric fields of TE^{x}_{112} mode could not satisfy these particular boundary conditions. Therefore, the dominant mode and TE^{x}_{113} mode which have the same radiation patterns are excited in this case. It is to be noted that TE^{x}_{112} mode does not radiate efficiently because it is equivalent to two opposite magnetic dipoles with approximately the same values [17].

It is worth mentioning that another way to make high aspect ratio structure is by making tile shape structures [15]. However, in this case the higher order mode of TE^{x}_{121} is also excited, making unstable radiation patterns and high cross polarization levels over the entire bandwidth.

3.1.3 Experimental Results

To prove the idea of high aspect ratio DRA, two antennas similar to those discussed above are fabricated and measured. The dielectric resonators are made from ceramic materials provided by Trans-Tech™ and fed by a 50 Ω microstrip line designed on top of 15 cm by 10 cm ground plane. The substrate is a 15-mil thick Taconic™ TLY-5 with $\varepsilon_r = 2.2$ and $tan\ \delta_e \leq 0.0009$.

The first antenna, made from MCT-25 (a ceramic material provided by Trans-Tech™) with dielectric constant of 25 and $tan\ \delta_e \leq 0.0015$, is a high aspect ratio structure with 6.4 mm by 4.6 mm cross section and 12 mm height (5.2:1). The measured and simulated reflection coefficients in Fig. 3.4(a) show, in general, good agreement. The measured -10 dB bandwidth is 17 percent. The difference between the measured and simulated reflection coefficients may be due to the thin layer of adhesive between the antenna and ground plane.

Measured and simulated radiation patterns at both measured reflection coefficient minima (6.85 GHz and 7.35 GHz) in the E and H planes are shown in Fig. 3.5. Since both the lowest order mode and the higher order mode of TE^{x}_{113} radiate as horizontal magnetic dipoles, low cross polarization levels are maintained. The gain at 6.85 GHz and 7.35 GHz is roughly 5.0 and 4.5 dBi, respectively.

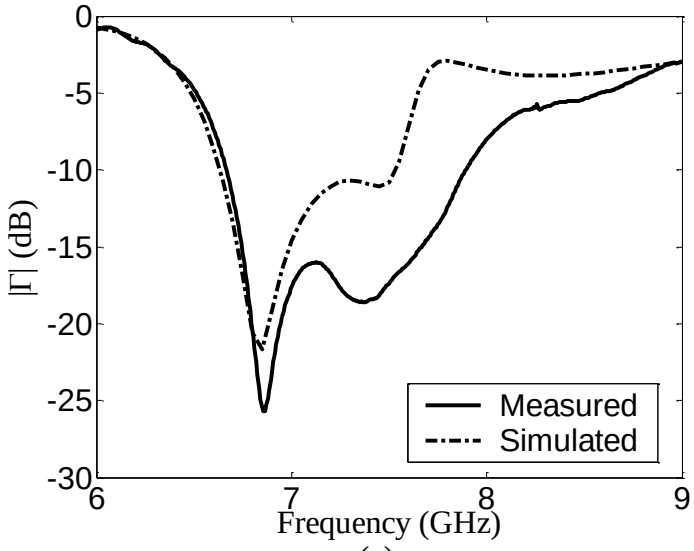

(a)

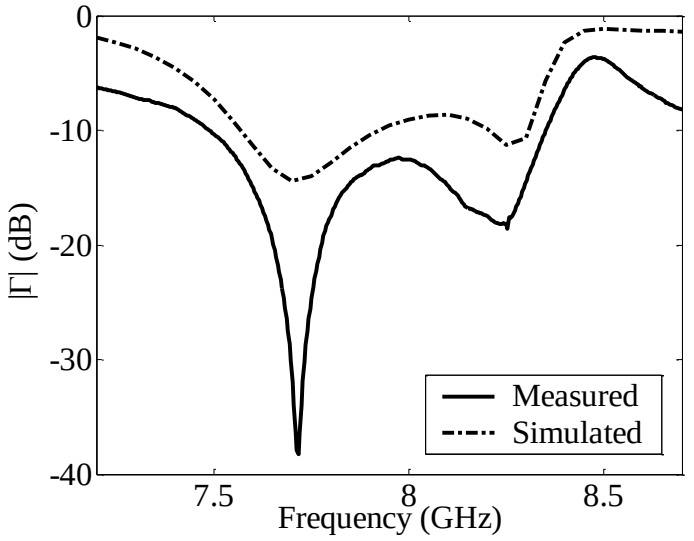

(b)

Fig. 3.4. Measured and simulated reflection coefficient of the high aspect ratio antennas. (a) ε_r = 25 and $A \times B \times h$ = 4.6 × 6.4 × 12 mm; (b) ε_r = 37 and $A \times B \times h$ = 3.0 × 4.5 × 10.5 mm.

The second fabricated antenna is also a tall structure made from D-38 Ba-Ti (a ceramic material provided by Trans-Tech™) with the dielectric constant of 37 and $tan\ \delta_e \leq 0.0005$. The antenna has 4.5 mm by 3 mm cross section and 10.5 mm height (7:1). Fig. 3.4(b) illustrates the measured and simulated reflection coefficients of the high aspect ratio DRA. The measured -10 dB bandwidth is 11 percent. Fig. 3.6 shows the measured and simulated antenna patterns at both

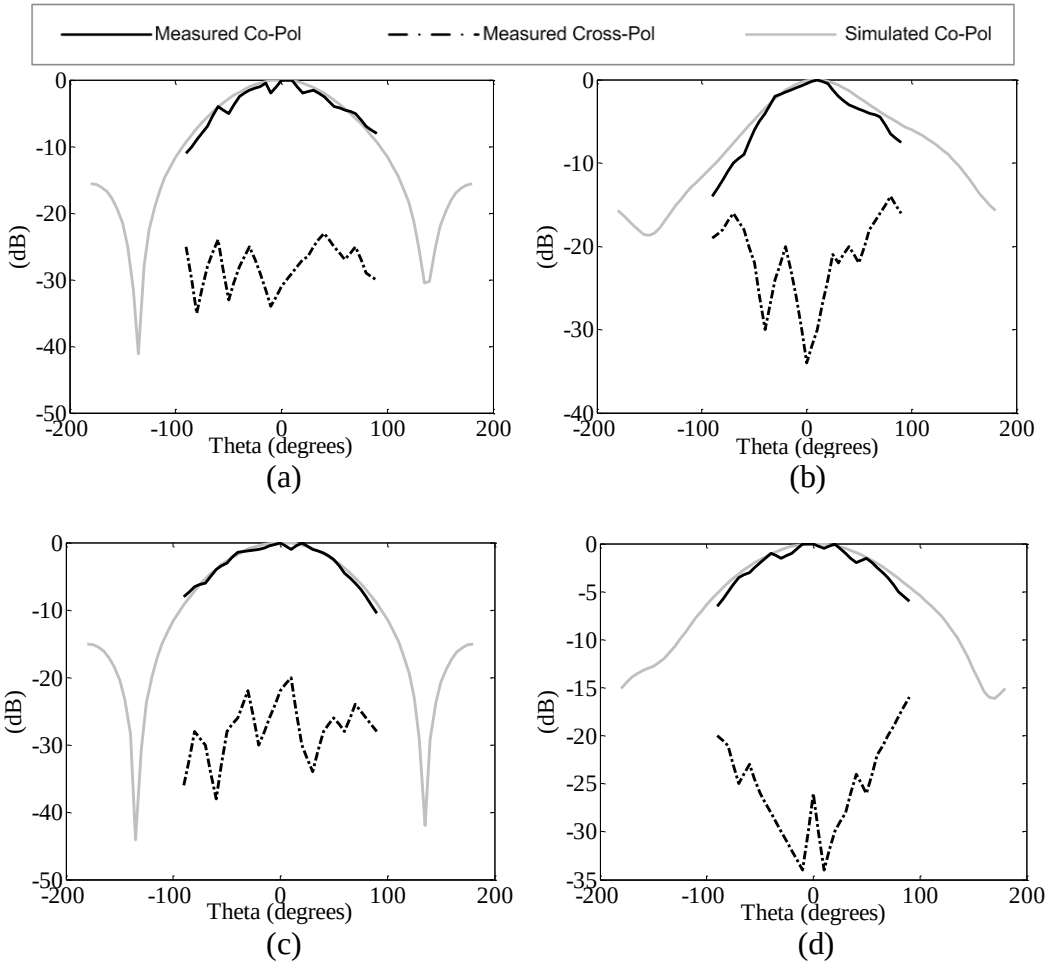

Fig. 3.5. Radiation patterns of the high aspect ratio DRA with permittivity of 25. (a) H (xz)-plane at 6.85 GHz (b) E (yz)-plane at 6.85 GHz (c) H (xz)-plane at 7.35 GHz (d) E (yz)-plane at 7.35 GHz.

measured reflection coefficient minima (7.72 GHz and 8.23 GHz) in the E and H planes. Stable radiation patterns and low cross polarization levels in the entire bandwidth are due to similar radiation properties of these two modes. Antenna gains of 4.8 and 4.4 dBi are achieved at 7.72 GHz and 8.23 GHz.

The gain-transfer method [18] in open space is performed to evaluate the gain of the fabricated antennas. In the experiments, the antenna is illuminated by a plane wave with similar polarization generated by a transmitting tower 10 m apart from the antenna under test and the received power is measured using Agilent 8564EC spectrum analyzer. Then the antenna is replaced with a standard antenna and the received power is again measured. The gain of the fabricated antenna is

computed in decibels using $G_F = G_S + 10 \log (P_F / P_S)$, where G_S is the gain of the standard antenna, P_F and P_S are the power received with the fabricated and standard antenna respectively [18].

The radiation patterns are measured by noting the relative received power when the antenna under test is rotated first in constant θ and then in constant φ planes in 5º steps. The accuracy of the rotation is better than 1º. A most probable source of the ripples in the measured radiation patterns (Figs. 3.5 and 3.6) is the reflections from obstacles in the open space.

The measured resonant frequencies of the fabricated antennas are compared with those of simulations and predicted (DWM) methods. The results are shown in Table 3.1. All resonant frequencies are within 5 percent from measured resonant frequencies except the predicted ones for the dominant mode of the tall structures which are 10.7 and 6.2 percent for the first and second high aspect ratio structures, respectively.

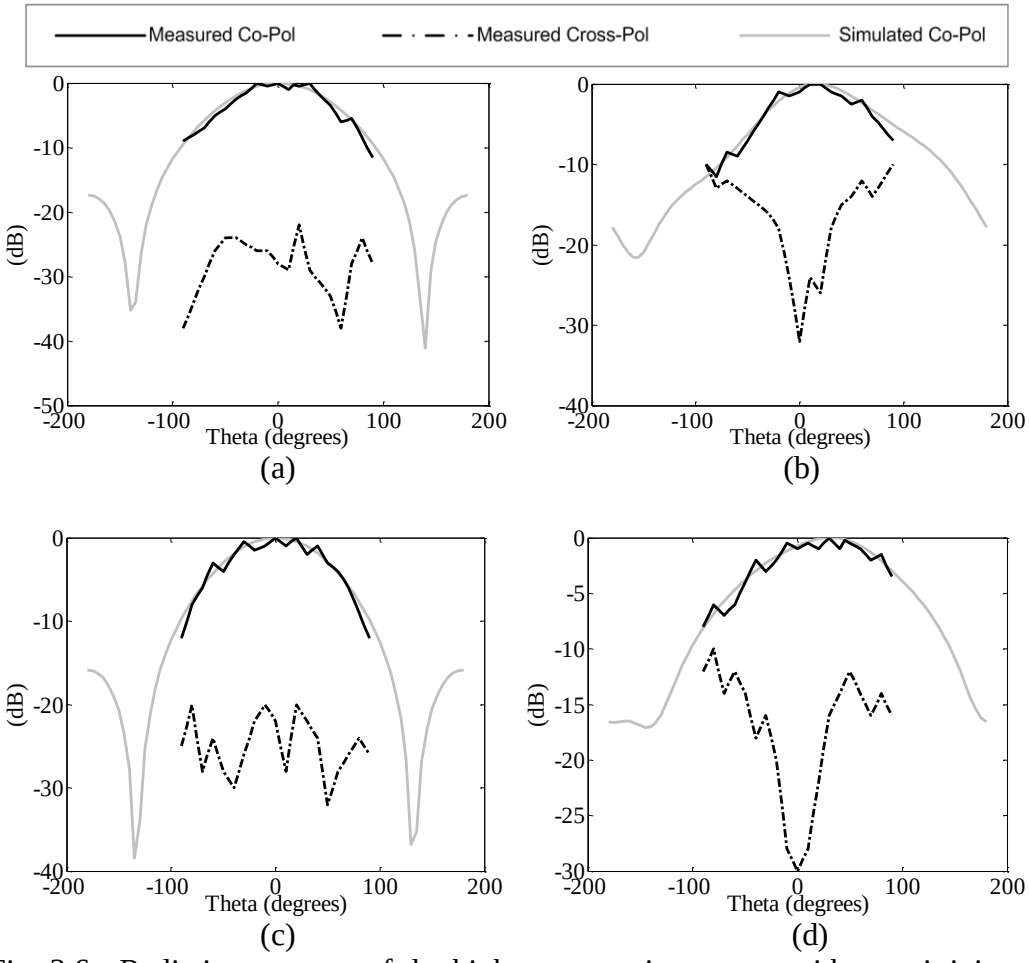

Fig. 3.6. Radiation patterns of the high aspect ratio antenna with permittivity of 37. (a) H (xz)-plane at 7.72 GHz (b) E (yz)-plane at 7.72 GHz (c) H (xz)-plane at 8.23 GHz (d) E (yz)-plane at 8.23 GHz.

Table 3.1 Comparison of predicted (DWM), simulated (HFSS), and measured resonant frequencies of the proposed high-aspect-ratio antennas.

High-Aspect-Ratio Structures	Resonant Frequency (GHz)					
	TE^{x}_{111}			TE^{x}_{113}		
	Measured	Simulated	Predicted	Measured	Simulated	Predicted
No. 1	6.85	6.85	6.12	7.35	7.45	7.22
No. 2	7.72	7.70	7.24	8.23	8.25	8.11

3.1.4 Discussions on Antenna Performance

Based on the closed-form formula derived for stored energy and radiated power of rectangular DRAs, the radiation Q factor of the TE^{x}_{111} of the proposed structure shown in Fig. 3.1 is as follows.

$$Q_{rad} = 2\omega_0 \frac{Stored\ Energy}{Radiated\ Power} = \frac{\varepsilon_r A k_x^2 (k_y^2 + k_z^2)}{5\left[\frac{8k_0}{\pi}\right]^4 Bh\omega_0 \varepsilon_0 (\varepsilon_r - 1)^2} \frac{\left[1 + \frac{\sin(k_x A)}{(k_x A)}\right]}{\sin^2(\frac{k_x A}{2})} \quad (3.5)$$

In addition, the antenna impedance bandwidth can be expressed in terms of radiation quality factor by the following equation [19].

$$BW = \frac{S-1}{Q_{rad}\sqrt{S}} \quad (3.6)$$

in which S is the maximum desired VSWR value.

It is desirable to increase the permittivity of DRAs to miniaturize them. However, it is known that the impedance bandwidth will dramatically decrease by this decision. In fact, the radiation Q factor is roughly proportional to $\varepsilon_r^{1.5}$. This result can be extracted from Equation 3.5 considering that k_x approaches a limiting value as the value of ε_r is increased and the resonant frequency is roughly proportional to $\varepsilon_r^{-0.5}$. Therefore, rising dielectric constant to achieve a miniaturized antenna increases radiation Q factor and consequently decreases antenna bandwidth.

Nevertheless, with higher dielectric constants a significant size reduction is achieved for the proposed antennas while broadband operation is still maintained, as shown in Table 3.2. Moreover, the antenna cross section, which is an important parameter for array miniaturization, is well miniaturized. Fig. 3.7 shows the two fabricated high aspect ratio antennas along with a two segmented dielectric resonator antenna structure. The high aspect ratio antennas are very well miniaturized and show approximately the same bandwidth.

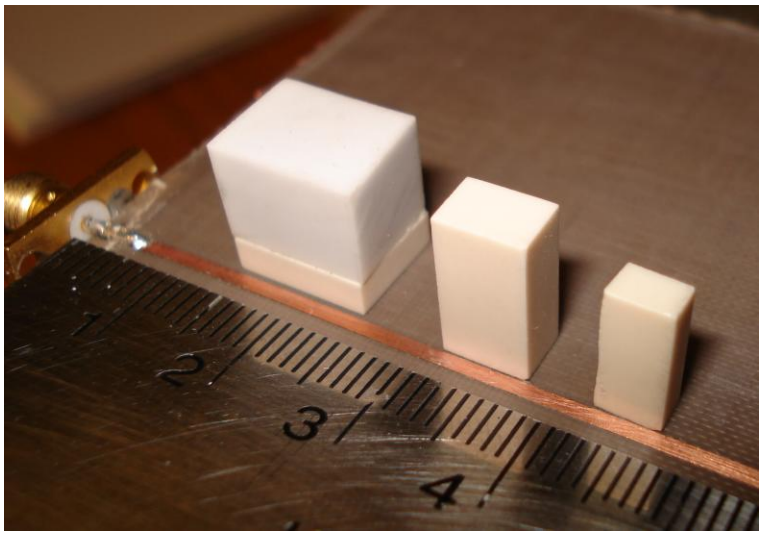

Fig. 3.7. Photograph of the fabricated structures. The ultimate high aspect ratio structure has a volume much less than the other two structures.

Table 3.2 Physical parameters and impedance bandwidth of the high-aspect-ratio antennas. All dimensions are based on wavelength in free space at the center operation frequency of the antennas which are directly fed by a 50 Ω microstripline ($\Delta L \approx 1$ mm) on top of a 15-mil Taconic™ TLY-5 substrate ($\varepsilon_r \approx 2.2$).

High-Aspect-Ratio Structures	Dimensions $A \times B \times h$ (λ_0)	Cross Section $A \times B$ (λ_0^2)	Volume (λ_0^3)	S/V	Meas. Impedance Bandwidth (%)
No. 1 ($\varepsilon_r = 25$)	(0.11 *0.15 *0.29)	0.0165	0.00478	0.9	17
No. 2 ($\varepsilon_r = 37$)	(0.08 *0.12 *0.28)	0.0096	0.00269	1.3	11

There are two main reasons for wideband operation of the high aspect ratio antennas with high dielectric constants. First of all, making high aspect ratio structures shifts the antenna higher order mode, TE^x_{113}, close to the dominant mode. These two modes together can make an enormous change in antenna bandwidth. Second, not only does Q and consequently antenna bandwidth depend on the dielectric constant but it also depends on antenna dimensions. Since it is difficult to see from Equation 3.5 how Q changes with the dimensions, a numerical result is used to demonstrate. The radiation quality factor versus the surface to volume ratio (i.e. S/V) is shown in Fig. 3.8 for the three dielectric constants of 10,

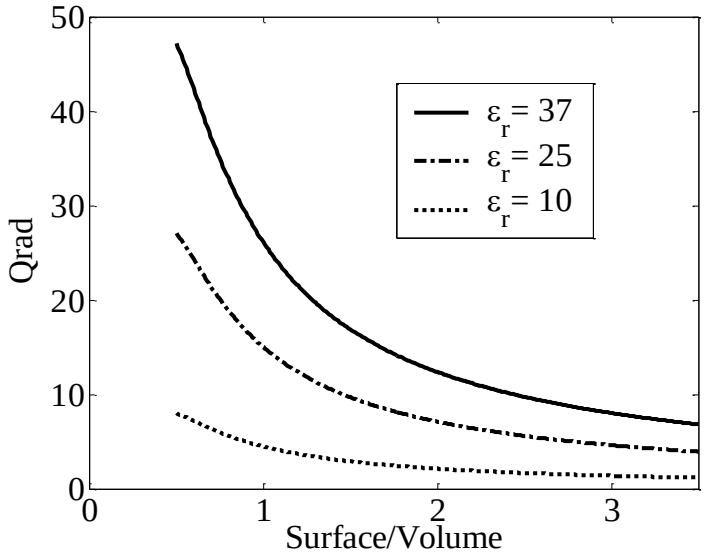

Fig. 3.8. Variation of radiation quality factor (Q_{rad}) with s*urface/volume* (S/V) for different dielectric constants (ε_r).

25, and 37. In this figure it is assumed that $B = 1.5A$ which is approximately true for the proposed structures. Furthermore, to achieve different surface to volume ratios B is changed and h is kept constant at 10 mm. In other words, the antenna height is maintained constant and the antenna cross section is changed while B is kept equal to $1.5A$. As shown in Fig. 3.8, the radiation quality factor decreases with increasing surface to the volume ratio. Therefore, the larger the surface-to-volume ratio, the larger the impedance bandwidth. Besides, radiation quality factor decreases faster with increasing *S/V* for higher dielectric constants. Thus, it is expected that a slight change in *S/V* for antennas with higher dielectric constant dramatically changes the quality factor and consequently the impedance bandwidth. Because *S/V* obtained for different structures in Table 3.2 is gradually increased from 0.6 for the two segmented structure to 1.3 for the high aspect ratio structure with dielectric constant of 37, the fast reduction of impedance bandwidth due to increasing dielectric constant can be mitigated.

It is worth mentioning that there are different ways to augment *S/V* and therefore increase bandwidth. One of the best ways is by making a high aspect ratio structure. For instance, structure No. 2 with an aspect ratio of 7:1 has the *S/V*

equal to 1.3, while structure No. 1 with the aspect ratio of 5.2:1 has the *S/V* equal to 0.9. The other way is by miniaturizing the structure. Upon miniaturization, even with the same aspect ratio, *S/V* increases. For example, miniaturizing all dimensions of a cube with the same factor of 1/2 increases *S/V* by a factor of 2. Therefore increasing *S/V* from 0.9 to 1.3 for the proposed structures is the result of miniaturization as well.

3.2 Anisotropic (Multisegment) Structures

The most common way to produce anisotropic structures is by multilayer design so that each layer has specific properties which are different from the others. These structures have shown many appealing features for antenna applications. For instance, each layer of a two-layer antenna is designed to radiate independently and therefore a multi-band antenna is achieved [14]. Moreover, the bottom layer of a two-layer design is used as an impedance transformer between the upper layer and transmission line resulting in widening the impedance bandwidth of the antenna [11]. When the number of layers is increased to smooth the transition, more improvements are achieved. For instance, three-layer antenna shows better properties than two-layer structure [20]. However, the more layers, the more difficulty to fabricate the structures. In multilayer structures a few micrometers air gap between layers can distort all the desirable results. The difficulty of fabrication will be intensified in millimetre-wave frequencies where the thickness of each layer is around few hundred micrometers.

In this section, the two segmented dielectric resonator antenna (TSDRA) is briefly described and a prototype at lower frequency bands is designed, fabricated and tested [5].

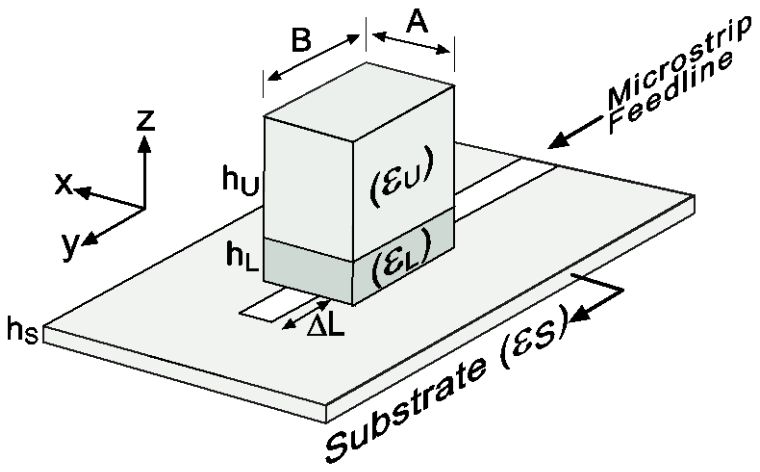

Fig. 3.9. Structure of a microstrip-fed two segmented dielectric resonator antenna.

3.2.1 Theory and Design

Fig. 3.9 illustrates a typical TSDRA. It consists of an upper segment with dielectric constant of ε_U and a lower segment with dielectric constant of ε_L. The antenna working in its dominant TE^{x}_{111} mode is directly fed by a microstrip line. Since a TSDRA is a kind of inhomogeneous DRA, it can be analyzed in the same manner. However, the above mentioned equations cannot be directly used for TSDRA due to this inhomogeneity. Therefore, the equations for the simple DRA should be modified to use in TSDRA. This modification is done by utilizing a weighted average model to calculate the dielectric constant of the whole structure [11], and the argument of effective dimensions to modify the width and the length of the structure [21]. These quantities for the proposed structure are as follows.

$$\varepsilon_{\text{eff}} = \frac{\varepsilon_S h_S + \varepsilon_L h_L + \varepsilon_U h_U}{h_S + h_L + h_U} \tag{3.7}$$

$$A_{eff} = A(1-\frac{1}{\varepsilon_{\text{eff}}}), \quad B_{eff} = B(1-\frac{1}{\varepsilon_{\text{eff}}}) \tag{3.8}$$

A_{eff} and B_{eff} are effective dimensions which depend on physical dimensions and effective permittivity of the resonator. The resonant frequency of TSDRA can be consequently estimated by the following equation.

$$f_r = \frac{h_S f_S + h_L f_L + h_U f_U}{h_S + h_L + h_U} \tag{3.9}$$

in which h_S, h_L, and h_U are the height of the substrate, lower segment and upper segment respectively, and f_S, f_L, and f_U are the resonant frequency of the whole structure made of substrate material, lower segment material, and upper segment material respectively based on modified equations.

In this method it is assumed that the influence of each segment on the resonant frequency of the whole structure is proportional to its height [22]. Furthermore, the resonant frequency like the effective permittivity of the whole structure is derived from the weighted average model. These equations have been shown to predict the resonant frequency with accuracy up to 12 percent, depending on such factors as the relative permittivity and the aspect ratio [11].

Since both TSDRA and the simple rectangular DRA radiate like a horizontal magnetic dipole in their lowest order mode [23], and also most of the stored electric energy lies inside the resonator in both cases, we can expect that the radiation quality factor for TSDRA is roughly the same as the one for a rectangular DRA.

As previously mentioned, the lower segment of TSDRA acts like an impedance transformer between the feedline and the upper segment. For that reason, it can be a dielectric of certain thickness and permittivity to minimize the input reflection coefficient and give the best possible impedance bandwidth [24]. Based on extensive investigations of the effects of different lower segment parameters on TSDRA performance, two quantitative relations have been extracted to predict the optimum lower segment parameters:

$$\varepsilon_{L,opt} = \frac{\eta_0 \sqrt{\varepsilon_U}}{Z_{Line}} \ , \ h_{L,opt} = \frac{c}{4 f_0 \sqrt{\varepsilon_L}} \tag{3.10}$$

These equations along with a procedure were introduced to design wideband TSDRAs [11].

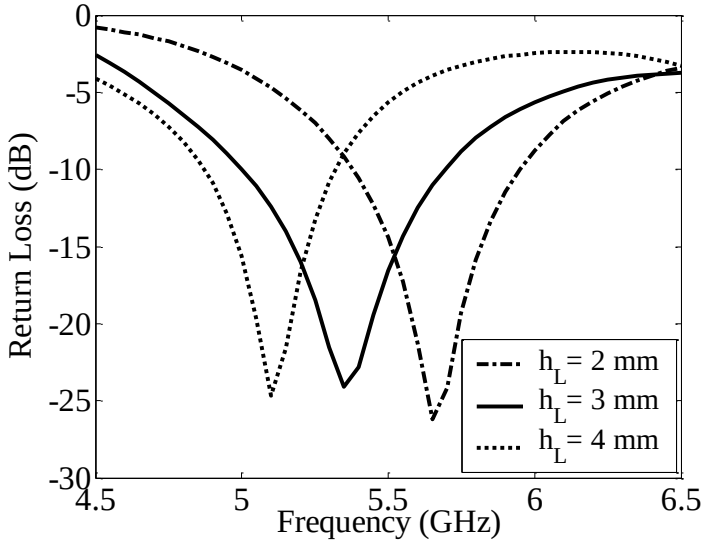

Fig. 3.10. Return loss deviations of the TSDRA when the lower segment thickness is changed. ($\varepsilon_U = 10$, $\varepsilon_L = 25$, $A \times B \times h_U = 9 \times 11.5 \times 9$ mm)

3.2.2 Parametric Study

In this section examples of two segmented antennas are given. In each case, the observed simulation result when certain parameters are varied is presented. All of the simulated designs are fed by a 50 Ω microstrip line on a substrate with ε_s = 2.2, h_s = 0.381 mm, and dielectric loss tangent equal to 0.0009. The simulations are carried out using Ansoft™ HFSS.

A TSDRA with dielectric constant of 10 and dimensions $(A \times B \times h_U)$ of 9 mm, 11.5 mm, and 9 mm for the upper segment can cover 5 to 6 GHz frequency band applications. The permittivity and the height of the optimum lower segment calculated by Equation 3.10 are ε_L = 25 and h_L = 3 mm. Therefore, the resonant frequency of the structure estimated using Equation 3.9 is 5.55 GHz.

Fig. 3.10 shows the simulated return loss of the antenna when the lower segment thickness is changed over the range from 2 mm to 4 mm. The resonant frequency decreases by increasing the lower segment thickness while the impedance bandwidth appears optimum at around 3 mm.

Figure 3.11 illustrates the simulated return loss of the antenna when the lower segment permittivity is changed from 15 to 30. Again, the resonant frequency

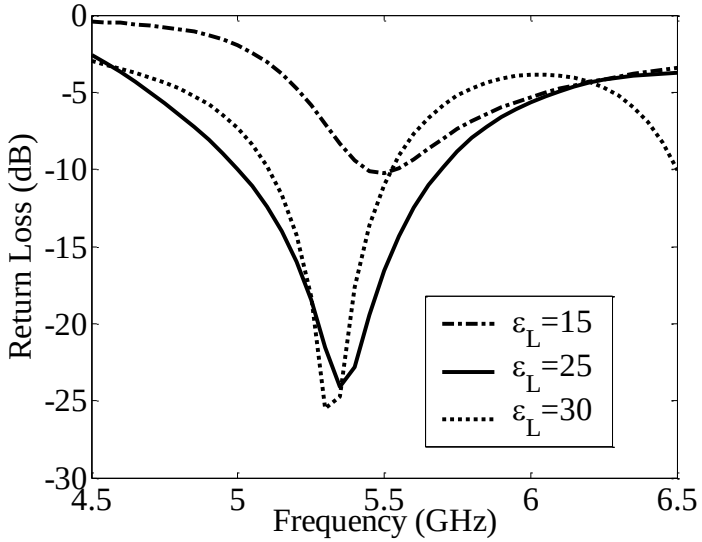

Fig. 3.11. Return loss deviations of the TSDRA when the lower segment permittivity is changed. (ε_U = 10, h_L = 3 mm, $A \times B \times h_U$ = 9 × 11.5 × 9 mm)

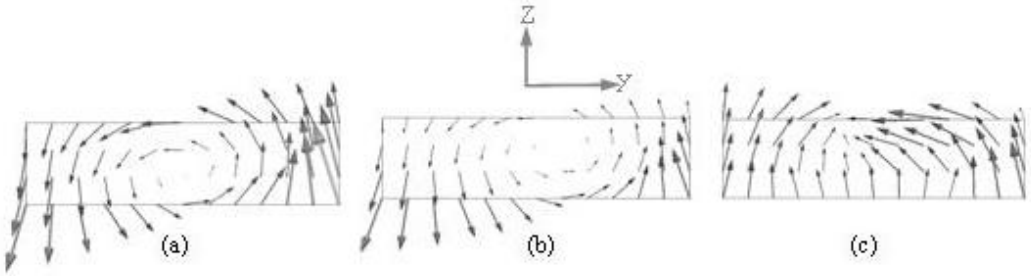

Fig. 3.12. Electric field distributions inside the lower segment of the resonator for (a) 5 GHz, (b) 6 GHz, and (c) 7 GHz. (ε_U = 10, ε_L = 25, $A \times B \times h_U$ = 9 × 11.5 × 9 mm, h_L = 3 mm)

decreases by increasing the lower segment permittivity while the impedance bandwidth appears optimum at around ε_L = 25. As predicted, the return loss of the antenna with lower segment permittivity of 15 barely touches the -10 dB level.

In all cases the ΔL is adjusted to achieve the maximum bandwidth. It should be noted that when the dielectric constant of the lower segment increases to more than 30 or its thickness increases to more than 4 mm, its second resonant frequency, TE^{x}_{121}, approaches the operating frequency of the TSDRA, making it an ineffective radiator with high cross polarizations.

The electric field distribution of the optimum lower segment is depicted at 5 GHz, 6 GHz, and 7 GHz in Figure 3.12. The frequency 6 GHz is near the first

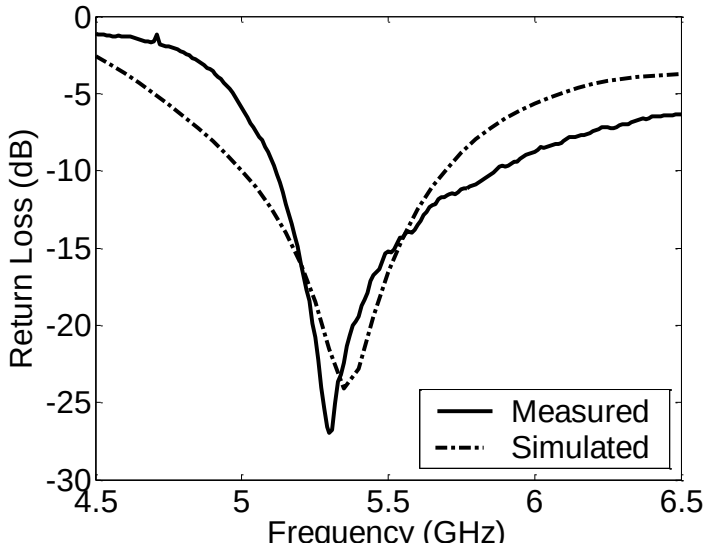

Fig. 3.13. Measured and simulated return loss of the TSDRA. (ε_U = 10, ε_L = 25, $A \times B \times h_U$ = 9 × 11.5 × 9 mm, h_L = 3 mm)

resonant frequency and 7 GHz is near the second resonant frequency of the lower segment. As shown, although the electric field distributions at 5 GHz and 6 GHz are similar, the field distribution at the second resonant frequency is completely different.

3.2.3 Experimental Result

A TSDRA similar to the optimum structure simulated above was fabricated and measured [5]. The antenna is made from TransTech's materials and fed by a 50 Ω microstrip line designed on top of 15 cm by 10 cm ground plane. The substrate is a 15-mil thick Taconic's TLY-5 with ε_r = 2.2 and $tan\ \delta_e \leq 0.0009$. The antenna has a cross section of 11.5 mm by 9 mm, 9 mm height for the upper segment, and 3 mm height for the lower section. The upper segment, made from SMAT10 with dielectric constant of 10 and $tan\ \delta_e \leq 0.00015$, and the lower segment, made from MCT25 with dielectric constant of 25 and $tan\ \delta_e \leq 0.0015$, are put together with RTV silicone adhesive to construct the antenna structure. The measured and simulated return losses are shown in Fig. 3.13. The measured –10 dB bandwidth is 14 percent. Discrepancies between the results are mainly due to the thin layer of

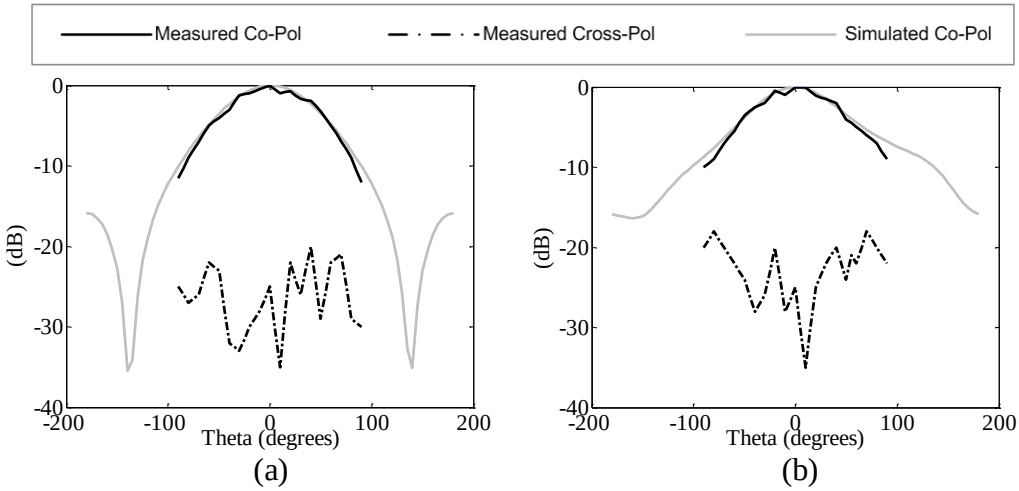

Fig. 3.14. TSDRA radiation patterns at the resonant frequency. (a) H (xz)-plane and (b) E (yz)-plane. (ε_U = 10, ε_L = 25, $A \times B \times h_U$ = 9 × 11.5 × 9 mm, h_L = 3 mm)

adhesive between the two segments of the antenna and also an air gap between the lower segment and the flexible ground plane.

The measured and simulated radiation patterns in the E and H planes at the resonant frequency of the TSDRA are shown in Figure 3.14. The TSDRA similar to a DRA radiates like a horizontal magnetic dipole in its dominant mode. The antenna gain at the resonant frequency is roughly 5.5 dBi. The measured resonant frequency of the fabricated antenna is 5.30 GHz which is very close to the simulated (5.35 GHz) and predicted (5.55 GHz) resonant frequencies.

3.3 Slot-Fed Low-Permittivity DRA

As discussed in previous section, low permittivity materials are preferred to increase the impedance bandwidth of the DRA. In the X-ray lithographic fabrication point of view, since the photoresist materials have relatively low dielectric constant (typically 2-4) and it still remains low even after they are mixed with small portions of microwave materials, the possibility of utilizing very low dielectric constant materials may also facilitate lithographic fabrication processes particularly for millimetre-wave applications. To best of my knowledge, this approach introduces polymer (plastic) resonator antennas for the first time. However, the approach may suffer from feeding the low permittivity polymers.

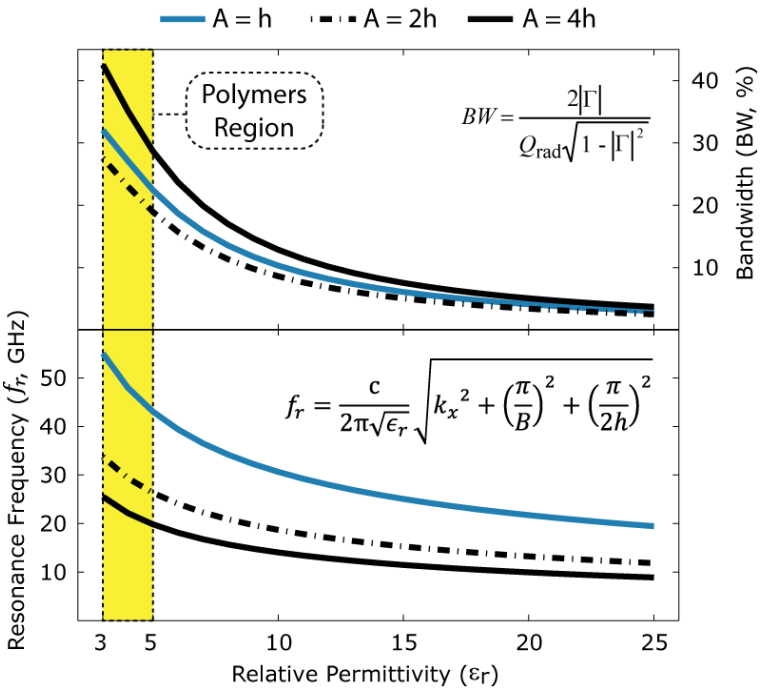

Fig. 3.15. Impedance bandwidth and resonant frequency vs. dielectric constant of the rectangular DRA. $|\Gamma|$ is the reflection coefficient value (*-10 dB* is considered here).

This problem has been addressed in the current and following sections using slot-fed and strip-fed excitation schemes. A DRA-slot hybrid antenna is introduced and multi-resonance ultra wideband operation is shown using strip-fed excitation.

3.3.1 Theory and Concept

It is well known that polymer materials have very low relative permittivity which can increase the resonant frequency and impedance bandwidth of the antenna while decreasing the radiation quality factor. The degree of this dependence is shown in Fig. 3.15 for a rectangular structure with cross section of $A \times B$, height of $2h$, and permittivity of ε_r. It is supposed that A in the x direction be equal to B in the y direction, and h be kept constant at 2 mm. Three geometric cases are considered, square ($A = 2h$), high aspect ratio ($A = h$), and low profile ($A = 4h$) structures.

A range of dielectric constant is indicated as the polymer region in Fig. 3.15. Most polymers with microwave applications have permittivities that lie in this

region or very close to it. For instance, liquid crystal polymer (LCP) [25], polydimethylsiloxane (PDMS) [26], and polyoxymethylene (POM) [27] have the permittivity of 3.1, 2.7, and 3.7 respectively. With small portions of additives (e.g. ceramic powder), on the other hand, many microwave polymers can be moved into the region while the fabrication advantages of polymers are maintained. For example, adding 10 volume percent Mg-Ca-Ti (MCT) or Bi-Ba-Nd-Titanate (BBNT) moves the permittivity of PDMS to 4.5 and 4.1 respectively and the elastic behavior of PDMS is still maintained for special microwave applications [26].

A polymer-based low profile structure with dielectric constant of 4 can result in a bandwidth of 35.2% at 22.1 GHz frequency, as derived from Fig. 3.15, while these values are 12.8% and 14.1 GHz respectively for a ceramic antenna with dielectric constant of 10. This shows that the bandwidth is almost tripled and resonant frequency is increased by 56%. Similar variations in bandwidth and resonant frequency are achieved for the other two structures, although the high aspect ratio and low profile DRAs have larger bandwidth (smaller Q_{rad}) than square shaped resonators due to higher surface to volume ratio [5]. Therefore, very low permittivity polymer-based materials, besides their fabrication advantages, could considerably improve antenna performance especially at millimetre-wave frequencies in which expanding antenna dimensions are better tolerated.

3.3.2 Slot-Coupled Excitation

To fulfill the feeding requirements of polymer-based DRAs, a slot-coupled excitation method is used and the structure is analyzed using numerical methods in the frequency domain (Ansoft ™ HFSS).

A diagram of the slot-coupled structure is shown in Fig. 3.16. Both the aperture and resonator positions are adjusted to be in the middle of the ground plane to attain a symmetrical geometry. It is supposed that the dielectric resonator

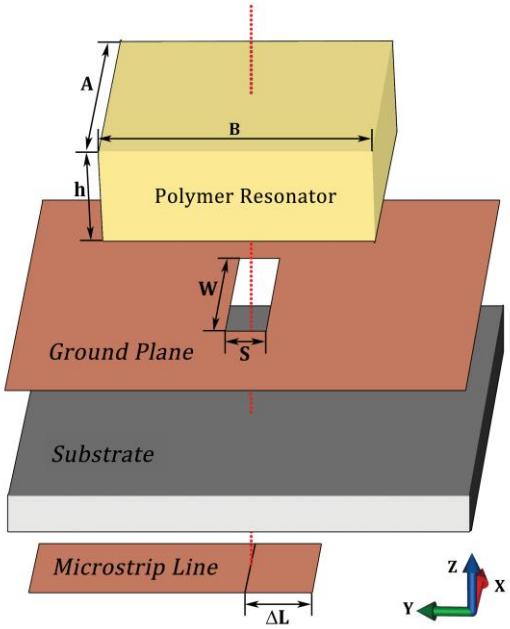

Fig. 3.16. Explosive view of slot-coupled antenna.

with permittivity of ε_r = 4 has dimensions of $A = B$ = 5.7 mm and h = 2 mm. The resonator is fed by the aperture through a 50 Ω microstrip line designed on the bottom of a substrate with dielectric constant of 2.2. The aperture size (W, S) and microstrip length variation (ΔL) are changed in order to improve impedance matching. Fig. 3.17(a) shows the reflection coefficient of the antenna for different aperture sizes. Two resonant frequencies are quite obvious in this figure. The lower resonant frequency increases with smaller slots from ~13 GHz to ~18 GHz, and therefore is related to the slot radiation. The upper resonant frequency remains fixed at ~26 GHz and is due to the DRA radiation. The magnetic field distribution inside the resonator at 26 GHz is shown in Fig. 3.17(b). The distribution is equivalent to a horizontal magnetic dipole and confirms that it is due to the dominant TE^{x}_{111} mode of the low permittivity DRA. It can be concluded that the polymer-based DRA with low permittivity of ε_r = 4 could achieve high coupling of -26 dB and 28 % (-10 dB) impedance bandwidth.

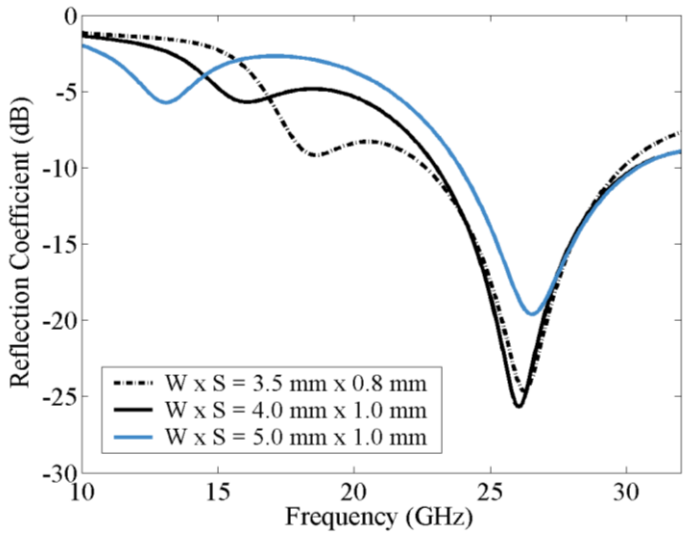

(a)

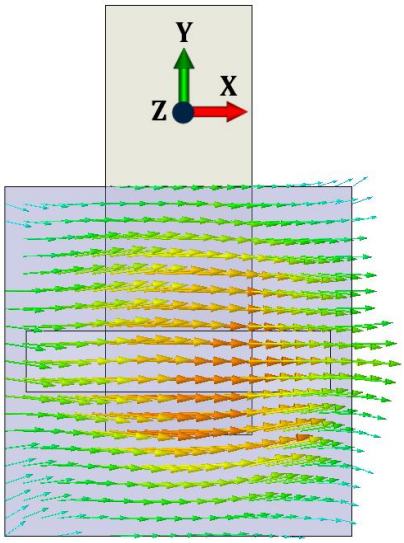

(b)

Fig. 3.17. Slot-coupled DRA with permittivity of 4. (a) Reflection coefficients with different slot sizes; (b) Top view of the magnetic field distribution inside the resonator at 26 GHz.

3.3.3 Comparison

The characteristics of polymer-based DRAs with low permittivity (ε_r = 4) are compared with higher permittivity ceramic DRAs (ε_r = 10). Similar dimensions of 5.7 mm by 5.7 mm by 2.0 mm are considered for both cases. The comparisons and discussions are based on Ansoft ™ HFSS FEM simulations and, as shown in

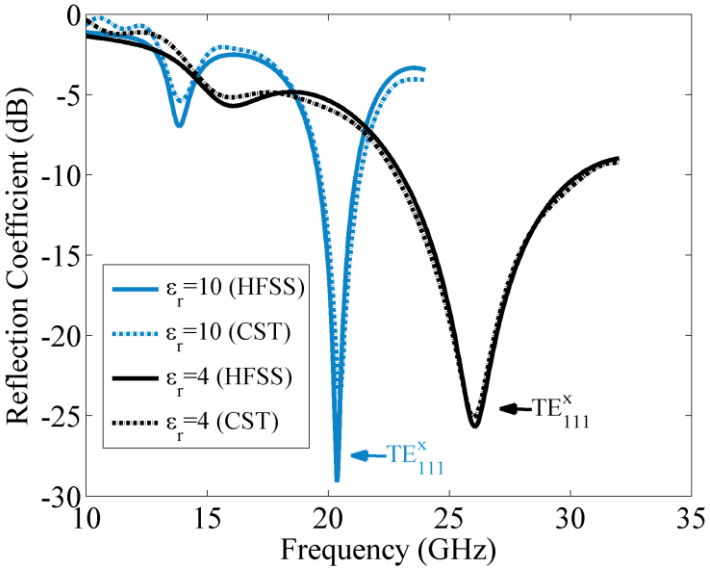

Fig. 3.18. Comparison of reflection coefficients of slot-coupled DRAs with high and low permittivities. ($A \times B \times h$ = 5.7 × 5.7 × 2 mm, more structural details are mentioned in Table 3.3)

the following table and figure, are confirmed by CST ™ Microwave Studio FIT results.

Fig. 3.18 shows the reflection coefficients of ceramic and polymer-based antennas. The -10 dB impedance bandwidth from 23.0 GHz to 30.4 GHz is achieved for the polymer-based antenna, while the impedance bandwidth is from 19.5 GHz to 21.2 GHz for the ceramic antenna. The achieved coupling for the polymer-based antenna is quite comparable to the coupling of the ceramic DRA. The obtained impedance bandwidths are the result of TE^{x}_{111} mode radiation for both cases. Table 3.3 shows the slot dimensions, slot and DRA resonances, antenna impedance bandwidths, and directivity at the DRA resonance for the slot-coupled very low permittivity polymer-based antenna and ceramic DRAs with higher permittivity. The antennas having moderate permittivities are also analysed and the results are depicted for comparison. In order to achieve the best impedance matching for lower permittivity antennas, the slot length is increased

Table 3.3 Physical parameters and simulation results of slot-coupled DRAs. The proposed antennas have the same dimensions of 5.7 mm by 5.7 mm by 2 mm.

Dielectric Constant	Slot Dimensions (mm)	ΔL (mm)	Slot Resonance (GHz)		TE^{x}_{111} Resonant Frequency (GHz)		-10 dB Impedance Bandwidth (GHz)		-10 dB Impedance Bandwidth (%)		Directivity at TE^{x}_{111} Resonance (dBi)	
			HFSS	CST-MS	HFSS	CST-MS	HFSS	CST-MS	HFSS	CST-MS	HFSS	CST-MS
4 (Polymer)	4.0 × 1.0	1.2	16.1	16.0	26.1	26.0	23.0~30.4	22.8~30.6	27.7	29.2	5.6	5.7
6	4.0 × 1.0	1.1	13.9	13.8	23.2	23.1	21.0~25.9	20.9~25.9	20.9	21.4	5.6	5.7
8	3.5 × 0.8	1.0	13.9	13.7	21.3	21.2	19.9~22.7	19.8~22.7	13.2	13.7	5.7	5.8
10 (Ceramic)	3.0 × 0.7	0.9	13.8	13.6	20.4	20.4	19.5~21.2	19.4~21.3	8.4	9.3	5.9	6.0

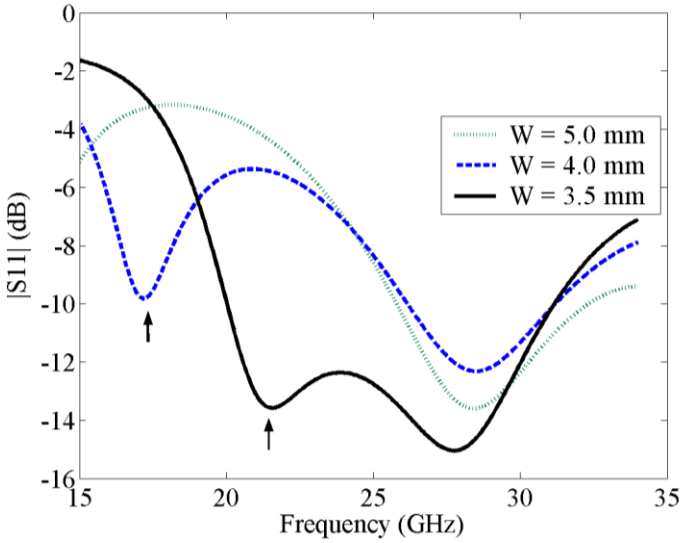

Fig. 3.19. Reflection coefficients of polymer-slot antenna. ($A \times B \times h$ = 5.7 × 5.7 × 2 mm, ε_r = 3.5, W/S = 5)

from *3.0 mm* to *4.0 mm*. However, the slot resonant frequencies remain far from the DRA resonant frequencies for all cases. The TE^x_{111} resonant frequency is about 30% increased from 20.4 GHz for the ceramic DRA, to 26.1 GHz for the polymer-based DRA. On the other hand, the -10 dB impedance bandwidth is tripled from 8.4 percent to 27.7 percent. The directivity of the antenna does not dramatically change and remains around 5.6 dBi ~ 6.0 dBi for all cases. It should be noted that lowering the permittivity of the DRA from 4 to 2 leads to very poor coupling between the antenna and feed, restricting direct application as antenna structures.

3.3.4 Hybrid Antenna

A huge improvement can be achieved when the DRA is mixed with another type of antenna. For instance, the impedance bandwidths of antennas are added up to have a wideband antenna if similar radiation patterns exist between antennas. Our current work is concentrated on mixing low permittivity polymer resonator antennae and slot antennae to achieve wideband performance.

Fig. 3.19 shows Ansoft™ HFSS simulated reflection coefficients of a polymer resonator antenna with ε_r = 3.5 as the aperture size is varied from W = 5.0 mm to

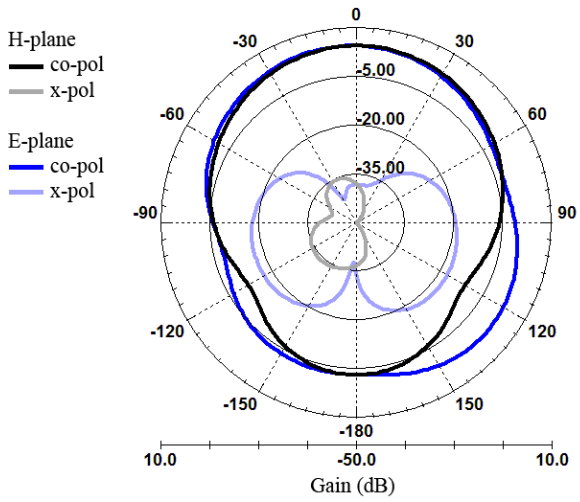

(a)

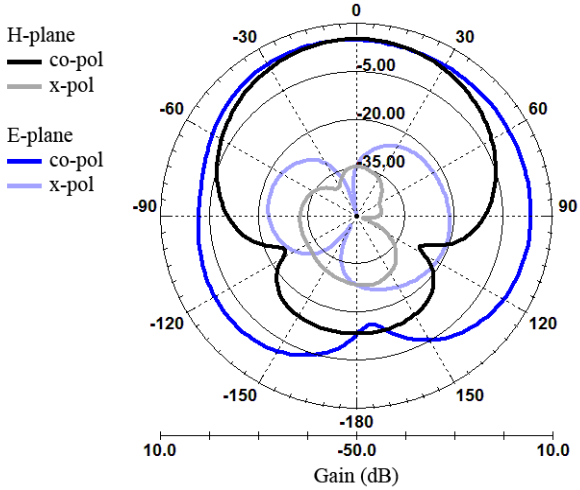

(b)

Fig. 3.20. Radiation patterns at (a) 21 GHz; (b) 28 GHz. ($A \times B \times h$ = 5.7 × 5.7 × 2 mm, ε_r = 3.5, W = 5 mm, S = 1 mm, ΔL = 1 mm)

W = 3.5 mm. The dimension ratio of the aperture (W/S) is maintained at 5 for all cases. The antenna structure is shown in Fig. 3.16 and the polymer is symmetrically positioned on the aperture and ΔL is adjusted (around 1 mm) to achieve the best possible coupling. The upper resonance mainly stays fixed at around 28 GHz while the lower resonance, shown by arrows in Fig. 3.19, shifts up with decreasing aperture dimensions. Simulated E-plane and H-plane radiation patterns of the antenna for W = 3.5 mm at the lower resonance frequency (21 GHz) and upper resonance frequency (28 GHz) are shown in Fig. 3.20(a) and (b), respectively. Similar radiation patterns with low cross polarization levels are

obtained. However, the level of back radiations at 28 GHz is lower than the 21 GHz level. The results of reflection coefficients and radiation patterns confirm that the lower resonance is related to the aperture and the upper resonance is related to the polymer. With this proper design, a hybrid polymer-slot resonator antenna with -10 dB impedance bandwidth of about 20 GHz ~ 32 GHz is achieved.

3.4 Strip-Fed Low-Permittivity DRA

Among available excitation schemes, the microstrip line feed provides simplicity, reproducibility in any form by lithographic technology, and capability of integration with MMICs. This excitation method was used in Section 3.1 to feed high permittivity DRAs effectively. Narrow impedance bandwidth of the antenna (due to the high permittivity of the resonator) was fixed using two resonant modes of the high aspect ratio structure. Hybrid antennas are another solution to present wideband or multiband microstrip-fed antennas. For instance, a combination of a T-shaped microstrip patch and circular disk dielectric resonator is utilized as a hybrid antenna for multiband applications [28]. The bandwidth of microstrip-fed DRAs can be increased by decreasing the dielectric constant of the resonator and enhancing the coupling between the resonator and the feedline by using different feedline shapes (e.g. step-shaped in [29-30] and T-shaped in [31]). Furthermore, an open-ended strip printed on the sidewall of microstrip-fed cylindrical DRAs with permittivities of 16 and 10 increased the impedance bandwidth to 10% and 19%, respectively [32]. In this section, microstrip transmission line with a vertical strip is used to excite polymer-based antennas with permittivity as low as 4. Due to the low permittivity of the structure, the frequency distance between appropriate modes is reduced and consequently multimode wideband antennas are achieved. The effect of the open-ended strip on antenna performance is examined. Improvements on the impedance bandwidth are discussed.

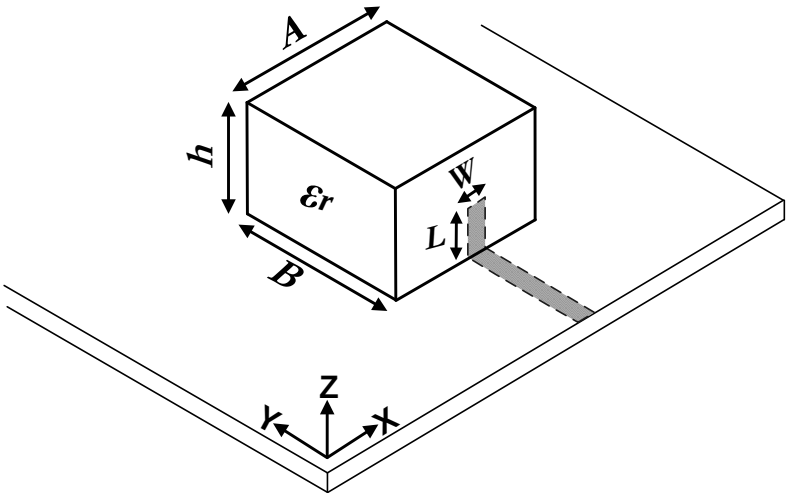

Fig. 3.21. Strip-fed antenna structure.

3.4.1 Parametric Study

A diagram of the antenna structure is shown in Fig. 3.21. The resonator is placed on a substrate with permittivity of 2.2, and fed by a 50 Ω microstrip line continuing up the side wall of the resonator to construct the strip-fed DRA. The resonator with permittivity of ε_r has a cross section of $A = B = 5.7$ mm and height of $h = 2$ mm. Length (L), width (W), and thickness of the vertical strip are adjusted to achieve the best coupling between the strip and resonator. The following parametric studies are carried out using HFSS^{TM} simulator.

First the permittivity of the resonator is changed and its effects on the reflection coefficient of the antenna are examined. Fig. 3.22 shows the reflection coefficients of the DRA with ε_r = 10, 8, 6, and 4. Two resonant frequencies are obvious in this figure for each case. At the first resonant frequency, the amount of maximum coupling (power transferred from the transmission line to the antenna) increases by increasing the antenna permittivity. At the second resonant frequency, the amount of maximum coupling increases by decreasing the antenna permittivity. The resonant frequency of the lower mode shifts up with lower permittivity while the upper resonance does not follow any regular pattern with respect to the resonator permittivity. It is at 24 GHz for ε_r = 10 and 8, at 23.5 GHz for ε_r = 6, and increases to 27.5 GHz for ε_r = 4. This irregularity is related

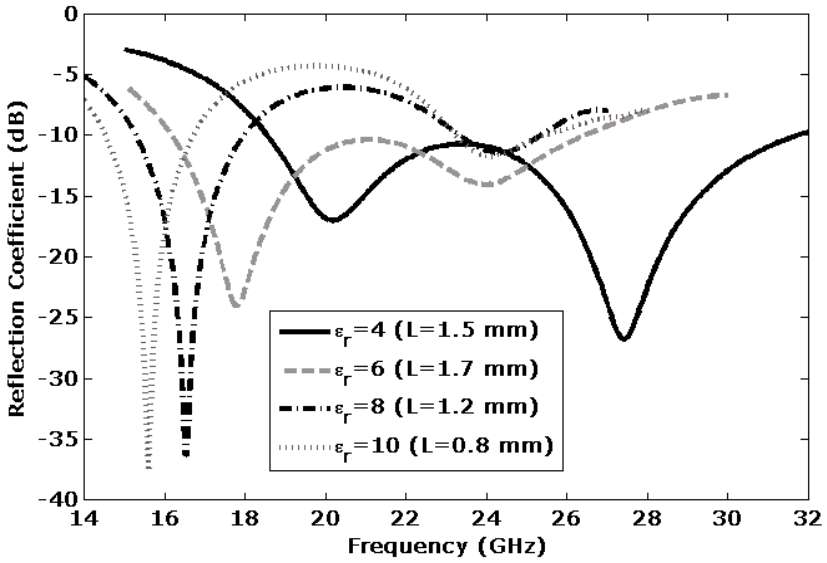

Fig. 3.22. Variation of reflection coefficients of the antenna when the resonator permittivity is changed. Width (W) and thickness of the vertical strip are adjusted to be 2.0 mm and 10 μm respectively. Strip length (L) is optimized to achieve the best impedance matching. ($A \times B \times h = 5.7 \times 5.7 \times 2$ mm)

to strip length (L) which is adjusted to achieve the best impedance matching. For the two lower permittivity cases (4 and 6), the impedance bandwidth of the individual modes increases and therefore the two separate -10 dB bandwidths are combined to create wideband dual-mode antennas.

Fig. 3.23(a) and (b) show the reflection coefficients of these two antennas for different strip lengths. Two kinds of variations, shown by arrows, are notable in these figures. First, strong couplings are achieved for the first resonant mode when the strip length increases. Second, the resonant frequency of the upper mode shifts down with increasing strip length, therefore controlling the frequency distance between two individual modes. To have as wide impedance bandwidth as possible, the strip length should be kept in a specific range depending on the dielectric constant of the resonator. The impedance matching is not sensitive to the width (varied from 1.6 mm to 2.4 mm) and the thickness (varied from 1 μm to 200 μm) of the vertical strip.

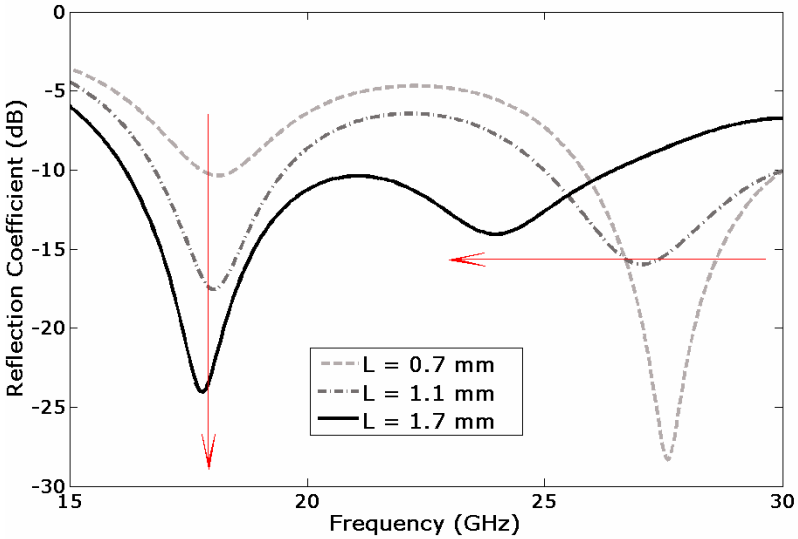

(a)

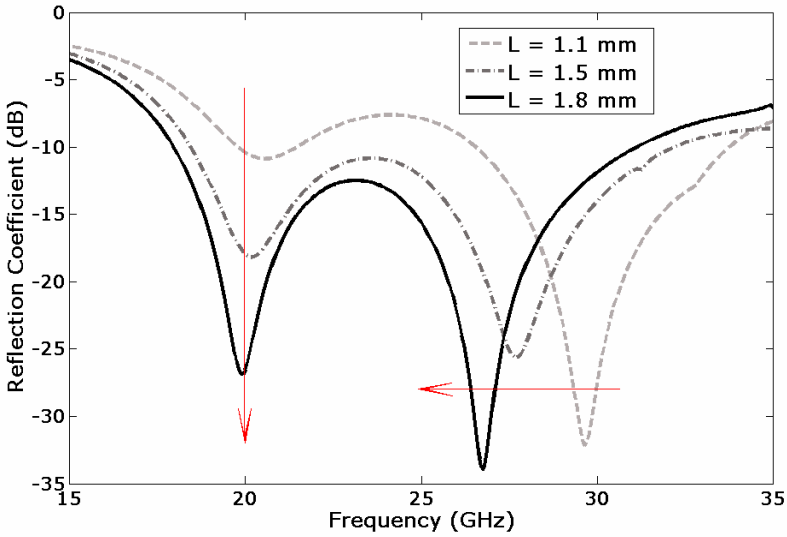

(b)

Fig. 3.23. Variation of reflection coefficients of the antenna when the strip length is changed. (a) ε_r = 6 and (b) ε_r = 4.

The electric field distributions are investigated to identify the resonant modes. Fig. 3.24(a) and (b) show the electric field vectors at the resonances inside the DRA with permittivity of 4. The distribution at the lower resonant frequency is similar to a quarter circle in the region between the vertical strip (L = 1.5 mm) and ground plane (z = 0), as illustrated in Fig. 3.24(a). This is related to the dominant mode of TE^{x}_{111} with short circuited fields based on Image Theory. Using a similar

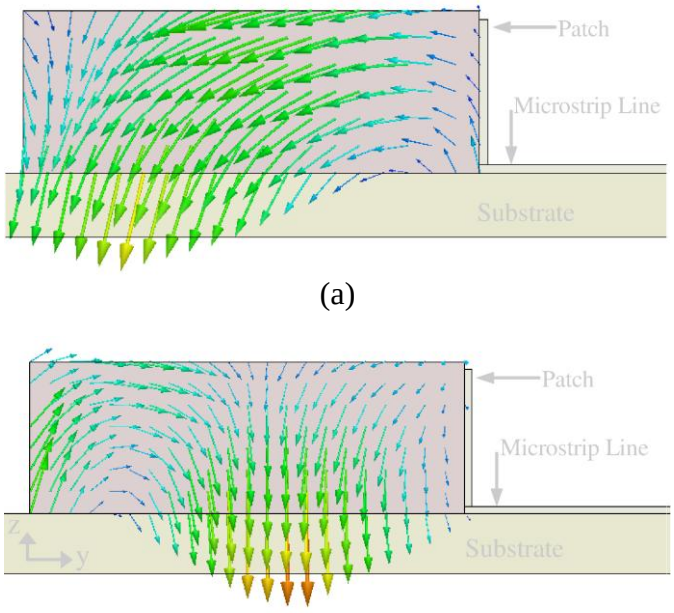

Fig. 3.24. Electric field distributions inside the polymer-based resonator at (a) 20 GHz and (b) 27 GHz.

interpretation, one can find that the second resonant mode is related to the higher order mode of TE^{x}_{131}. The electric fields of TE^{x}_{121} mode, which are equivalent to two opposite magnetic dipoles and therefore cannot radiate efficiently, could not satisfy the boundary condition due to the presence of the lengthy strip. It is worth mentioning that TE^{x}_{111} and TE^{x}_{131} are equivalent to a horizontal magnetic dipole in the *x* direction and consequently should radiate similarly.

3.4.2 Ultra Wideband Operation

The low permittivity of the polymer antenna results in larger impedance bandwidth for individual modes. This enlargement in bandwidth reduces the frequency distance between individual modes and makes a multi-mode wideband antenna which could not be easily produced by ceramic antennas with higher permittivities and longer frequency distance between radiation modes. In the current work, a vertical strip connected to the microstrip line excites the odd modes (i.e. TE^{x}_{111} and TE^{x}_{131}) of the polymer-based resonator antenna with a

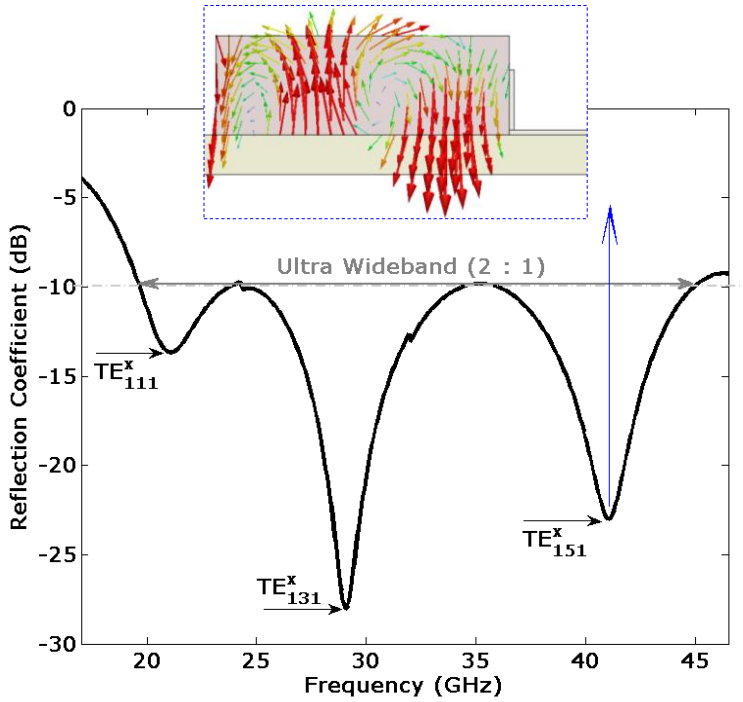

Fig. 3.25. Reflection coefficient of the rectangular-shape multi-mode antenna. Electric field distributions at the third resonant frequency, shown in a dash-dash block, belong to the TE^{x}_{151} mode.

permittivity as low as 4. The even modes (i.e. TE^{x}_{121} and TE^{x}_{141}), which are non radiating modes and usually increase the cross polarization levels over the bandwidth, are removed using the special boundary condition enforced by the vertical open-ended strip.

Further bandwidth enhancement can be achieved by using rectangular shapes instead of the square shape geometries. For instance, a rectangular antenna ($A \times B \times h = 4 \times 6 \times 2$ mm, $\varepsilon_r = 4$) excited using a vertical strip ($W \times L = 2 \times 1.25$ mm) is a 2:1 ultra wideband DRA. Fig. 3.25 shows the simulated reflection coefficient of this antenna. The ultra wideband operation is due to the excitation of the dominant mode of TE^{x}_{111} and higher order modes of TE^{x}_{131} and TE^{x}_{151}.

3.5 Summary

Two approaches, high aspect ratio and two segmented structures, were examined to improve the size and impedance bandwidth of microstrip-fed

rectangular DRAs. It was shown that dual-mode operation inherent to all microstrip-fed high aspect ratio DRAs can be exploited with high aspect ratio structure for bandwidth enhancement while an enormous size reduction can be achieved by choosing high permittivity materials. Moreover, the identical radiation characteristic of these modes allows preservation of the radiation patterns and polarization over the entire bandwidth. More than 70 percent cross section miniaturization and 50 percent volume miniaturization, along with wideband operation of high aspect ratio structures make them a strong alternative for array applications.

Additional enhancements in impedance bandwidth may be achieved by incorporating the high aspect ratio and two segmented DRA techniques when antenna miniaturization is not an important issue. For instance, antenna dimensions at millimeter-wave frequencies are intrinsically small enough so that both techniques can be exploited to increase the impedance bandwidth. Ansoft™ HFSS simulations show at least 30% bandwidth at 24 GHz with the maximum antenna dimension less than 3.5 mm.

It was also shown that polymer-based resonator structures with permittivity as low as 4 can be utilized as wideband antennas with various fabrication advantages. Resonant frequency and impedance bandwidth of DRAs in the polymer region (ε_r = 3 ~ 5) were discussed and compared with higher permittivity DRAs. The microstrip slot coupling and vertical open-ended strip enable effective excitation of the low permittivity resonators and realization of the polymer-based resonator antennas with improved performance. The vertical open-ended strip introduces a new degree of freedom for the antenna designer to tune the higher resonant frequencies to achieve multiband or wideband operation. By adjusting antenna dimension and exciting three resonant modes with identical radiation patterns, a 2:1 ultra wideband antenna can be achieved. The possibility of utilizing softer materials like polymers as very low permittivity dielectrics in the fabrication of millimetre-wave DRAs facilitates simple fabrication processes for

conventional structures, and also enables fabrication of small structures with fine features and complex geometries through lithographic batch fabrication.

References

[1] A. Rashidian and D. M. Klymyshyn, "Strip-fed excitation of very low permittivity dielectric resonator antennas," *Asia-Pacific Microwave Conference (APMC 2008)*, Hong Kong, December 2008.

[2] A. Rashidian and D. M. Klymyshyn, "Microstrip-fed high aspect ratio dielectric resonator antenna with dual-resonance, broadband characteristics," *IET (IEE) Electronics Letters*, vol. 45, no. 2, pp. 94-95, January 2009.

[3] A. Rashidian and D. M. Klymyshyn, "Very low permittivity slot-fed dielectric resonator antennas with improved bandwidth for millimeter-wave applications," *European Conference on Antennas and Propagations (EuCAP 2009)*, Berlin, Germany, March 2009.

[4] A. Rashidian and D. M. Klymyshyn, "A novel approach to enhance the bandwidth of miniaturized microstrip-fed dielectric resonator antennas," *European Conference on Antennas and Propagations (EuCAP 2009)*, Berlin, Germany, March 2009.

[5] A. Rashidian and D. M. Klymyshyn, "On the two segmented and high aspect ratio dielectric resonator antenna for bandwidth enhancement and miniaturization," *IEEE Transactions on Antennas and Propagation*, vol. 57, no. 9, pp. 2775-2780, Sep. 2009.

[6] A. Rashidian, D. M. Klymyshyn, M. Tayfeh Aligodarz, M. Boerner, and J. Mohr, "Development of polymer-based dielectric resonator antennas for millimeter-wave applications," *Progress In Electromagnetics Research C (PIER C)*, vol. 13, pp. 203−216, 2010.

[7] A. Rashidian, D. M. Klymyshyn, M. Tayfeh Aligodarz, M. Boerner, and J. Mohr, "Photoresist-based polymer resonator antennas: lithography fabrication,

strip-fed excitation, and multimode operation," *IEEE Antennas and Propagation Magazine*. Accepted for publication Nov. 27, 2010.

[8] M. Tayfeh Aligodarz, K. Forooraghi, and A. Rashidian, "Wideband miniaturized fractal clover leaf microstrip patch antenna," *International Symposium on Antennas (JINA)*, pp.164-165, 2004.

[9] O'Keefe, S. G., S. P. Kingsley, and S. Saario, "FDTD simulation of radiation characteristics of half-volume HEM and TE-mode dielectric resonator antennas," *IEEE Trans. on Antennas and Propagat.*, vol. 50, no. 2, pp. 175–179, 2002.

[10] R. K. Mongia, A. Ittipiboon, and M. Cuhaci, "Low profile dielectric resonator antennas using a very high permittivity material," *Electronics Letters*, vol. 30, no. 17, pp. 1362-1363, August 1994.

[11] A. Rashidian, K. Forooraghi, and M. Tayfeh Aligodarz, "Investigations on two-segment dielectric resonator antennas," *Microwave and Optical Technology Letters*, vol. 45, no. 6, pp. 533-537, June 2005.

[12] A. Ittipiboon, A. Petosa, and S. Thirakoune, "Bandwidth enhancement of a monopole using dielectric resonator antenna loading," *Proc. ANTEM Conf.*, pp. 287-290, Aug. 2002.

[13] K. P. Esselle and T. S. Bird, "A hybrid-resonator antenna: experimental results," *IEEE Transactions on Antennas and Propagation*, vol. 53, no. 2, pp. 870-871, Feb. 2005.

[14] P. Rezaei, M. Hakkak, and K. Forooraghi, "Design of wide-band dielectric resonator antenna with a two-segment structure," *Progress In Electromagnetics Research*, PIER 66, pp. 111-124, 2006.

[15] G. Bit-Babik, C. Di Nallo, and A. Faraone, "Multimode dielectric resonator antenna of very high permittivity," *IEEE Antennas and Propagat. Society International Symposium*, vol. 2, pp. 1383-1386, June 2004.

[16] B. Li and K. W. Leung, "Strip-fed rectangular dielectric resonator antennas with/without a parasitic patch," *IEEE Trans. on Antennas and Propagat.*, vol. 53, no. 7, pp. 2200–2207, July 2005.

[17] K. M. Luk and K. W. Leung, *Dielectric Resonator Antennas*. London: Research Studies Press LTD., 2003.

[18] ANSI/IEEE Std 149-1979 (Revision of IEEE Std 149-1965), IEEE standard test procedures for antennas. 1979.

[19] R. K. Mongia and P. Bhartia, "Dielectric resonator antennas- a review and general design relations for resonant frequency and bandwidth," *International Journal of Microwave and Millimeter-Wave Computer-Aided Engineering*, vol. 4, no. 3, pp. 230-247, 1994.

[20] W. Huang and A. A. Kishk, "Compact wideband multi-layer cylindrical dielectric resonator antennas," *IET Microw. Antennas Propag.*, vol. 1, no. 5, pp. 998-1005, October 2007.

[21] Y.M.M. Antar, D. Cheng, G. Seguin, B. Henry, and M.G. Keller, "Modified waveguide model for rectangular dielectric resonator antenna," *Microwave and Optical Technology Letters*, vol. 19, no. 2, pp. 158-160, October 1998.

[22] K. A. Walters, and G. W. Hanson, "Resonant frequency calculation for inhomogeneous dielectric resonators using volume integral equations and face-centered node points," *Microwave and Optical Technology Letters*, vol. 32, no. 5, pp. 356-59, 2002.

[23] A. Petosa, R. Larose, A. Ittipiboon, and M. Cuhaci, "Microstrip-fed array of multisegment dielectric resonator antennas," *IEE Proc. Microwave Antennas Propagat.*, vol. 144, no. 6, pp. 472-476, December 1997.

[24] C. A. Balanis, *Advanced engineering electromagnetics.* New York, NY: Wiley, 1989.

[25] G. Zou, H. Groenqvist, J. P. Starski, and J. Liu, "Characterization of liquid crystal polymer for high frequency system-in-a-package applications," *IEEE Trans. Advanced Packaging*, vol. 25, no. 4, pp. 503-508, Nov. 2002.

[26] S. Koulouridis, G. Kiziltas, Z. Yijun D. J. Hansford, and J. L. Volakis, "Polymer-ceramic composites for microwave applications: fabrication and performance assessment," *IEEE Trans. Microw. Theory Tech.*, vol. 54, no. 12, pp. 4202-4208, Dec. 2006.

[27] D. A. Wasylyshyn, "Effects of moisture on the dielectric properties of polyoxymethylene (POM)," *IEEE Trans. Dielectrics and Electrical Insulation*, vol. 12, no. 1, pp. 183-193, Feb. 2005.

[28] Q. Rao, T. A. Denidni, A. R. Sebak, and R. H. Johnston, "Compact independent dual-band hybrid resonator antenna with multifunctional beams," *IEEE Antennas and Wireless Propagation Letters*, vol. 5, pp. 239-242, 2006.

[29] Q. Lai, G. Almpanis, C. Fumeaux, H. Benedickter, and R. Vahldieck, "Comparison of the radiation efficiency of the dielectric resonator antenna and microstrip antenna at Ka band," *IEEE Trans. Antennas and Propagation*, vol. 56, no. 11, pp. 3589-3592, Nov. 2008.

[30] M. Saed and R. Yadla, "Microstrip-fed low profile and compact dielectric resonator antennas," *Prog. Electromagn. Res.*, no. 56, pp. 151-162, 2006.

[31] P. V. Bijumon, S. K. Menon, M. N. Suma, M. T. Sebastian, and P. Mohanan, "Broadband cylindrical dielectric resonator antenna excited by modified microstrip line," *IET (IEE) Electronics Letters*, vol. 41, no. 7, pp. 385-387, March 2005.

[32] K. M. Luk, M. T. Lee, K. W. Leung, and E. K. N. Yung, "Technique for improving coupling between microstripline and dielectric resonator antenna," *IET (IEE) Electronics Letters*, vol. 35, no. 5, pp. 357-358, March 1999.

Chapter 4

X-ray Lithography Fabrication Process

Two photoresists, SU-8 and polymethylmethacrylate (PMMA), are predominantly used in X-ray lithography. SU-8 is a three-component negative tone resist which was developed by IBM in 1989 for UV lithography applications and found to be a sensitive material in the X-ray regime as well [1]. PMMA is a one-component positive tone resist which shows poor sensitivity requiring high exposure doses to be patterned [2]. But its selectivity (contrast) with specific developers is very high resulting in excellent structure quality.

To produce successful and viable polymer-based antenna structures with different portions of ceramic contents, three different X-ray lithography fabrication methods are proposed using positive (PMMA) and negative tone (SU-8) resists [3]. In the first method the structures are lithographically fabricated avoiding an intermediate molding step. In the second and third methods a very precise plastic mold is first fabricated by X-ray lithography, then polymer-ceramic microcomposite is injected into the mold. The plastic mold can remain in the final structure or be removed at the end of process. Sacrificial layer techniques are used to release the antenna structures from the substrate in order to investigate and analyze the material properties and structural qualities in more detail. However, this is not required once these characteristics are controlled and therefore the structures can be fabricated on the final microwave substrate (e.g. alumina, glass, etc.) along with other circuit components for future applications. It is worth mentioning that this integration is possible since the debinding and sintering steps are removed in the fabrication process and the processing temperature is

maintained under 100°C. The resulting antennas are examined regarding their structural qualities using an environmental scanning electron microscope (ESEM). Optimized fabrication parameters allow the production of high quality antenna structures as thick as 2.3 mm.

4.1 Method 1: Direct Fabrication

The direct fabrication method produces a final antenna structure without an intermediate molding step. The electrical properties of the photoresist material are modified by adding ceramic micropowders and the modified photoresist material is patterned by deep X-ray lithography. A new fabrication procedure including material preparation, casting, soft baking, exposure, and development is evaluated to fabricate antenna structures.

4.1.1 Material Preparation

In this procedure a commercial type of SU-8, SU-8(10) from MicroChem™ [4], is chosen as the photoresist binder due to its low viscosity, outstanding crosslinking behaviour, and high sensitivity to X-rays. Submicron sized alumina (Al_2O_3) powder with mean particle diameter of 0.8 microns (Alcoa CT3000SG; Reyholds RC-HP w/o Mg, 0.4 micron) is used as the ceramic filler. A laboratory dissolver stirrer (IKA T110 Ultra Tourax) is used to mix the resist and ceramic micropowder.

SU-8(10) is a low viscosity material and by adding small portions (less than 25 wt%) of alumina micro particles, the viscosity still remains tolerable for the mixing process. However, adding more alumina fillers dramatically changes the viscosity and therefore caution should be exercised. For instance, micro powders should be gradually added until the final portion is reached. This action not only simplifies the process but also helps to avoid deterioration of the mixer device. Furthermore, during the mixing process the temperature increases resulting in lower viscosity and therefore making mixing much easier especially for higher

alumina content. After 30-60 minutes, depending on the amount of micropowder filler, a homogenous composite is produced. Details regarding the resulting viscosity and other issues related to mixing of polymer-alumina composites can be found in [5].

4.1.2 Casting

It is difficult to create homogeneous thick layers of high viscosity material by spincoating; therefore, a different coating technique is pursued. A two-segment metallic box covered with a 125 micron polyimide foil at the bottom side is used for the casting procedure. A picture of the box is shown in Fig. 4.1(a). Segments are attached together by screws and a specific amount of mixture is poured into the metallic box. Due to its low friction and the minimal adhesion of the mixture, the polyimide foil helps to planarize the layer during the soft baking process. The foil can also be released after exposure to ease and accelerate the development process on the back side. Moreover, no further steps are required to release the final structure since it is released from the metallic box at the end of development.

4.1.3 Soft Baking

After the metallic box is filled by the modified photoresist, it is soft baked using a conventional oven to evaporate the excess solvent. SU-8(10) has 40.9% solvent content and the optimal amount of remaining solvent for the photoresist is approximately 7% [6]. Soft baking of thick layers of photoresist has always been challenging since it is difficult to achieve a low and uniform distribution of solvent content in thick layers. In fact the solvent content at the bottom side is often greater than at the top side after soft baking, which can compromise the quality of the final structure. The high solvent content results in air bubbles while the low solvent content results in cracks in the final structure. Different approaches have been used to attempt to solve this problem [6]. In this work a

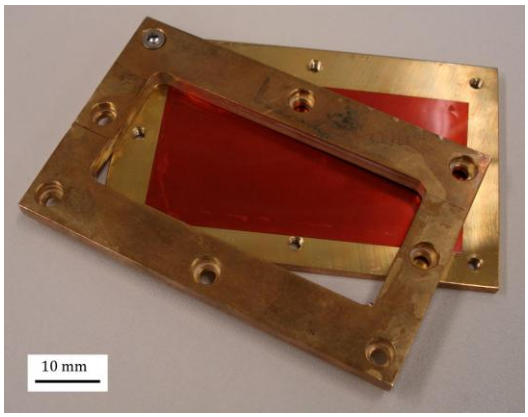

(a)

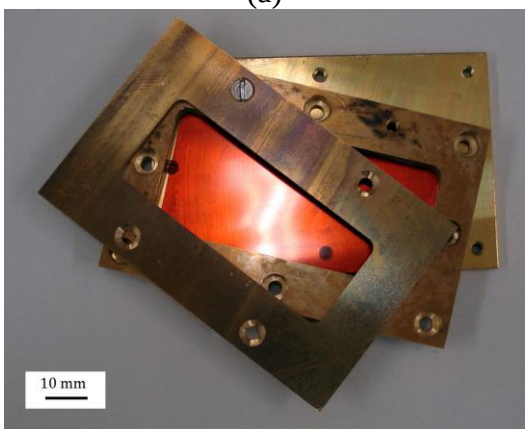

(b)

Fig. 4.1. (a) Two-piece metallic box with polyimide foil at the bottom side fabricated for the casting procedure. (Outer dimensions are 35 mm by 70 mm and inner hole is 30 mm by 65 mm.); (b) Three-piece metallic box with polyimide foil at the bottom side used for preliminary dose screening. (Top layer inner dimensions are 24 mm by 59 mm.)

new uneven two-step soft baking procedure is applied to thick photoresist layers at 95°C.

In the first step, approximately half of the modified photoresist (composite) final thickness is poured and dried until 4% solvent content is achieved for the SU-8 content of the composite. The following formula is used to calculate the final solvent content [3].

$$Solvent\ content\,[\%] = \left(1 - \frac{0.591\left(1 - \frac{M}{100}\right)W_{initial}}{W_{final} - \frac{M}{100}W_{initial}} \right) \times 100 \qquad (4.1)$$

In this equation, M is the weight percent of the ceramic content, $W_{initial}$ is the weight of the composite before soft-bake, and W_{final} is the weight of the composite after soft-bake.

In the next step the second half of the composite is applied on top of the first layer and soft baked to attain 10% solvent content for the SU-8 part of the composite. The previous formula is used to calculate the final solvent content of the second layer and in this computation it is supposed that bottom layer and top layer are isolated from each other. However, in reality these two layers are not perfectly isolated and during the baking process for the second layer, a small portion of the solvent content penetrates from the second layer to the first layer. Therefore, the uneven soft baking procedure will help to achieve a uniform average of 7% solvent content in the composite layer.

4.1.4 Exposure

The X-ray exposures are carried out at beamline Litho-2, a bending magnet beamline at the 2.5-GeV Angstroemquelle Karlsruhe (ANKA) storage ring at Forschungszentrum, Karlsruhe, Germany. The bending radius is set to 5.556m which corresponds to a magnetic field of 1.5T for the electron energy of 2.5GeV. The Litho2 beamline is equipped with a Ni coated Si mirror set to 4.85 mrad which corresponds to an energy range of 2.5-12.4 KeV. The beamline has two Be-windows to separate the UHV part (100µm thick Be-window) from the HV part and the HV part (125µm thick Be-window) to the entrance port of the scanner (JenOptik DexKfK X-ray scanner) located 14.73m from the source point (mask plane).

To find suitable exposure conditions two types of experiments are performed. In the first set of experiments no mask is used and the photoresist material is exposed to synchrotron radiation through a rectangular metallic frame with 59 mm by 24 mm dimensions (Fig. 4.1(b)). The results verify the possibility of

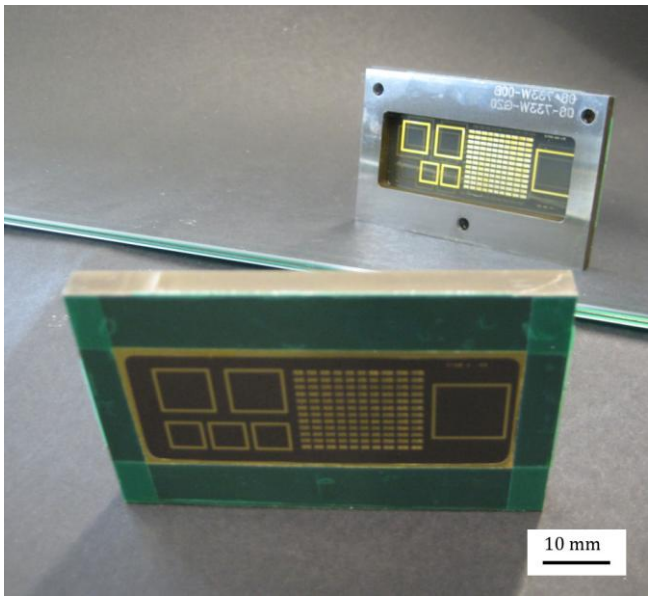

Fig. 4.2. Double sided titanium X-ray mask in front of a mirror. 20 μm and 15 μm gold absorbers are electrodeposited on the back side (front image) and front side (rear image) of the mask respectively. The bottom left rectangular frame is kept single sided for structural quality comparison.

patterning 2 mm thick SU8/alumina layers by X-ray lithography and define the exposure dose range. In the second set of experiments a double sided X-ray mask consisting of a pattern of 20/15 microns gold absorber features supported by a 2.7 micron titanium membrane is used, and finer adjustments are performed. A picture of the mask is shown in Fig. 4.2. This is a mask which was used in [7] to produce tall microwave cavity structures and was modified in [8] to achieve higher X-ray contrast. In all the exposures, a 125 micron thick polyimide filter and 35 micron thick aluminium filter are used between mask and photoresist layer to limit fluorescence radiation of the titanium membrane and different carbon filters are used before the mask to harden the X-ray radiation.

4.1.5 Development and Post Processing

After exposure, propylene glycol monoether acetate (PGMEA) is used at room temperature to dissolve the unexposed area, leaving the patterned photoresist. Development time depends on the samples and is from 30 minutes to a few hours. Following development, the samples are rinsed with isopropanol and dried with a

gentle stream of air. A post-baking procedure can be performed at the end with a very slow temperature ramp to further harden the structures.

4.1.6 Results

Based on the procedure described in the previous subsection, 2.0-2.3 mm thick SU-8 photoresist layers with 0 wt%, 23 wt%, 38 wt%, and 48 wt% alumina content were prepared. In order to pattern the composite material and find an appropriate bottom energy density, special consideration of X-ray absorption is required for the exposing step. This widely depends on the ceramic powder quantity and the size of ceramic particles. Exposure parameters were calculated to maintain a top to bottom energy density ratio of around 3-4 for all experiments. In each case several exposures were performed to find a suitable bottom energy density. For the pure SU-8 (0 wt% alumina filler), the bottom energy density was maintained in the range from 10-20 J/cm^3. This value must be increased considerably for ceramic content photoresists since the absorption of the X-rays is much higher than in pure SU-8.

In the first set of experiments performed without an X-ray mask, it was found that a bottom energy density of less than 100 J/cm^3 was not sufficient even for the 23 wt% sample. With this condition, the bottom side of the photoresist is partially developed resulting in poor structure quality. A picture of a SU-8/alumina structure with insufficient bottom energy density is shown in Fig. 4.3(a). On the other hand, bottom energy density higher than 500 J/cm^3 resulted in poor sidewalls quality.

The second set of experiments was performed with a mask to adjust the required energy density more precisely. The results are shown in Table 4.1. In these experiments the best results were achieved when the bottom energy density were 150, 200, and 250 J/cm^3 for 23, 38, and 48 wt% samples respectively to achieve the required bottom dose for SU-8 to be cross linked. As shown, several carbon filters were used to limit the top to bottom energy density ratio to the

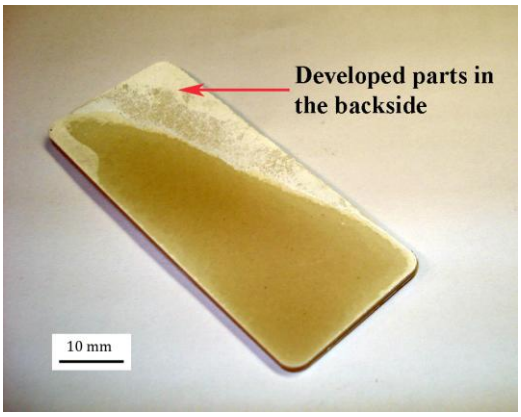

(a)

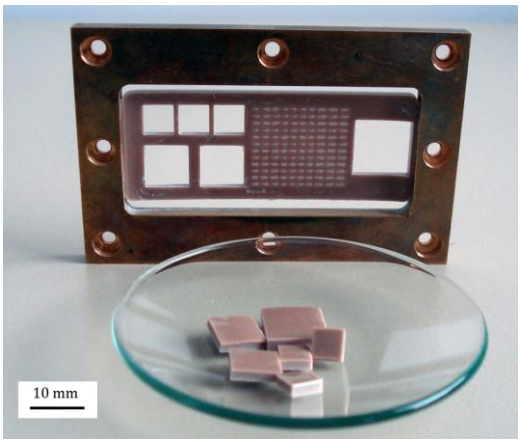

(b)

Fig. 4.3. SU-8/alumina structures after exposure. (a) Partially developed bottom side due to insufficient bottom dose; (b) Fully cross linked structures with 48 wt% alumina released from the frame after 2 hours development with PGMEA.

desired value. The exposure times for the thick samples remained relatively short (i.e. less than 30 minutes) even for higher wt% SU-8/alumina resists. Fig. 4.3(b) shows the final released structures with 48 wt% following development.

4.2 Method 2: Sacrificial Plastic Mold

One of the usual methods to fabricate ceramic structures is micro powder injection molding [9]. In this method demolding is required to release the structure from the metallic permanent mold which complicates the fabrication process especially for millimetre and micrometer scale structures. A sacrificial plastic mold method is proposed in this section to facilitate the fabrication process by using a different demolding step. The fabrication process includes 3 main steps

Table 4.1 Exposure parameters for SU-8 resists with different wt% alumina micropowder content.

Resist Type	Resist Thickness (μm)	Bottom Energy Density (J/cm^3)	Top Energy Density (J/cm^3)	Filters	Exposure Time (min)
0 wt%	2300	10	37	385 μm Carbon 189 μm Carbon 40 μm Carbon	1
23 wt%	2300	150	550	385 μm Carbon 189 μm Carbon 40 μm Carbon	10
38 wt%	2100	200	710	385 μm Carbon 189 μm Carbon 96 μm Carbon	18
48 wt%	2000	250	780	385 μm Carbon 189 μm Carbon 96 μm Carbon	27

and is demonstrated in Fig. 4.4. In this method a sacrificial PMMA mold (frame) is first fabricated by deep X-ray lithography (Fig. 4.4(a)-(d)). A composite of a polymer (or a negative tone photoresist) and high ceramic micropowder content is then injected into the mold (Fig. 4.4(e)). At the end of process, the PMMA frame is removed to achieve the final structure (Fig. 4.4(f)-(h)).

The first step begins with sputtering of 100 nm carbon on a sacrificial silicon wafer. Due to the low adhesion of carbon to silicon, the final structure can be released from the wafer by gently bending the silicon wafer. A PMMA sheet with the desired thickness is glued on the carbon layer. The PMMA layer is exposed through a mask at the Litho-2 beamline at ANKA. The bottom exposure dose is 4000 J/cm^3 while the top to bottom dose ratio of 4 is maintained in the process. The PMMA structure is developed in GG-developer at room temperature to obtain a rectangular frame with submicron range precision. A picture of the frame with 500 micron thick PMMA walls and 1 mm height is shown in Fig. 4.5(a). The

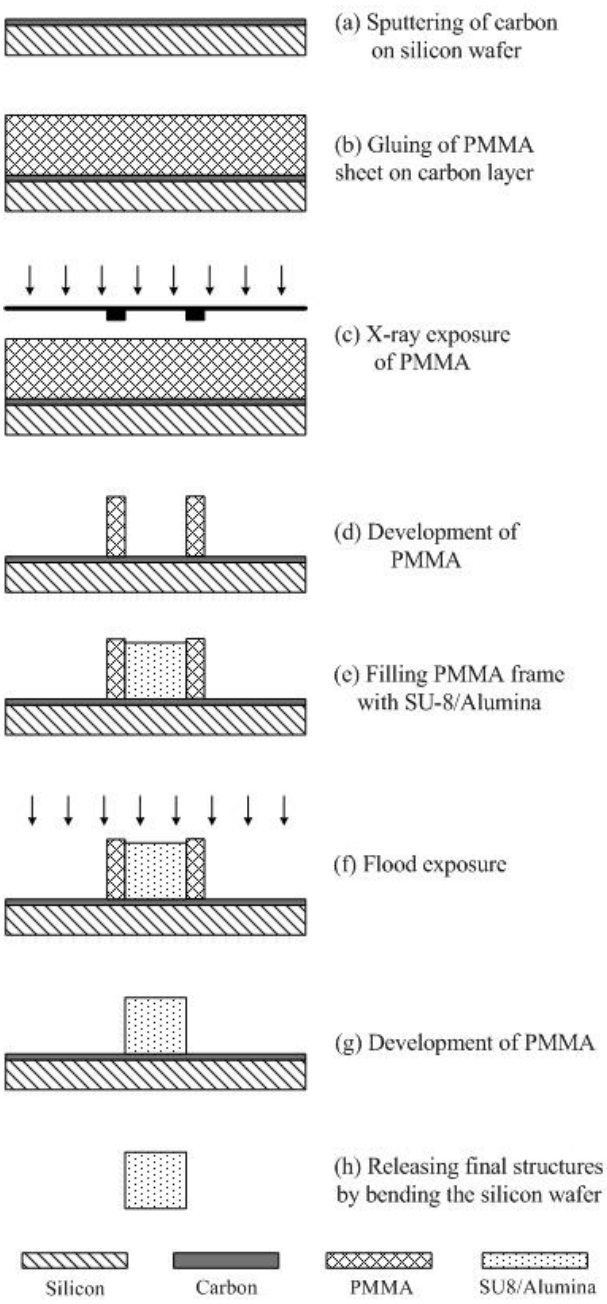

Fig. 4.4. Sacrificial plastic mold fabrication process.

same procedure has successfully produced 1.5 mm and 1.8 mm thick PMMA frames. The mask used in this step is the same as in the previous section. However, with the opposite tone resist, the inverse structures are created for the PMMA frames.

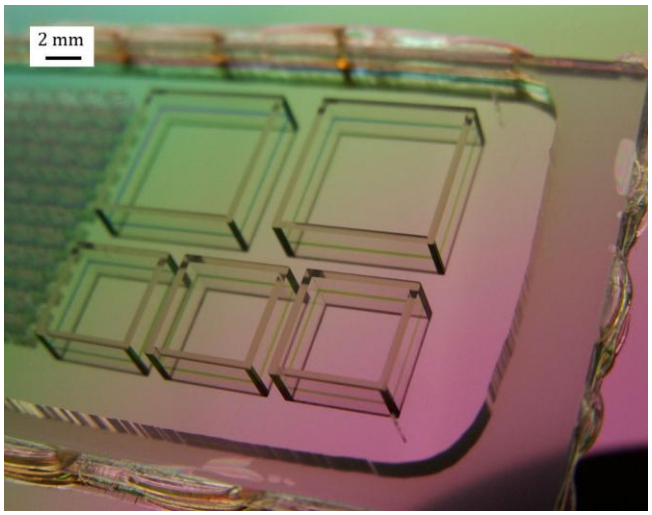

(a)

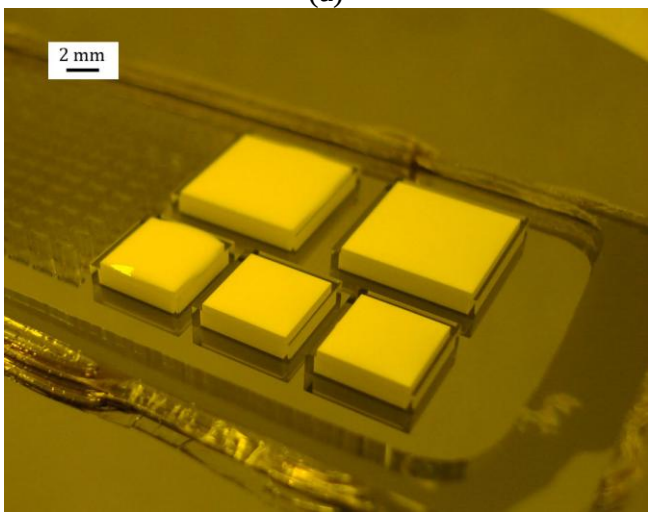

(b)

(c)

Fig. 4.5. (a) PMMA frames on silicon substrate; (b) Frames filled with a composite of SU-8 (10) and 60 wt% alumina micro powder; (c) Final SU-8/alumina structures.

In the second step of this method a composite of SU-8 and alumina micro powder is injected into the PMMA frame. Preparation of the composite follows the same procedure used for Method 1 although a larger portion of alumina micro powder (around 60 wt%) is considered here. Fig. 4.5(b) shows PMMA mold structures filled with the composite material. During the soft baking step which has been done in a conventional oven at 95° C, about 20% shrinkage results. This can be largely compensated by the second injection.

To make a rigid structure and remove the PMMA mold, the wafer is flood exposed to X-ray radiation. In fact, SU-8 molecules are cross linked whilst the long molecular chains of PMMA are broken down making them soluble to developer. Therefore, after X-ray flood exposure the PMMA frame can be removed by either GG developer or acetone to accelerate the fabrication process. It should be noted that the cross linked SU-8/alumina is very hard and essentially insoluble. The final structure released from the sacrificial carbon layer and depicted in Fig. 4.5(c) presents, in general, high structural qualities especially for the sidewalls. More discussions and pictures are provided in Section 4.4.

4.3 Method 3: Permanent Plastic Mold

Electromagnetic simulations using Ansoft HFSS^{TM} indicate that if a thin layer of polymer remains in the surrounding area of the final antenna structure, the impedance bandwidth, radiation patterns, and efficiency of the antenna are not drastically affected and negligible variations in output antenna parameters can be taken into account in the design procedure [10]. Effects of the permanent plastic frame are discussed in detail in Chapter 6. This idea facilitates the fabrication process even further by avoiding the demolding step all together using a permanent plastic mold. The mold insert which should be a high aspect ratio structure is responsible for the precision of the antenna structure features and can be easily batch fabricated by the LIGA process. Fig. 4.6 shows a summary of the fabrication procedure along with an ESEM picture of the outer wall of the PMMA

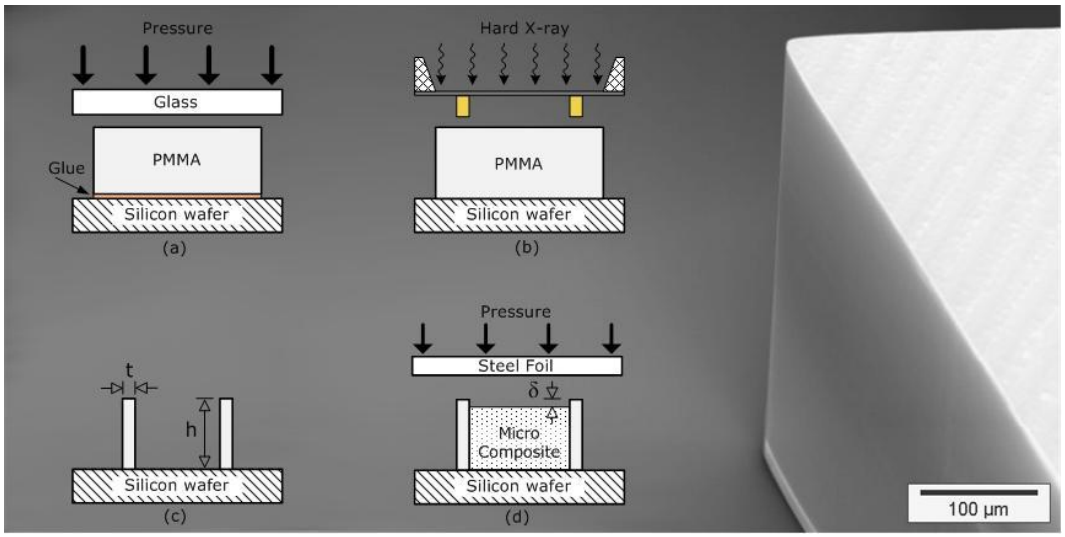

Fig. 4.6. Fabrication process for 1800 µm-thick PMMA frames (background is an ESEM picture of outer wall of the structure). (a) PMMA sheet is chemically attached to the silicon wafer using a very thin layer (10 µm) of PMMA, MMA (Methylmethacrylate, PMMA monomer), BPO (benzoyl peroxide), DMA (dimethylaniline), and MEMO (methacryloxypropyl trimethoxy silane) as the coupling agent. The layer is polymerized at room temperature under 6 bar pressures for 4 hours; (b) Deep X-ray exposure of PMMA using a titanium mask with 15 µm gold absorbers; (c) Development of PMMA using GG developer at room temperature; (d) Mixture of MMA, PMMA, BPO, and DMA with different portions of alumina content is injected into the PMMA frame using JR 2200-JANOME robotic machine. Final polymerization is performed at 110°C in a vacuum oven. Five percent shrinkage (δ) typically results after polymerization.

frame. One of the advantages of the indirect fabrication methods is that the frame can be filled with non X-ray sensitive polymer composites as well. This provides more flexibility for different microwave applications. In this experiment, 46 wt% MMA, 8 wt% PMMA, and 46 wt% alumina micro powder are mixed together and injected into the mold using a robotic machine (JR 2200-JANOME (GLT)). The composite material is polymerized inside the mold at room temperature using chemical agents (BPO, MEMO, and DMA). A 50 micron stainless steel foil is put on top of the material and gradual pressure is applied. The foil prevents the evaporation of MMA and pressure is required to maintain the smooth surface during polymerization. Around 5% linear shrinkage results in the final structure due to MMA polymerization. A fabricated sample based on this idea is shown in

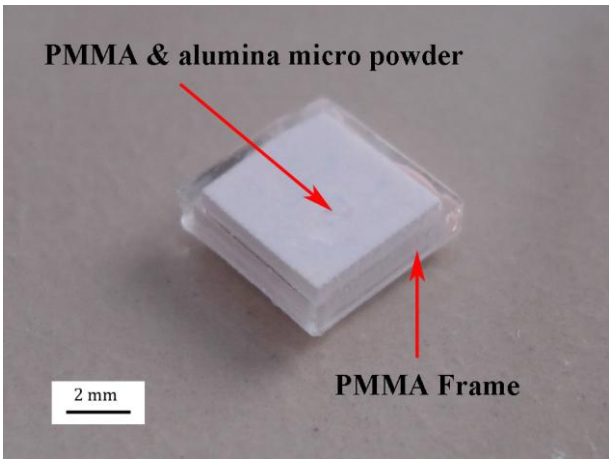

Fig. 4.7. A sample fabricated by permanent plastic mold method.

Fig. 4.7. The mold is a 500 micron thick 1.8 mm high rectangular PMMA frame which is fabricated by X-ray lithography using a similar procedure and the same mask described in Section 4.2. However, when a mask is designed for this purpose it is recommended to keep the frame thickness less than 500 microns for antenna structures working at millimetre-wave frequencies.

4.4 Results and Discussions on Structure Quality

Rectangular frames and boxes with different thicknesses obtained by using the X-ray mask, shown in Fig. 4.2, are examined using ESEM micrographs in this section. In the third fabrication method, the PMMA rectangular frame is directly responsible for the precision of the antenna structure since it remains as part of the final structure. In the second method, although the PMMA frame is removed at the end of fabrication process, its structural quality is transferred into the final antenna structure. Hence analysis of the frame structure regarding the critical dimensions (i.e. maximum achievable thickness and aspect ratio) and their accuracy is very important for these two methods. Fig. 4.8(a) and (b) show details of the sidewall and edge of an uncoated PMMA frame with 1830 μm height, on a silicon substrate. Excellent sidewall verticality better than 89.7° is obtained while the sidewall roughness is expected to be in the order of 26 ± 12 nm [7]. To have a better idea of the capability of X-ray lithography to fabricate high aspect ratio

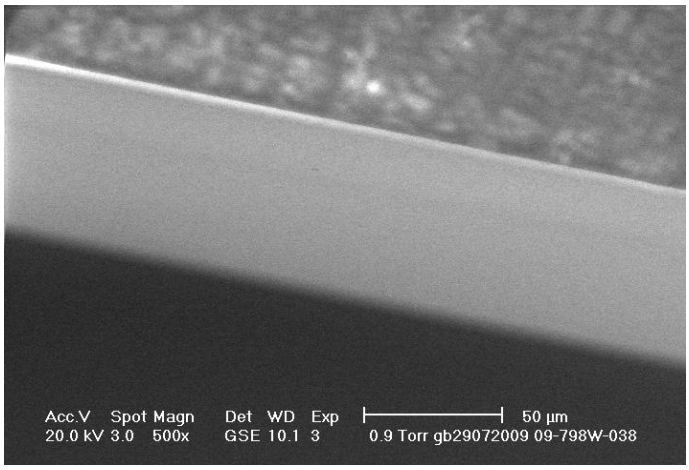
Acc.V Spot Magn Det WD Exp 50 µm
20.0 kV 3.0 500x GSE 10.1 3 0.9 Torr gb29072009 09-798W-038

(a)

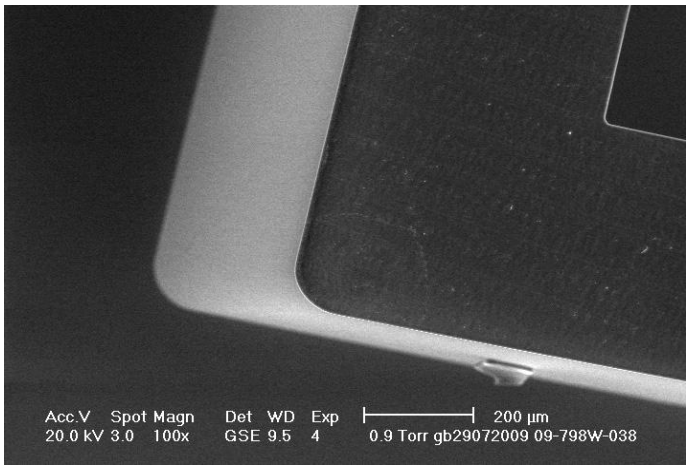
Acc.V Spot Magn Det WD Exp 200 µm
20.0 kV 3.0 100x GSE 9.5 4 0.9 Torr gb29072009 09-798W-038

(b)

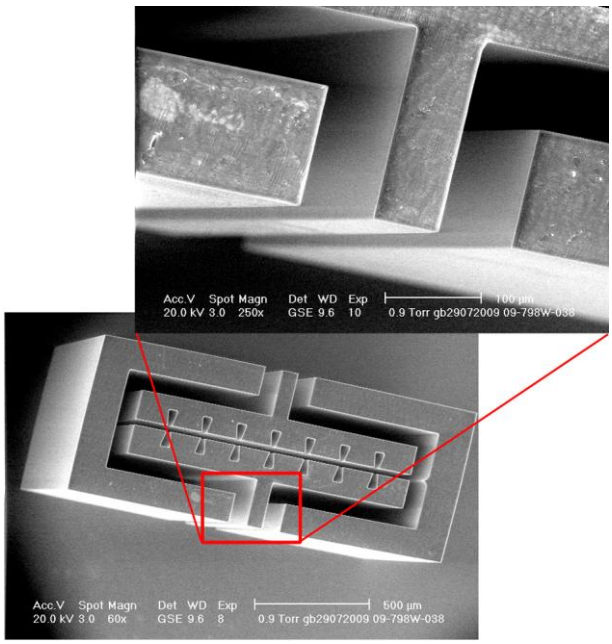
Acc.V Spot Magn Det WD Exp 100 µm
20.0 kV 3.0 250x GSE 9.6 10 0.9 Torr gb29072009 09-798W-038
Acc.V Spot Magn Det WD Exp 500 µm
20.0 kV 3.0 60x GSE 9.6 8 0.9 Torr gb29072009 09-798W-038

(c)

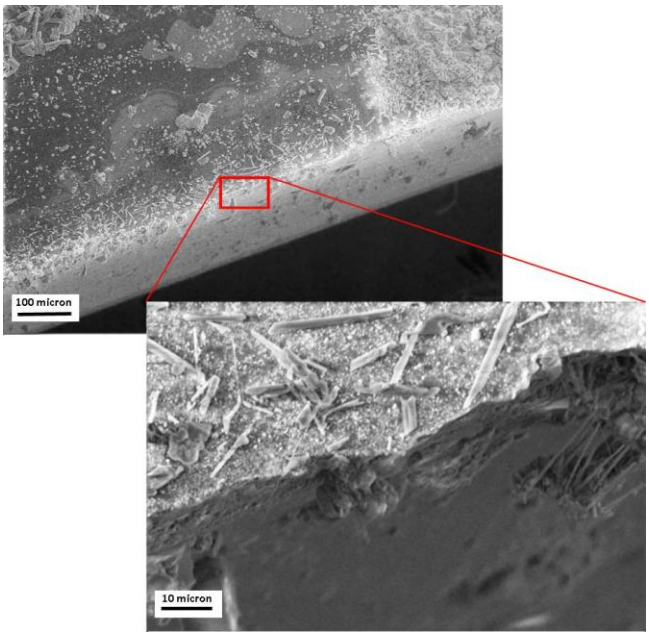

(d)

Fig. 4.8. ESEM micrographs. (a) Details of the sidewall of a PMMA rectangular frame with 1830μm height on a silicon substrate; (b) Edge of a PMMA rectangular frame with 1830μm height on a silicon substrate; (c) A structure with the aspect ratio of 36:1 fabricated with the same mask to show the capability of X-ray lithography in producing high aspect ratio frames for antenna applications; (d) Details of the sidewall of a 60 wt% uncoated alumina sample after the PMMA mold is removed.

frames with high precision, one of the tiny structures in the middle of the mask is also investigated. As shown in Fig. 4.8(c), very accurate structures are fabricated with 50 μm width and 1830 μm height, resulting in an aspect ratio of 36:1. This structure is similar to the RF MEMS capacitors in [11], and further reinforces the idea of making complicated antenna and other structures with fine features using Methods 2 and 3.

An alternative for Method 3 is making an SU-8 frame instead of a PMMA frame. There are several reasons for and against this idea. For instance, UV lithography could also be used to make SU-8 frames on the order of 1-2 mm with possibly reduced quality and larger local feature [12]. Thicker SU-8 structures can be fabricated using X-ray lithography due to its higher sensitivity. The SU-8

structures are more durable and stronger than PMMA structures. However, less accurate structures may be fabricated by SU-8 due to its lower X-ray contrast.

Fig. 4.8(d) shows the sidewall and top edge of a 60 wt% alumina-filled uncoated sample after the PMMA mold is removed. An excellent sidewall verticality and roughness is transferred into the sample by the PMMA frame. Although many interior particles can be seen in the picture, no particles in the range of a few microns can be detected in the sidewall. The wavy edge of the sample is due to a slight overfilling of the mold.

To investigate the structural quality of the samples fabricated by direct X-ray lithography (Method 1), ESEM micrographs of the edge and sidewall of the pure SU-8, 38 wt%, and 48 wt% alumina-filled structures are shown in Fig. 4.9(a), (b), and (c), respectively. Although a good sidewall quality is achieved for pure SU-8 and only a small number of particles in the range of few microns are detected in the sidewall of the 38 wt% sample, the visible roughness of 48 wt% sample is apparent in the picture. Roughness in the sidewall of the ceramic content structures has two main causes. First, agglomeration of the submicron sized alumina powders in the mixing process makes larger particles and radiation scattering from these particles and also smaller particles during exposure degrades the quality of the structure. Second, during the development process SU-8 is dissolved in the border of the exposed area but these particles remain.

Moreover, an excess layer of a few microns is found on the top part of the sidewall of the 48 wt% sample which has limited the quality of the structure. This T-topping effect is likely due to fluorescence radiation produced by the titanium membrane. The filter which was used to limit the florescence radiation was likely insufficient in this case due to increased exposure dose. To solve the problem and achieve better structural quality in high wt% samples if necessary, the utility of other membranes, such as beryllium, could be explored.

In another experiment to compare the effect of the gold absorber thicknesses on the mask, it was found that with 20 microns gold absorber on the mask a very

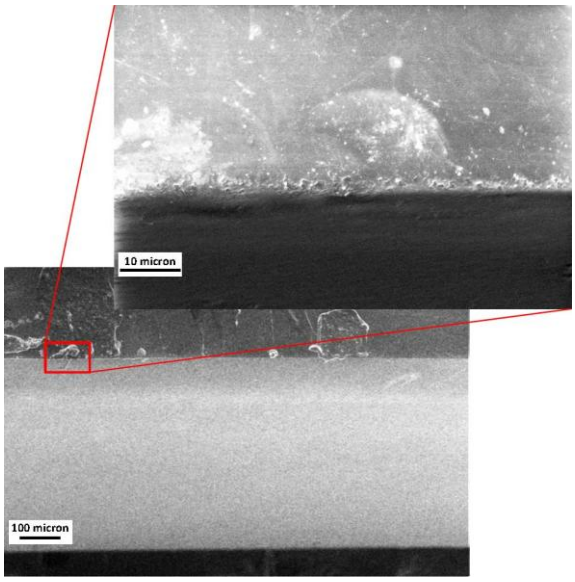

(a)

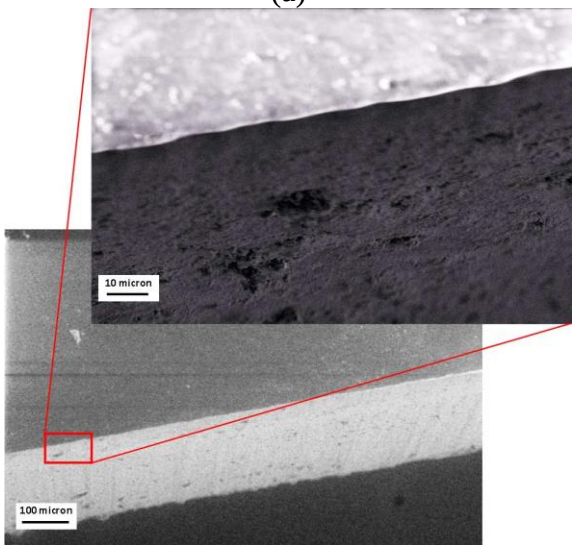

(b)

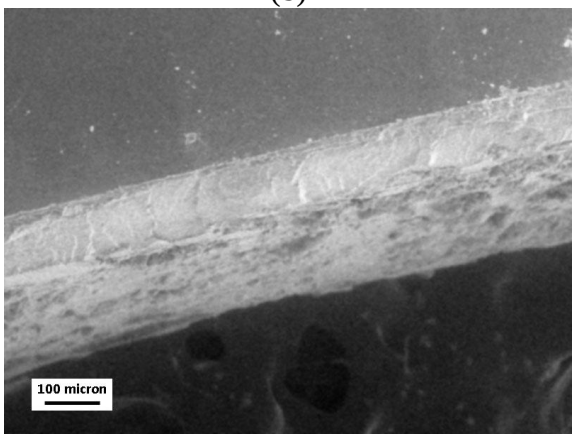

(c)

Fig. 4.9. ESEM micrographs of the top edge and sidewall of structures fabricated by direct X-ray lithography. (a) 2.3 mm thick pure SU-8; (b) 2.1 mm thick 38 wt% alumina; (c) 2 mm thick 48 wt% alumina.

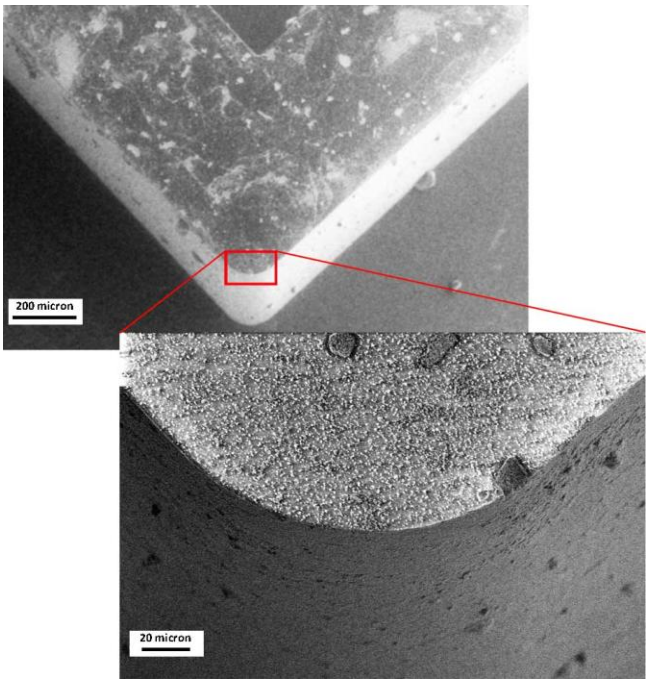

Fig. 4.10. ESEM micrographs of PMMA structure with 20 wt% alumina content.

thin layer in the unexposed area on the resist begins to cross link due to insufficient X-ray contrast and the high exposure dose required for ceramic content structures. As a result, development time is unreasonably increased to more than 24 hours at this condition. However, with 35 microns gold absorber, a maximum of 2 hours development time was achieved.

In direct X-ray lithography fabrication, PMMA can be used instead of SU-8 as a photoresist binder. A sample with about 20 wt% alumina content and 1 mm height is fabricated and its ESEM micrograph is shown in Fig. 4.10. Here, 20 wt% alumina micropowder, 68 wt% MMA, and 12 wt% PMMA are mixed in the vacuum condition and polymerized using some initializations under 6 bar pressure at room temperature to make a 1 mm thick layer. Further polymerization is performed in the oven at 110°C with a very slow ramp. The layer is then glued on the silicon substrate and exposed through the same mask with a bottom dose of 7000 J/cm^3 while the top to bottom dose ratio is kept around 4 in the process. The wafer is developed in GG-developer at room temperature. As shown, the quality of the structure is again limited by agglomeration of the submicron sized alumina

powders in the sidewall. Particles in the range of a few microns are quite obvious on the sidewall of the structure. In comparison to SU-8/ceramic structuring, although PMMA/ceramic patterning can lead to a better verticality, much longer exposure time (e.g. more than 7 hours in this case) is required and the mixing process is more difficult due to higher viscosity.

All in all, more ceramic content can be used in Method 2 and 3 since the sidewall quality is protected by a polymer frame. However, it should be noted that the stability of the structure depends on the ceramic filler. In fact, the larger the ceramic content, the less structural stability. It is recommended to keep the ceramic filler less than 70 wt% to achieve good structural stability. Furthermore, agglomeration of the ceramic micro sized particles which was increased by increasing the ceramic filler content is the main restriction in the quality of structures in the direct fabrication method. To achieve higher quality structures, optimizing the ceramic particle size and the mixing process would be necessary.

4.5 Summary

Three lithographic fabrication methods were examined to realize high precision photoresist-based polymer resonator antennas in the millimetre or micrometer range. In all proposed fabrication methods, the debinding and sintering steps were removed to maintain the high dimensional quality of the antenna structures and simplify the fabrication procedure. Further simplification was also performed by eliminating the demolding step and consequently keeping the plastic mold in the final structure. Plastic molds in Method II and III can be batch fabricated by the LIGA process in various shapes, and sizes, and with good precision.

References

[1] R. Angelo, J. Gelorme, J. Kuczynski, W. Lawrence, S. Pappas, and L. Simpson, U.S. Patent 5, 102,772, IBM, 1992.

[2] E. Spiller, “Early history of x-ray lithography at IBM,” *IBM Journal of Research and Development*, vol. 37, no. 3, pp. 291-297, May 1993.

[3] A. Rashidian, D. M. Klymyshyn, M. Boerner, and J. Mohr, “Deep x-ray lithography processing for batch fabrication of thick polymer-based antenna structures,” *Journal of Micromech. Microeng.*, 11 pp., vol. 20, no. 2, Feb. 2010.

[4] MicroChem Corporation, USA webpage http://www.microchem.com.

[5] T. Hanemann, “Influence of particle properties on the viscosity of polymer-alumina composites,” *Ceramics International*, no. 34, pp. 2099-2105, 2008.

[6] C. Becnel, Y. Desta, and K. Kelly, “Ultra-deep x-ray lithography of densely packed SU-8 features: I. an SU-8 casting procedure to obtain uniform solvent content with accompanying experimental results,” *Journal of Micromechanics and Microengineering*, no. 15, pp. 1242-1248, 2005.

[7] Z. Ma, LIGA cavity resonators and filters for microwave and millimeter-wave applications, Ph.D. thesis, University of Saskatchewan, 2007.

[8] M. Boerner, F. Gosch, B. Matthis, J. Mohr, E. Reznikova, “Double sided X-ray transparent membranes for different HARMST applications,” *8th Intern. Workshop on High-Aspect-Ratio Microstructure Technology*, pp. 15-16, Saskatoon, Canada, June 2009.

[9] R. Zauner, “Micro powder injection molding,” *Microelectronic Engineering*, no. 83, pp. 1442-44, 2006.

[10] Ansoft HFSS Version 10.0, Ansoft Corporation, 225 West Station Square Drive, Suite 200, Pittsburgh, PA 15219.

[11] D. M. Klymyshyn, D. Haluzan, M. Boerner, S. Achenbach, J. Mohr, and T. Mappes, "High aspect ratio vertical cantilever RF-MEMS variable capacitor," *IEEE Microw. Wireless Compon. Lett.*, vol. 17, no. 2, pp. 127-9, 2007.

[12] M. Despont, H. Lorenz, N. Fahrni, J. Brugger, P. Renaud, and P. Vettiger, “High aspect ratio, ultra thick, negative-tone near-UV photoresist for MEMS applications,” *IEEE International workshop on Micro Electro Mechanical Systems*, pp. 518-522, 1997.

Chapter 5

Electrical Properties Measurement

Proposed by Troughton to measure dispersion of microstrip transmission lines [1], microstrip ring resonators have attracted considerable interest for electrical properties measurements of dielectrics even at very high frequencies [2]. The advantage of this technique, which uses the resonance frequency and the Q factor of the resonator to calculate the permittivity and the loss tangent of the substrate, is its simplicity and accuracy due to the absence of end-effects and high Q factor. However, this technique requires dielectric samples in the form of metal-cladded substrates, with the microstrip ring pattern etched or machined on the metal layer. Due to the low adhesion of metal to X-ray resists and also the requirement to pattern rings separately on every sample, fabricating uniformly patterned metal-cladded substrates for a series of samples is a difficult and tedious task in a laboratory. To overcome this limitation and utilize a simple method, a combination of a one-layer and two-layer microstrip ring resonator measurement is proposed [3]. Microstrip ring resonators with different characteristics are designed and fabricated on microwave substrates with known electrical properties. SU-8 and PMMA microcomposite slabs are prepared and superimposed on the microstrip ring resonators to construct a two-layer microstrip structure. The differences in Q factor and resonant frequency before and after slab insertion are used to determine the dielectric constant and loss tangent of the microcomposite slabs from 2 to 40 GHz. The two-layer microstrip ring resonator measurement technique is validated using two standard methods of cavity resonator and long stripline [4].

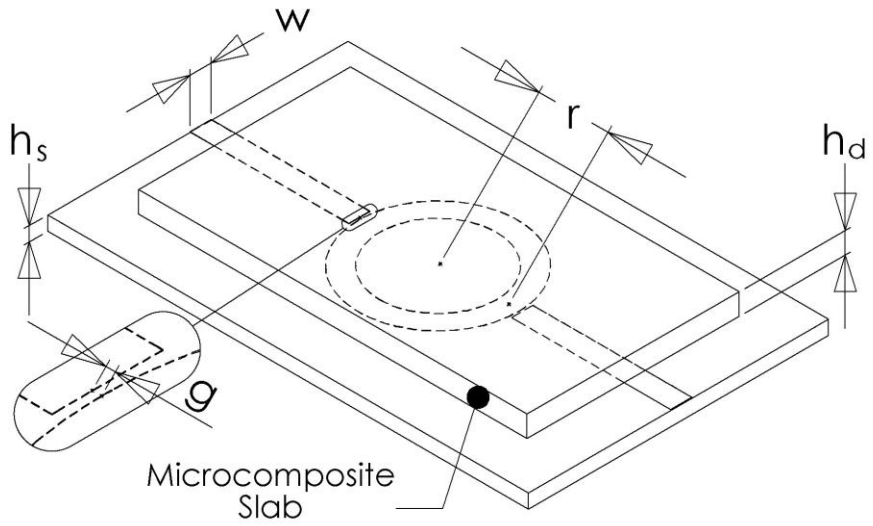

Fig. 5.1. Two-port microstrip ring resonator structure with a superimposed microcomposite slab.

5.1 Theory of Measurement Technique

5.1.1 Relative Permittivity

Fig. 5.1 illustrates the two-port microstrip ring resonator configuration. The ring resonator with mean radius of r and width of w is printed on a microwave substrate with thickness of h_s. The microcomposite slab with thickness of h_d is superimposed on the ring resonator. The circuit has multiple resonances which occur when the perimeter of the ring is equal to an integer number of the guided wavelength

$$2\pi r = n\lambda_{g,2} = \frac{nc}{f_{r,2}\sqrt{\varepsilon_{eff,2}}} \tag{5.1}$$

where $\lambda_{g,2}$, $f_{r,2}$, and $\varepsilon_{eff,2}$ are the guided wavelength, resonance frequency, and effective permittivity of the two-layer microstrip ring resonator, respectively; n is the number of wavelengths on the ring and c is the free space velocity of light. The resonance frequency, $f_{r,2}$, of the two-layer resonator is related to the one-layer (i.e. without the slab) resonance, $f_{r,1}$, as follows

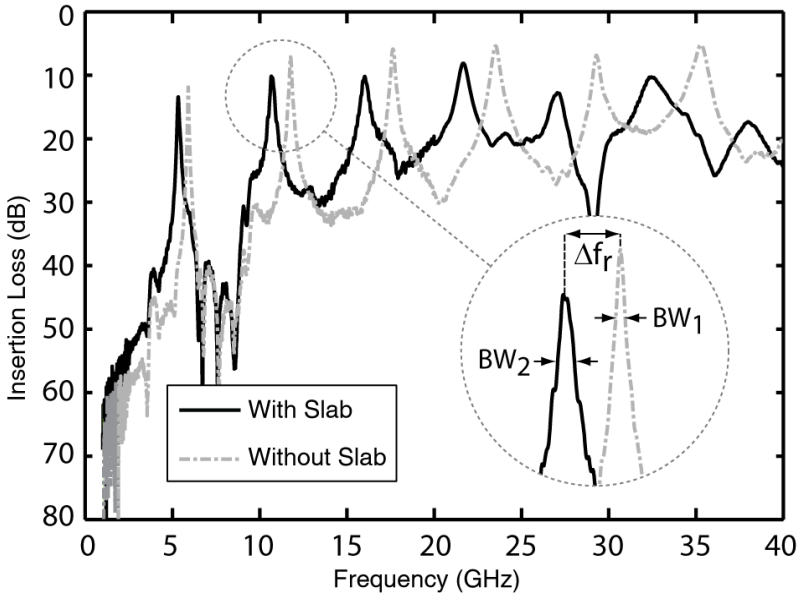

Fig. 5.2. Insertion loss measurement for the 6 GHz ring resonator (r = 5.84 mm, h_s = 0.254 mm, w = 0.71 mm) on TLY5 substrate (ε_r = 2.2, tanδ = 0.0009) before and after insertion of pure SU-8 slab (h_d = 1.73 mm).

$$\varepsilon_{eff,2} = \left(\frac{f_{r,1}}{f_{r,2}} \right)^2 \varepsilon_{eff,1} \tag{5.2}$$

where $\varepsilon_{eff,1}$ is the effective permittivity of the one-layer microstrip ring resonator; $f_{r,1}$ and $f_{r,2}$ can be extracted from the measured insertion loss of the ring resonator with and without the microcomposite slab, as shown in Fig. 5.2 for a particular case.

The relative permittivity of the slab, $\varepsilon_{r,2}$, can be found analytically using the effective permittivity of the two-layer microstrip configuration ($\varepsilon_{eff,2}$) and the relative permittivity of the substrate ($\varepsilon_{r,1}$) [5]

$$\varepsilon_{r,2} = \frac{q_2}{q_1 + q_2 - 1 + \dfrac{(1-q_1)^2}{\varepsilon_{eff,2} - q_1 \varepsilon_{r,1}}} \tag{5.3}$$

where q_1 and q_2 are Wheeler filling factors for the two-layer geometry, and are functions of geometrical parameters of the microstrip circuit (i.e. w, h_d, and h_s).

5.1.2 Dielectric Loss Tangent

The introduction of the microcomposite slab on the microstrip ring not only affects the resonance frequency of the circuit, but also changes the 3-dB bandwidth of the resonance as seen in Fig. 5.2. It is known that the unloaded quality factor (Q_U) is related to the 3-dB bandwidth (BW) by [6]

$$Q_U = \frac{f_r}{BW} \frac{1}{1 - 10^{-\frac{L}{20}}} \tag{5.4}$$

where f_r is the resonance frequency, and L is the insertion loss level in dB at f_r.

The dielectric quality factor of a multilayer microstrip configuration, $Q_{D,N}$, is related to the loss tangents of different layers [7]

$$\sum_{i=1}^{N} p_{i,N} \tan \delta_i = \frac{1}{Q_{D,N}} \tag{5.5}$$

where N is the total number of layers, $tan\ \delta_i$ is the dielectric loss tangent of layer i, and

$$p_{i,N} = \frac{\varepsilon_{r,i}}{\varepsilon_{eff,N}} \frac{\partial \varepsilon_{eff,N}}{\partial \varepsilon_{r,i}} \tag{5.6}$$

is the Schneider filling factor [7] for ith layer of the N-layer microstrip circuit.

Dielectric loss tangent of the superimposed slab ($tan\ \delta_2$) can be found by subtracting Equation 5.5 for one- and two-layer configurations

$$\tan \delta_2 = \frac{1}{p_{2,2}} \left(\frac{1}{Q_{D,2}} - \frac{1}{Q_{D,1}} \right) + \frac{p_{1,1} - p_{1,2}}{p_{2,2}} \tan \delta_1 \tag{5.7}$$

where

$$p_{1,1} = \frac{\varepsilon_{r,1}(1+G)}{\varepsilon_{r,1}(1+G) + 1 - G} \ , \qquad G = \left(1 + 10 \frac{h_s}{w} \right)^{1/2} \tag{5.8}$$

and $p_{1,2}$ and $p_{2,2}$ can be derived using the effective permittivity expression of a two-layer microstrip line, developed by Svacina [5], and Equation 5.6

$$p_{1,2} = \frac{\varepsilon_{r,1}}{\varepsilon_{eff,2}} q_1 \tag{5.9}$$

$$p_{2,2} = \frac{\varepsilon_{r,2}}{\varepsilon_{eff,2}} \frac{q_2(1-q_1)^2}{\left(\varepsilon_{r,2}(1-q_1-q_2)+q_2\right)^2} \tag{5.10}$$

The only unknowns in Equation 5.7 are $Q_{D,1}$ and $Q_{D,2}$ which are yet to be defined.

The unloaded quality factors of one- and two-layer configurations, $Q_{U,1}$ and $Q_{U,2}$, are computable from the measured insertion loss using Equation 5.4. In addition, it is known that the unloaded quality factor of a microstrip circuit can be expressed as

$$\frac{1}{Q_U} = \frac{1}{Q_C} + \frac{1}{Q_R} + \frac{1}{Q_D} \tag{5.11}$$

where Q_C , Q_R , and Q_D are quality factors related to conductor, radiation and dielectric losses, respectively [8]. If it is assumed that the changes in conductor and radiation losses due to the superposition of the slab are negligible, it can be concluded that

$$\frac{1}{Q_{D,2}} - \frac{1}{Q_{D,1}} = \frac{1}{Q_{U,2}} - \frac{1}{Q_{U,1}} \tag{5.12}$$

The loss tangent of the microcomposite slab can be therefore determined from the measurement of f_r, L, and BW, with and without the slab to calculate Equation 5.12 and substituting this into Equation 5.7.

5.1.3 Frequency Dependencies of Microstrip Resonator

To calculate frequency dependent relative permittivity of the slab, $\varepsilon_{r,2}(f)$, a general method of frequency improvement in the form of [9]

$$\varepsilon_{eff}(f) = \varepsilon_r - \frac{\varepsilon_r - \varepsilon_{eff}(f=0)}{1+P(f)} \tag{5.13}$$

can be used for the effective permittivity of the one-layer microstrip circuit in Equation 5.2. Two accurate formulations for the frequency correction term, $P(f)$, are that of Edwards and Owens [10] and Kirsching and Jansen [11].

To calculate the frequency dependent dielectric loss tangent of the slab, the frequency dependent Schneider filling factors, $p_{i,N}(f)$, should be derived. For the one-layer configuration, substituting Equation 5.13 into 5.6 results in

$$p_{1,1}(f)=\left(\frac{2P(f)+1+G}{2P(f)+2}\right)\left(\frac{\varepsilon_{r,1}}{\varepsilon_{eff,1}(f)}\right) \tag{5.14}$$

For the two-layer structure, an analytical frequency dependent effective permittivity is required to define Schneider filling factors. For this purpose, the effective permittivity formulation of the two-layer structure ($\varepsilon_{eff,2}$) [5] is first used to calculate the quasi TEM expression. This value is then considered as the effective permittivity of a one-layer microstrip structure, and the relative permittivity of the new one-layer configuration, ε'_r , is extracted as a function of $\varepsilon_{r,1}$ and $\varepsilon_{r,2}$

$$\varepsilon'_r=\frac{2}{1+G}\left[\varepsilon_{r,1}q_1+\varepsilon_{r,2}\frac{(1-q_1)^2}{\varepsilon_{r,2}(1-q_1-q_2)+q_2}+\frac{G-1}{2}\right] \tag{5.15}$$

Substituting Equation 5.15 and the quasi TEM effective permittivity of the two-layer structure into Equation 5.13, the frequency dependent effective permittivity of the two layer configuration is derived. After some manipulation

$$\varepsilon_{eff,2}(f)=A\left[\varepsilon_{r,1}q_1+\varepsilon_{r,2}\frac{(1-q_1)^2}{\varepsilon_{r,2}(1-q_1-q_2)+q_2}\right]-B \tag{5.16}$$

where

$$A=\frac{2P(f)+1+G}{(1+P(f))(1+G)}$$

and

$$B=\frac{(1-G)P(f)}{(1+P(f))(1+G)}$$

Equation 5.16 is a relatively simple analytical function in terms of permittivities. An advantage of this equation is that it can be incorporated with ease into Equation 5.6 to derive the Schneider filling factors for high frequencies, due to the

fact that the Edwards and Owens *P(f)* is not a function of dielectric constants and therefore its partial derivatives do not need to be calculated

$$p_{1,2}(f) = Aq_1 \frac{\varepsilon_{r,1}}{\varepsilon_{eff,2}(f)} \tag{5.17}$$

$$p_{2,2}(f) = A\left(\frac{q_2(1-q_1)^2}{\left(\varepsilon_{r,2}(1-q_1-q_2)+q_2\right)^2} \right) \frac{\varepsilon_{r,2}}{\varepsilon_{eff,2}(f)} \tag{5.18}$$

These frequency dependent filling factors are implemented in Equation 5.7 to calculate the loss tangent of the slab.

5.2 Slab Preparation

Two different procedures are followed to produce slabs of SU-8 and PMMA microcomposites. Submicron sized alumina (Al_2O_3) powder with mean particle diameter of 0.8 microns (Alcoa CT3000SG; Reyholds RC-HP w/o Mg, 0.4 micron) is used as the ceramic filler. A laboratory dissolver stirrer (IKA T110 Ultra Tourax) is used to mix the resist and ceramic micropowder in both cases.

5.2.1 SU-8 Microcomposite Slabs

A commercial type of SU-8 with low viscosity, SU-8(10) from MicroChem™ [12], having 40.9% solvent content is mixed with different weight percents of alumina micropowder for about 1 hour to produce homogeneous composites (the mixing time is slightly increased for higher amounts of alumina filler). The low viscosity of SU-8(10) simplifies the mixing procedure. A specific amount of the mixture is put into a metallic frame with 100 μm polyimide foil on the bottom side. After baking at 95°C to reduce the excess amount of solvent content, samples are exposed to X-rays at the ANKA storage ring. Fig. 5.3(a) shows one of the samples after X-ray exposure. The appropriate exposure dose and time varies considerably with the portion of ceramic content. Fig. 5.4 shows these parameters for up to 50 weight percent of alumina content. Determination of exposure dose and time is performed based on DoseSim simulator [13] parameters as a starting

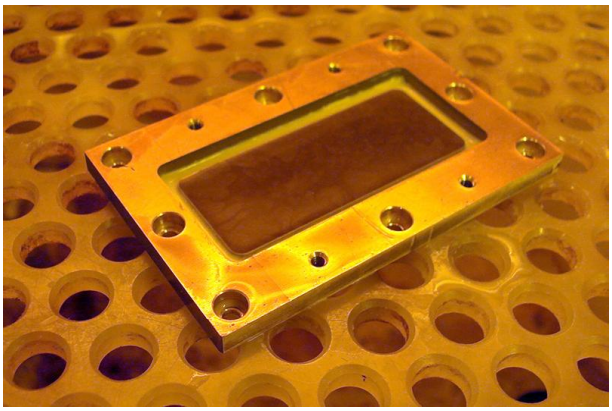

(a)

(b)

Fig. 5.3. Preparation of SU-8 microcomposite slabs. (a) After flood exposure; (b) After development.

point and fine-tuning through trial and error experiments to achieve best possible fully developed structures at the bottom and low sidewall slope. While the exposure dose and time are very low for the pure SU-8 (10 J/cm^3 dose and less than 1 minute time), they increase rapidly for small portions of alumina additive (e.g. they are about 15 and 10 times more than pure SU-8 parameters respectively for 20 wt% alumina). The diagram shows a slower increase for ceramic contents from about 20 to 45 wt%. It is worth mentioning that in all cases the exposure time remains less than 30 minutes. The samples are developed with propylene glycol monoether acetate (PGMEA) at room temperature to produce the final slabs (Fig. 5.3(b)).

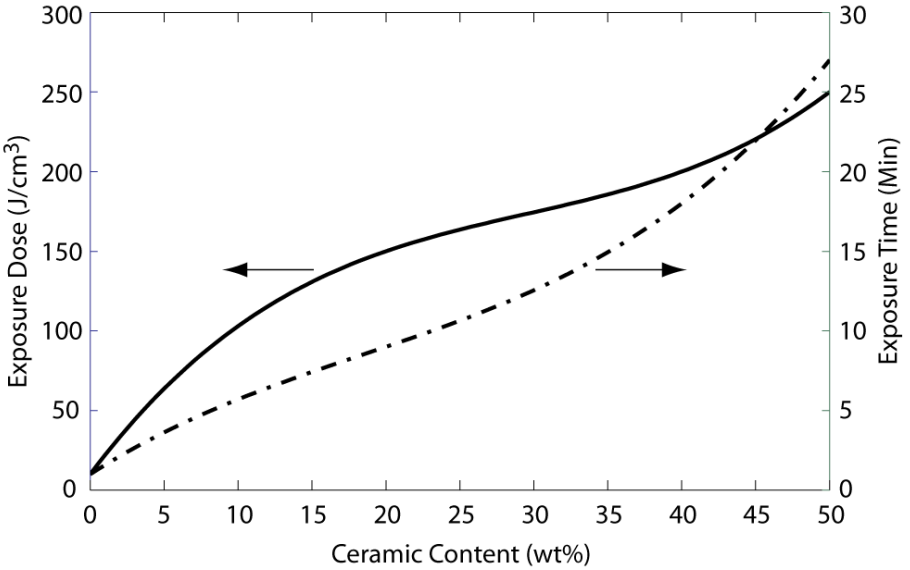

Fig. 5.4. Exposure time (100 mA reference current) and dose for 2 mm SU-8 samples with different alumina content.

5.2.2 PMMA Microcomposite Slabs

A casting procedure is followed to fabricate PMMA/alumina microcomposite slabs. A solution of 80 wt% MMA (Methylmethacrylate, PMMA monomer) and 20 wt% PMMA is mixed with different weight percents of alumina micropowders in a vacuum chamber at room temperature and at 100 mbar vacuum for about 30 minutes. The vacuum prevents creating gas bubbles during the mixing procedure. The resulting material is mixed with dimethylaniline (DMA) as the polymerization starter and benzoyl peroxide (BPO) catalyst as the hardener for 1 minute at the same condition and poured into a temporary frame with 50 micron thick stainless steel foils in the bottom and top sides as depicted in Fig. 5.5. The top side is covered with a glass plate and the whole frame is put under 6 bar pressure for 20 hours. The stainless steel foils and pressure are required to prevent MMA evaporation, to create a smooth surface on the composite material, and to avoid oxygen absorption, which postpones the polymerization process. The stainless steel foil has minimal adhesion to PMMA and aids delamination of the composite material from the frame. Finally, to create a harder material, further

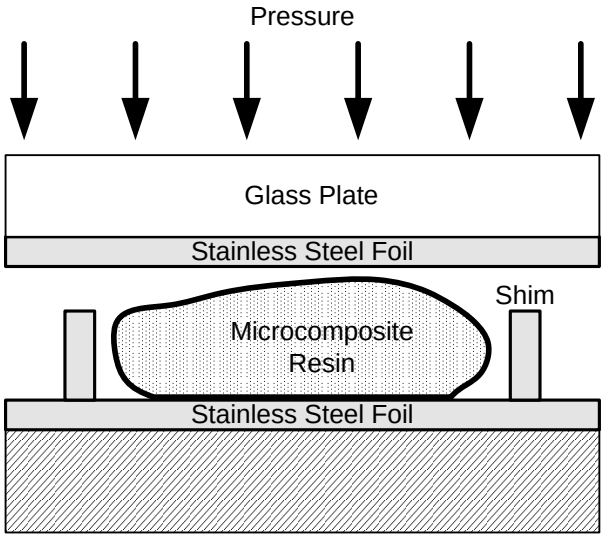

Fig. 5.5. Polymerization of the PMMA microcomposite resist layer using a metallic frame.

polymerization is performed in an oven at 110°C for about 1 hour. A slow heating and cooling ramp is performed to prevent cracks due to the temperature coefficient difference of alumina and PMMA.

5.3 Electrical Properties

The electrical properties of the fabricated pure SU-8 and PMMA samples, as well as samples with different weight percentages of alumina micropowder in the PMMA and SU-8 matrices are measured using the two-layer microstrip ring resonator technique to assess the microwave performance. Since the ring resonator parameters such as substrate thickness and permittivity, line width, ring diameter, and coupling gaps may affect the accuracy of the results [14], microstrip ring resonators of varying diameters were designed and fabricated on different substrates. Table I shows the physical parameters of different rings. In all designs the line width to ring radius ratio (w/r) of the ring resonator structure is kept smaller than 0.2 to avoid excitation of possible higher order modes [6]. The first ten resonances of the large rings (2 GHz and 4 GHz designs) and the first six

Table 5.1 Physical parameters of ring resonators. The relative permittivity and loss tangent of the substrates are ε_r = 6.15, $tan\ \delta$ = 0.0027 for RT/Duroid 6006 and ε_r = 2.2, $tan\ \delta$ = 0.0009 for TLY-5 with a few percent variation from 2 to 40 GHz.

Substrate			Ring Radius (r)	Gap (g)	Microstrip Width (w)	Fundamental Resonant Frequency
Material	Thickness (h_s)	Copper Cladding				
RT/Duroid 6006	0.625 mm	17.8 μm	11.2 mm	120 μm	0.91 mm	2 GHz
TLY-5	0.381 mm	17.5 μm	8.66 mm	100 μm	1.16 mm	4 GHz
TLY-5	0.254 mm	17.5 μm	5.84 mm	70 μm	0.71 mm	6 GHz

resonances of the small ring (6 GHz design) are within the desired frequency range of measurement (up to 40 GHz), have clear and sharp peaks (Q>100), and are suitable for calculations to determine the electrical properties of the microcomposite slabs. The slabs are superimposed on the rings and the whole circuit is mechanically stabilized with small plastic clips installed electrically far from the ring resonator.

An Agilent 8722ES Vector Network Analyzer is used to measure the insertion loss of the two-port ring resonators from 1 to 40 GHz. The universal substrate test fixture WK-3001-G from Inter-continental Microwave is directly used to measure the circuits without additional connectors. Two standard SOLT (Short-Open-Load-Through) calibration procedures, one from 1 GHz to 20 GHz, and the other from 20 GHz to 40 GHz are performed to de-embed the loading effects of the test fixture and cables using the Agilent 85056 Calibration Kit. The full 1601 point sweep is used, giving a frequency resolution of 11.87 MHz for the first and 12.49 MHz for the second band. The measured insertion loss of the 6 GHz ring with and without the pure SU-8 slab is shown in Fig. 5.2 as a sample. The sharp resonances are clear and the effect of the slab in lowering the resonances and widening the 3-dB bandwidth is noticeable. Post-processing (Spline interpolation) is performed on the measured data using MATLAB to further enhance the frequency resolution to less than 1 MHz. The resonant frequencies, 3-dB bandwidths, and consequent Q factors of each resonance of the rings before and after insertion of the slabs are extracted from the data. The relative permittivity and loss tangent of the slabs are calculated at the resonant frequencies using Equation 5.3 and 5.7, respectively.

5.3.1 SU-8 and SU-8 Microcomposites

In Fig. 5.6 the dielectric constant and loss tangent for pure SU-8 resist, extracted from measurements of two-layer microstrip ring resonators, are shown. An average value of 3.2 is achieved for the relative permittivity at 30 GHz. The dielectric loss tangent increases over the frequency and it is 0.03 at 30 GHz. The

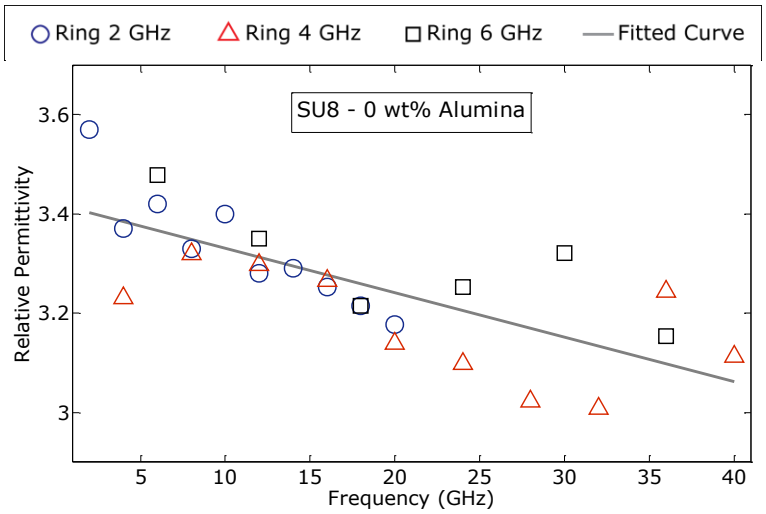

(a)

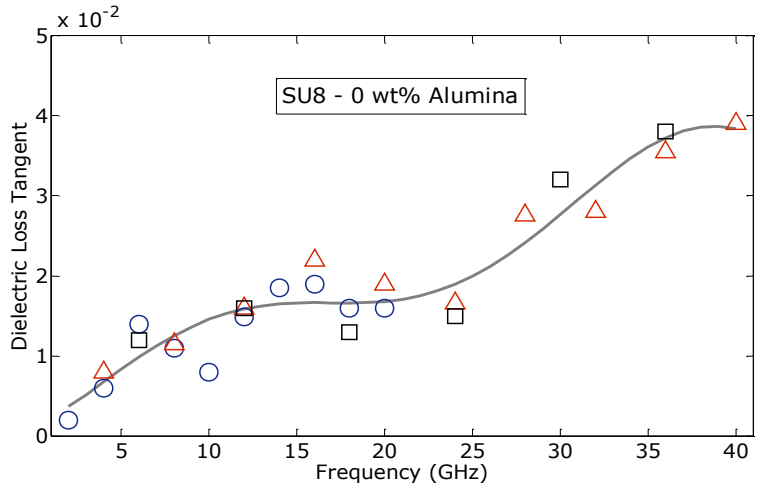

(b)

Fig. 5.6. (a) Dielectric constant and (b) loss tangent vs. frequency of SU-8 resist. The curves are fitted to the scattered measured points using comprehensive regression analyses (Matlab cftool), for visualization purpose and to show trends of dielectric properties over frequency.

measurement results are comparable to the results reported by other research groups [15]- [17].

Fig. 5.7 shows the dielectric constant from 2 GHz to 40 GHz of the fabricated SU-8 microcomposites with different proportions of alumina micropowder content. The results of the different ring designs are in good agreement at the common frequency points over the entire frequency range. The best-fit line is also illustrated to indicate the overall behaviour of the permittivity versus frequency. A worst case variation of about ±5% is observed for the measured points with

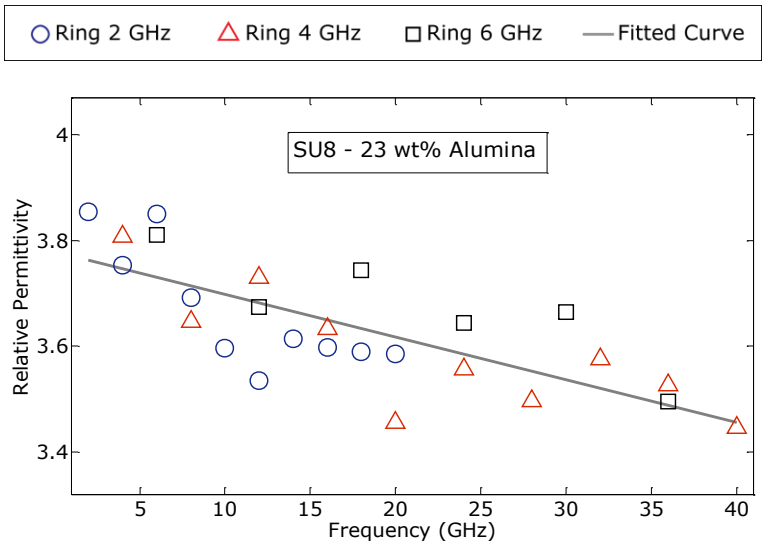

(a)

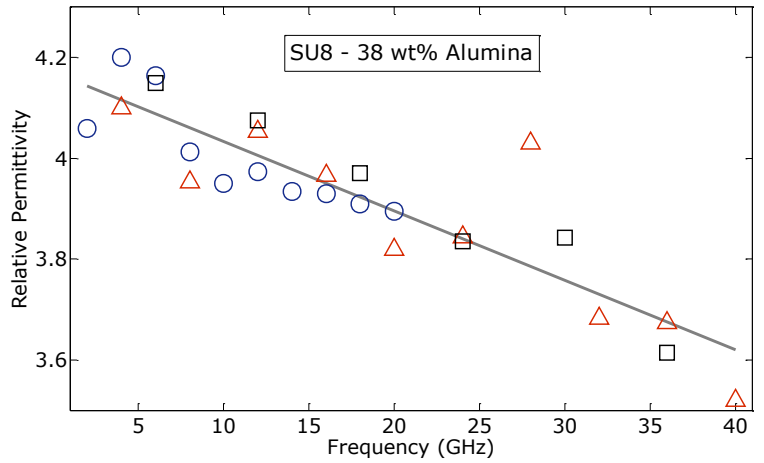

(b)

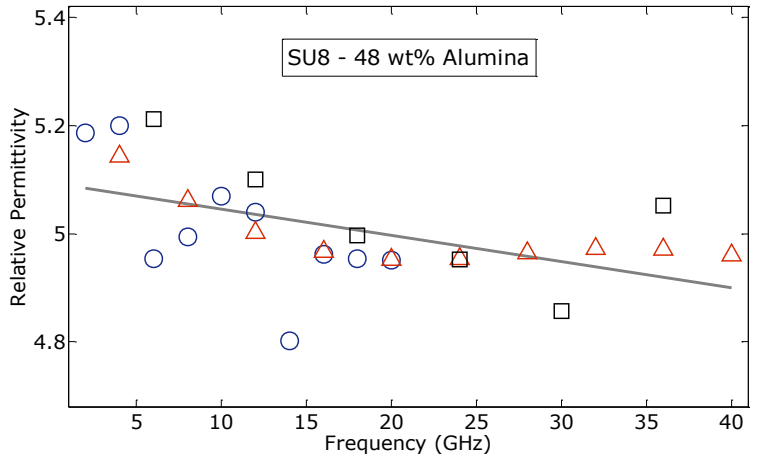

(c)

Fig. 5.7. Dielectric constant of SU-8 microcomposites made with different portions of alumina micropowder.

respect to this line; however a majority of points are closer to it. For all samples, the dielectric constant is stable with frequency, with a slight linear drop as the test frequency increases 20-fold. This trend is consistent with the dielectric behaviour of other polymer-ceramic composites [18], [19]. It can be observed that the addition of alumina content nonlinearly increases the relative permittivity of the composites. It results in considerable increase in the relative permittivity between 0 and 23 wt%, and between 23 and 38 wt% samples, and even greater increase between 38 and 48 wt% samples. The approximate average relative permittivities are 3.2, 3.6, 3.9, and 5.0 for composites of 0, 23, 38, and 48 weight percents of alumina content, respectively. The considerable difference between the permittivities of 38 and 48 wt% samples may be related to a transition phase between the two main schemes of dielectric behaviours (i.e. polymer towards ceramic).

The measured loss tangent versus frequency for the SU-8-alumina composites is shown in Fig. 5.8. A second order Fourier regression illustrates the general trend of the loss tangent versus frequency. In all samples, the loss tangent increases with frequency while two relaxations occur around the beginning and end of the frequency band. For frequencies below 5 GHz, the dielectric loss tangent remains less than 0.009 in all cases. From 5 GHz to 20 GHz, the dielectric loss decreases as the weight ratio of alumina content increases. The average values are 0.015, 0.014, 0.012, and 0.008 for 0 wt%, 23 wt%, 38 wt%, and 48 wt% samples respectively. In the upper frequency band of 20 GHz to 40 GHz, the loss tangent of 23 wt% microcomposite is greater than pure SU-8 while the results are similar for 38 wt% and 0 wt% samples. The higher dielectric loss of 23 wt% ceramic-polymer microcomposite is an unusual behaviour which can be related to the interaction of the ceramic and polymer matrix. The loss tangent of 48 wt% sample is considerably lower than the other samples, suggesting a minimum percentage of ceramic content in the composite is required to achieve low loss tangent at frequencies greater than 20 GHz. More specifically, the value observed

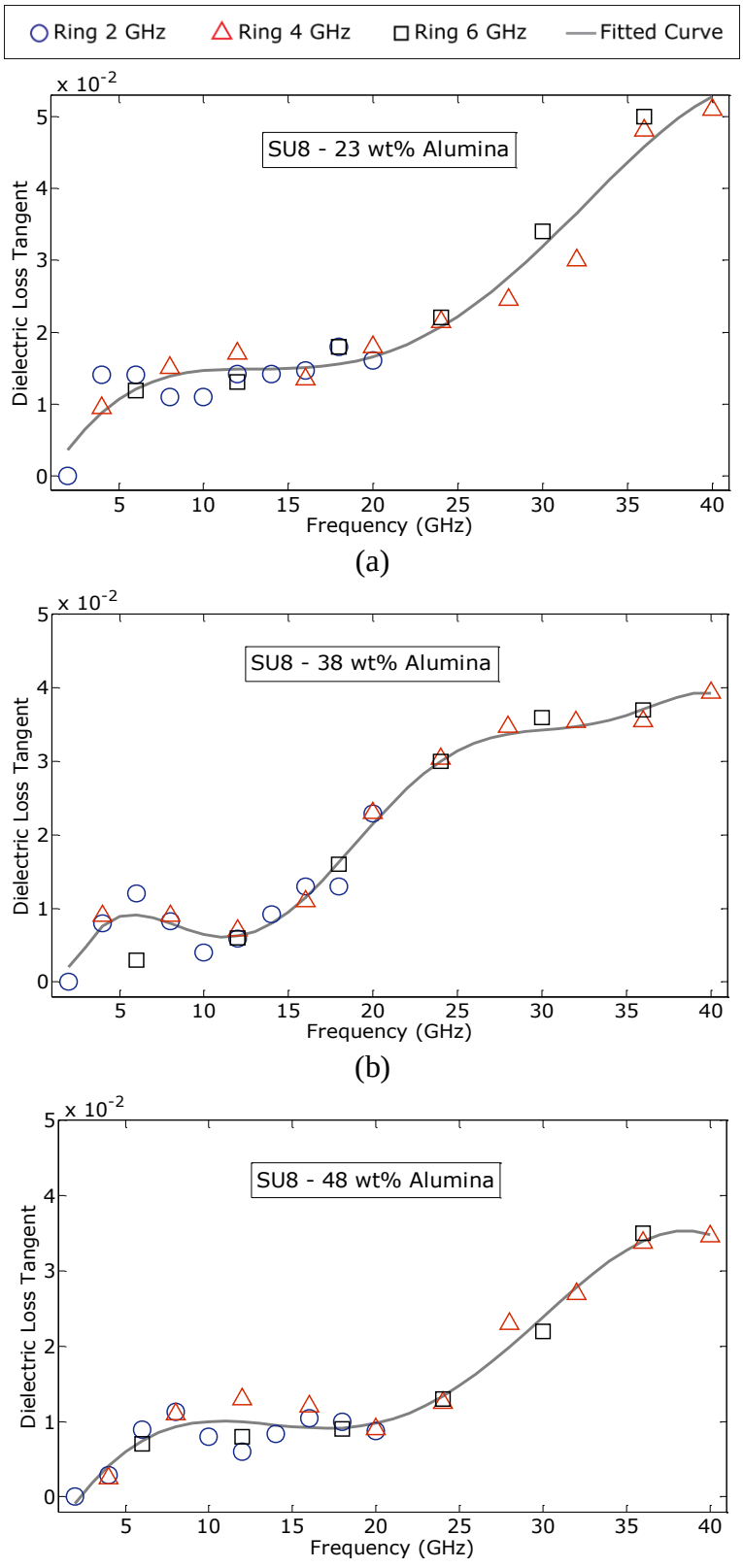

Fig. 5.8. Loss tangent of SU-8 microcomposites made with different portions of alumina micropowder.

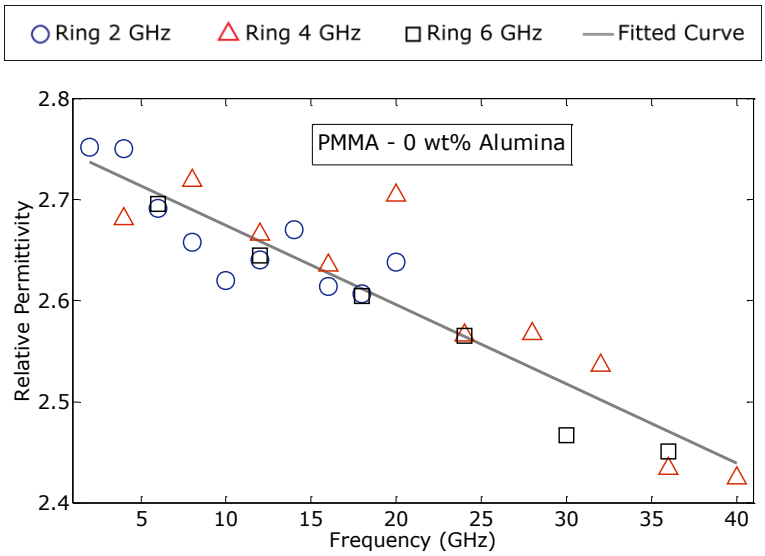

(a)

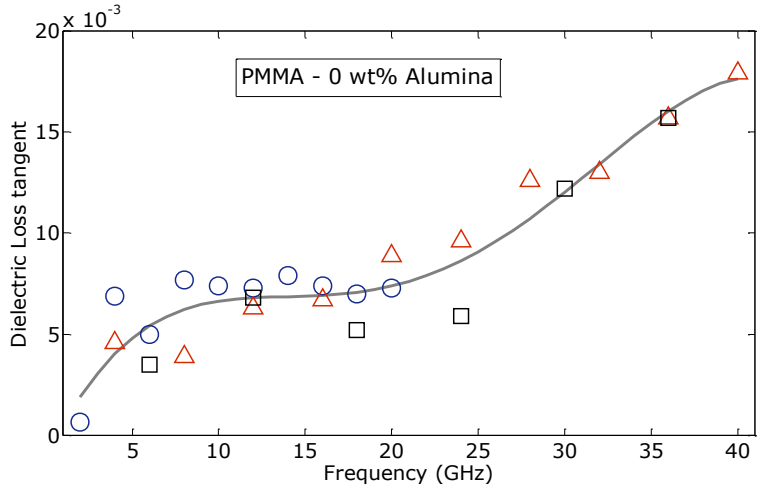

(b)

Fig. 5.9. (a) Dielectric constant and (b) loss tangent vs. frequency of PMMA resist. The curves are fitted to the scattered measured points using comprehensive regression analyses (Matlab cftool), for visualization purpose and to show trends of dielectric properties over frequency.

between 20 GHz and 25 GHz is about $tan\ \delta \approx 0.01$ for 48 wt% polymer microcomposite which is a great improvement for microwave applications.

5.3.2 PMMA and PMMA Microcomposites

Fig. 5.9 shows the dielectric constant and loss tangent of pure PMMA photoresist from 2 to 40 GHz. An average value of $\varepsilon_r = 2.6$ with a slight decrease with increasing frequency is obtained. The loss tangent of PMMA is considerably

lower than that of SU-8 and shows values between 0.009 and 0.018 in the upper frequency range of measurement (20 – 40 GHz).

The measured permittivity and loss tangent of the fabricated PMMA microcomposites are shown in Fig. 5.10 and 5.11, respectively. Again, good agreement is achieved among the results of different rings. Both the permittivity and loss tangent are noticeably lower compared with the SU-8 microcomposites with identical portions of alumina content. This is consistent with the similar behaviour of other ceramic-polymer composites [20]. As the weight percentage of the alumina increases, the permittivity rises and the big step occurs between 23 wt% and 38 wt% samples. The average values are 2.6, 2.8, 3.6, and 4.0 for microcomposites of 0, 23, 38, and 48 weight percents of alumina content, respectively. The loss tangent value is better than 0.005 for all microcomposite samples below 5 GHz. From 5 GHz to 20 GHz, the dielectric loss decreases as the weight ratio of alumina content increases. The average values are 0.007, 0.006, 0.005, and 0.004 for 0, 23, 38, and 48 wt% samples respectively. With the exception of the 23 wt% sample, the dielectric loss tangent decreases as the weight ratio of alumina content increases in the frequency band of 20 to 40 GHz. The loss tangent of 48 wt% microcomposite is considerably lower than the other samples, and shows a loss tangent value approximately better than 0.01 for frequencies below 35 GHz. The unusual loss behavior of 23 wt% alumina-PMMA microcomposite is similar to that of the SU-8 sample and reinforces the assumption that a minimum amount of ceramic content (about 40 wt%) is required to achieve composite loss improvements in microwave applications at frequencies greater than 20 GHz.

5.4 Method Evaluation

A particular advantage of the proposed dielectric properties measurement method is to remove conductor and radiation loss calculations. In other words, it is supposed that the sum of the conductor and radiation loss is similar before and

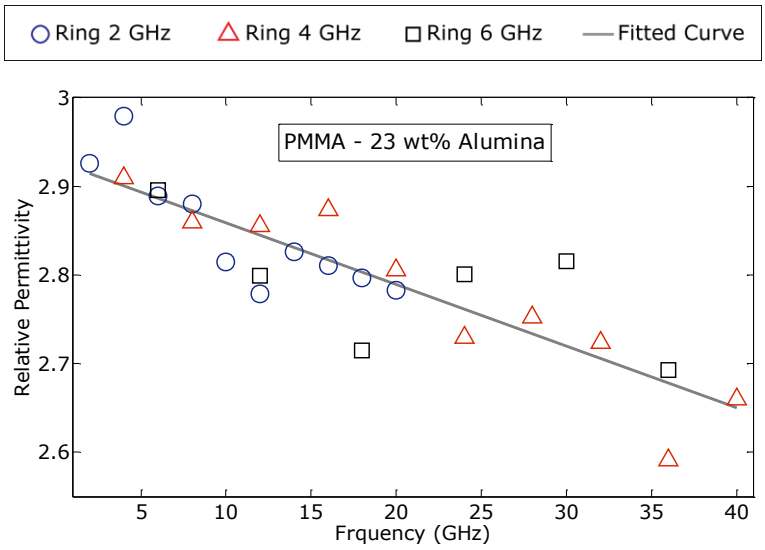

(a)

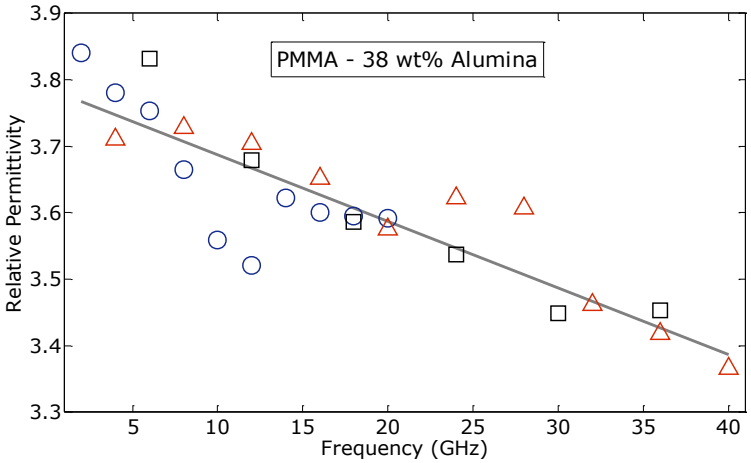

(b)

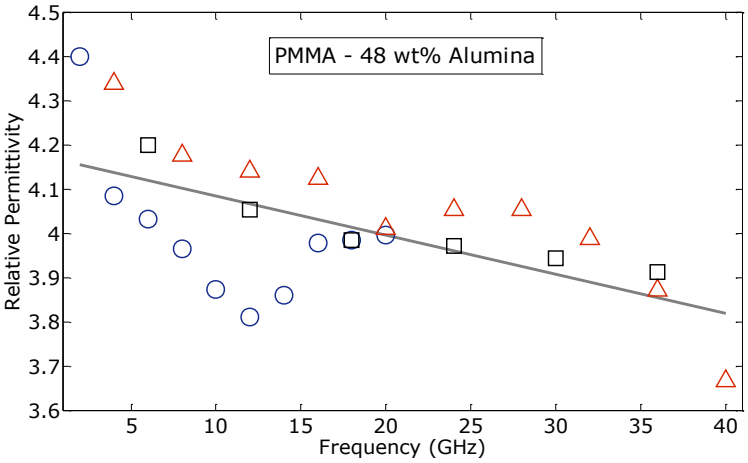

(c)

Fig. 5.10. Dielectric constant of PMMA microcomposites made with different portions of alumina micropowder.

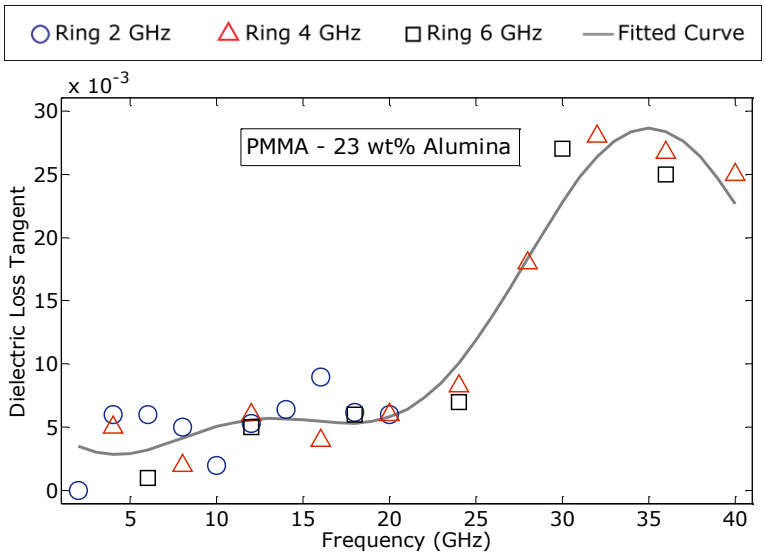

(a)

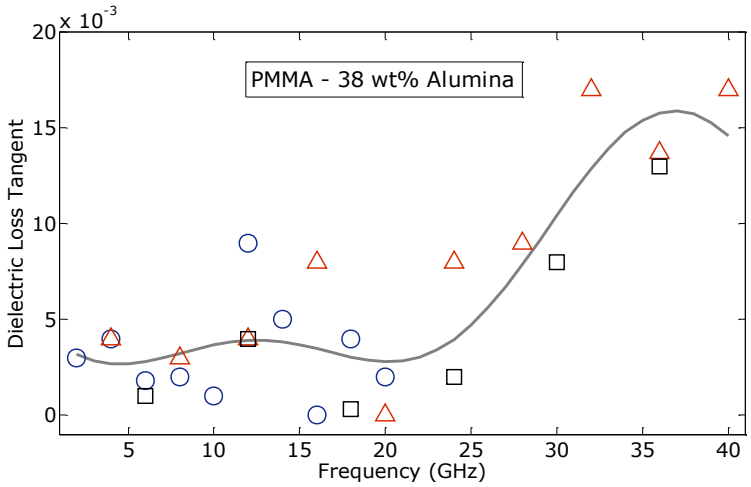

(b)

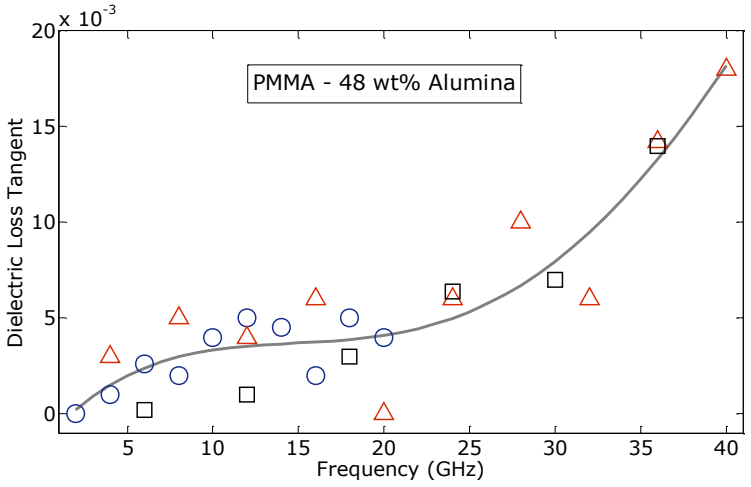

(c)

Fig. 5.11. Loss tangent of PMMA microcomposites made with different portions of alumina micropowder.

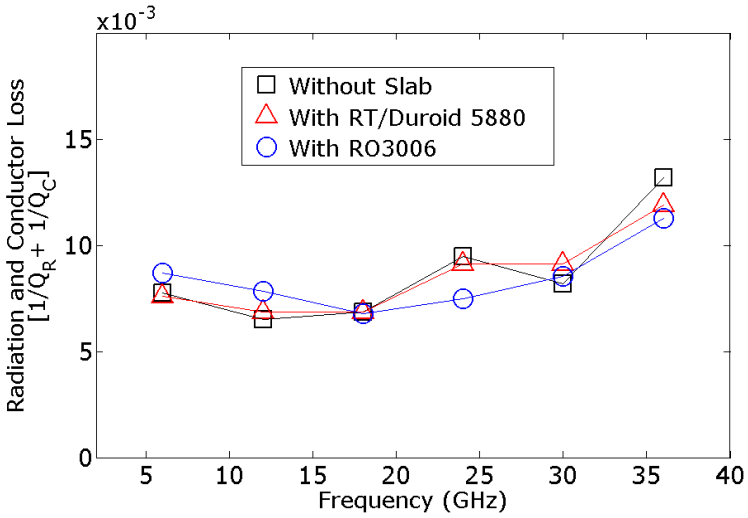

Fig. 5.12. Comparison of sum of radiation and conductor losses before and after slab insertion on the 6 GHz microstrip ring resonator. RT/Duroid 5880 and RO 3006 were superimposed as dielectric slabs.

after slab insertion. To verify this assumption the unloaded (Q_U) and dielectric (Q_D) quality factors of the one-layer (without slab) and two-layer (with slab) ring resonators with samples of known permittivities and loss tangents up to 40 GHz (provided by Rogers and Taconic corporations) are extracted from insertion loss measurements and Schneider formulation for multilayer microstrip configurations (5). The sum of conductor and radiation losses for one-layer and two-layer microstrip resonators can be calculated as follows at the resonant frequencies:

$$\frac{1}{Q_C}+\frac{1}{Q_R}=\frac{1}{Q_U}-\frac{1}{Q_D} \tag{5.19}$$

Fig. 5.12 compares the cumulative conductor and radiation losses of the one-layer microstrip ring resonator with the two-layer microstrip ring resonator for the 6 GHz design (TLY 5 substrate material) when RT/Duroid 5880 (ε_r = 2.2 ± 0.02, tan δ_e = 0.0006-0.0011) and RO 3006 (ε_r = 6.15 ± 0.15, tan δ_e = 0.002-0.003) are superimposed as dielectric slabs. An excellent agreement is achieved among the three curves, confirming the accuracy of the assumption. The total conductor and radiation loss increases with increasing frequency and a maximum of 1.9×10^{-3} deviation occurs at 36 GHz between the ring resonator without slab and with the

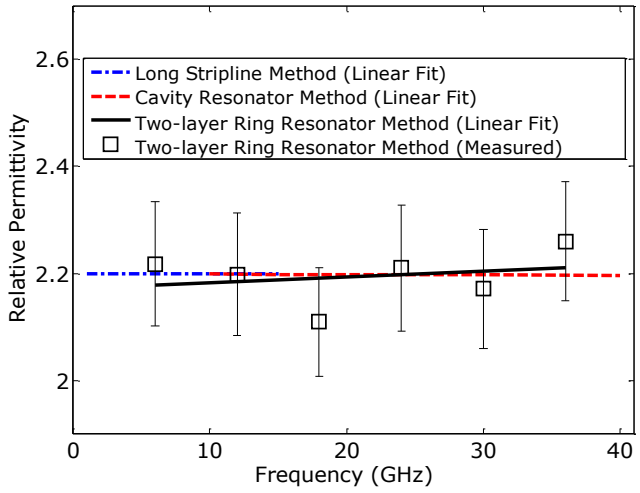

(a)

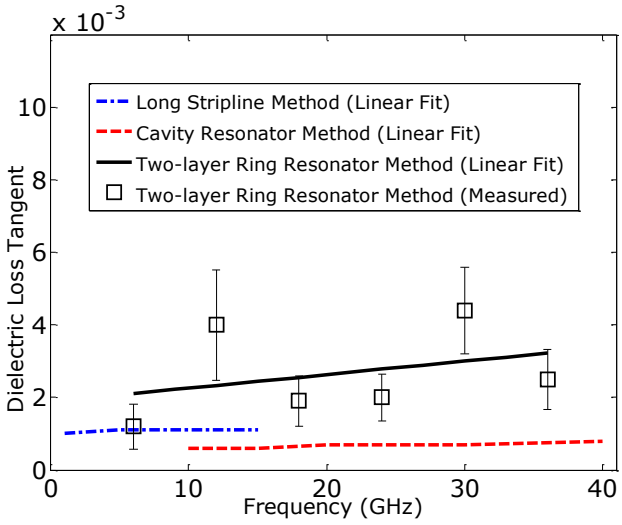

(b)

Fig. 5.13. Comparison of other measurement techniques with the proposed two-layer ring resonator method. RT/Duroid 5880 slab is superimposed on the 6 GHz ring resonator. The error bars are calculated based on uncertainties in resonant frequency and Q-factor measurements, plus in microstrip width, substrate thickness and substrate permittivity. (a) Relative permittivity; (b) Dielectric loss tangent.

RO 3006 slab. Other experiments show that by increasing the substrate permittivity (e.g. 2 GHz ring resonator design with RT/Duroid 6006 as substrate) the sum of the conductor and radiation losses decreases to about one third of that of the 6 GHz ring and becomes less important in dielectric loss calculation using this method.

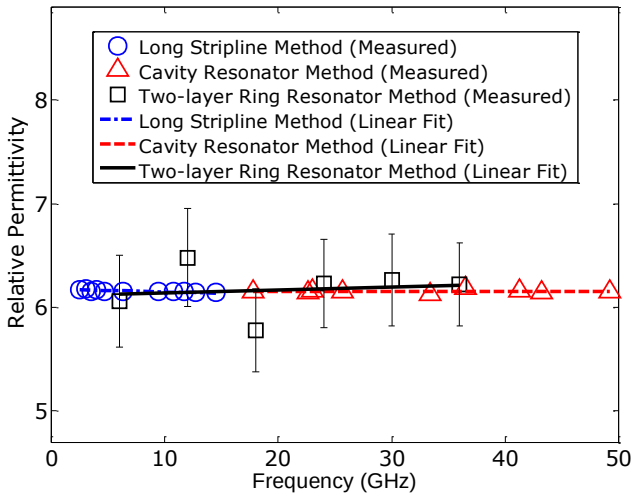

(a)

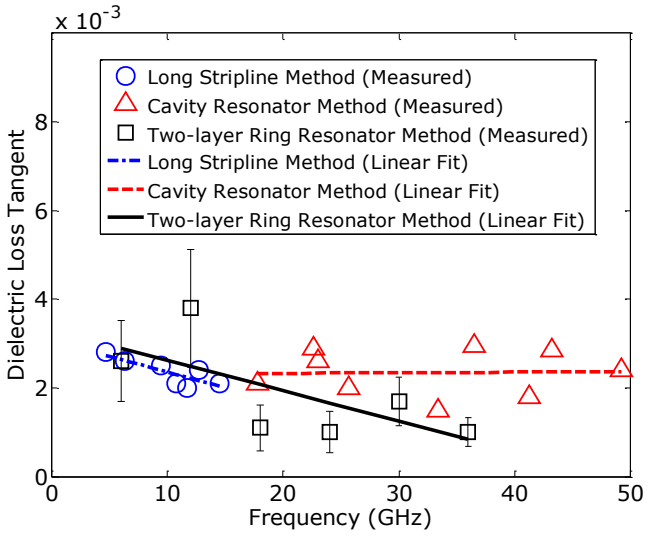

(b)

Fig. 5.14. Comparison of other measurement techniques with the proposed two-layer ring resonator method. RO 3006 slab is superimposed on the 6 GHz ring resonator. The error bars are calculated based on uncertainties in resonant frequency and Q-factor measurements, plus in microstrip width, substrate thickness and substrate permittivity. (a) Relative permittivity; (b) Dielectric loss tangent.

The results of other measurement methods provided by the manufacturers are compared with the proposed technique for the low loss materials in Fig. 5.13 and Fig. 5.14. In general, the two-layer ring resonator plot gives a good approximation of the values found by the standard long stripline and cavity resonator methods for

RT/Duroid 5880 and RO 3006 slabs. The relative permittivity achieved by the ring resonator technique varies within about 5% while average values of 2.17 and 6.11 (very close to 2.2 and 6.15 for the other methods) are obtained over the entire frequency for RT/Duroid 5880 and RO 3006, respectively. The loss tangent achieved by the ring resonator shows values between 0.001-0.004 over a 6 - 36 GHz frequency band and agrees well with other measurement techniques. It is to be noted that the results of the ring resonator technique should be more accurate for higher dielectric loss materials (i.e. SU-8 and PMMA). These experiments show that the relative permittivities and loss tangents of X-ray resist-ceramic microcomposites achieved in previous section using the two-layer ring resonator are sufficiently accurate and reliable.

5.5 Summary

Electrical properties of X-ray resist-alumina microcomposites were investigated and measured from 2 to 40 GHz using a new approach to verify the performance of the materials for antenna applications. The ceramic micropowders are mixed with resist polymers, improving microwave properties while maintaining X-ray sensitivity and allowing fabrication of high structural quality components in thick slabs using lithographic processing. The measurement method utilizes a modified ring resonator technique in one-layer and two-layer microstrip configurations and eliminates the requirement to metalize the samples. Complex and inaccurate equations to calculate the conductor and radiation losses are removed in this method. By fabricating only one ring resonator, one can measure electrical properties of as many materials as desired. The proposed technique can also be used to measure materials in non-substrate forms such as powders and liquids which cannot be measured using stripline and direct microstrip methods.

References

[1] P. Troughton, “Measurement technique in microstrip,” *Electron. Lett.*, vol. 5, no. 2, pp. 25-26, Jan. 1969.

[2] D. C. Thompson, O. Tantot, H. Jallageas, G. E. Ponchak, M. M. Tentzeris, and J. Papapolymerou, “Characterization of liquid crystal polymer (LCP) material and transmission lines on LCP substrates from 30 to 110 GHz,” *IEEE Trans. Microw. Theory Tech.*, vol. 52, no. 4, pp. 1343-1352, April 2004.

[3] A. Rashidian, D. M. Klymyshyn, M. Tayfeh Aligodarz, M. Boerner, and J. Mohr, “Characterization of photoresist-based microcomposites for polymer resonator antennas,” to be submitted to *IEEE Trans. Antennas and Propagat*.

[4] A. Horn, Dielectric constant and loss of selected grades of Rogers high frequency circuit substrates from 1 – 50 GHz (Technical report 5788), Rogers Corporation, One Technology Drive, Rogers, CT 06263.

[5] J. Svacina “Analysis of multilayer microstrip lines by a conformal mapping method,” *IEEE Trans. Microw. Theory Tech.*, vol. 40, no. 4, pp. 769-772, 1992.

[6] K. Chang and L. H. Hsieh, Microwave Ring Circuits and Related Structures. Hoboken, New Jersey: John Wiley & Sons, 2004.

[7] M. V. Schneider, “Dielectric loss in integrated microwave circuits,” *The Bell System Technical Journal*, pp. 2325-2332, Sep. 1969.

[8] E. Belohoubek and E. Denlinger, “Loss considerations for microstrip resonators,” *IEEE Trans. Microw. Theory Tech.*, vol. 23, no. 6, pp. 522-26, 1975.

[9] W. J. Getsinger, "Microstrip dispersion model," *IEEE Trans. Microw. Theory Tech.*, vol.21, no.1, pp. 34- 39, Jan 1973.

[10] T. C. Edwards, and R. P. Owens, “2-18 GHz dispersion measurements on 10-100 ohm microstrip lines on sapphire,” *IEEE Trans. Microw. Theory Tech.*, vol. 24, no. 8, pp. 505-513, August 1976.

[11] M. Kirsching and R. H. Jansen, “Accurate model for effective dielectric constant of microstrip with validity up to millimetre-wave frequencies,” *Electron. Lett.*, vol. 18, no. 6, pp. 272-273, March 1982.

[12] MicroChem Corporation, USA webpage http://www.microchem.com.

[13] P. Meyer, J. Schulz, and L. Hahn, "DoseSim: Microsoft-windows graphical user interface for using synchrotron x-ray exposure and subsequent development in the LIGA process," *Review of Scientific Instruments*, pp. 1113-1119, 2003.

[14] J. Heinola and K. Tolsa, "Dielectric characterization of printed wiring board materials using ring resonator techniques: a comparison of calculation models." *IEEE Trans. Dielectrics and Electrical Insulation*, vol. 13, no. 4, pp. 717-726, August 2006.

[15] R. Osorio, Micromachined transmission lines for microwave applications, Ph.D. dissertation, Univ. Freiburg, Germany, 2003.

[16] F. D. Mbairi and H. Hesselbom, "High frequency design and characterization of SU-8 based conductor backed coplanar waveguide transmission lines," *Proc. of Intl. Symp. on Advanced Packaging Material*, pp. 243-248, March 2005.

[17] J. R. Thorpe, D. P. Steenson, and R. E. Miles, "High frequency transmission line using micromachined polymer dielectric," *Electron. Lett.*, vol. 34, no. 12, pp. 1237-1238, June 1998.

[18] Y. Rao, J. Yue, and C. P. Wong, "Material characterization of high dielectric constant polymer-ceramic composite for embedded capacitor to RF application," *Active and Passive Elec. Comp.*, vol. 25, no. 1, pp. 123-129, 2002.

[19] K. A. O'Connor, J. Smith, R. D. Curry, "Dielectric characterization of polymer-ceramic nanocomposites," *IEEE Proc. Pulsed Power Conference (PPC '09)*, pp. 336-341, 2009.

[20] J. Xu and C. P. Wong, "Effect of the polymer matrices on the dielectric behavior of a percolative high-k polymer composite for embedded capacitor applications," *Journal of Electronic Materials*, vol. 35, no. 5, pp. 1087-1094, 2006.

Chapter 6

Photoresist-Based Polymer Resonator Antennas

The results of previous chapters are combined to realize and introduce pure photoresist and photoresist-based resonator antennas in this chapter. The ideas of strip-fed and slot-fed low permittivity antennas, discussed in Section 3.3 and 3.4, are progressed to detailed fabrication. Direct and indirect X-ray lithography fabrication methods, introduced in Chapter 4, are applied and all the measurements on electrical properties of the resulting composite materials are performed using two-layer microstrip ring resonator which was introduced in Chapter 5. It is worth mentioning that the ideas of high-aspect-ratio high-permittivity and multisegment antennas require more experiments on material preparation (especially to produce high permittivity photoresist composites at high frequencies) and therefore are considered for future developments.

6.1 SU-8 Resonator Antennas

Originally developed and patented by IBM in 1989 and commercially introduced by MicroChem Corporation in 1996, SU-8 rapidly found wide use in UV and X-ray lithography as a negative tone photoresist for microsystem technology applications [1]. Its very low optical absorption in UV and X-ray ranges leads to uniform exposure conditions for thicknesses up to a few millimetres resulting in high structural quality and excellent sidewall verticality. Cured SU-8 is highly resistant to solvents, acids and bases and has excellent thermal stability, making it attractive for applications in which the SU-8 is considered as a permanent part of the device. For instance, it is used in fabrication

of X-ray lenses [2], metamaterials [3], single-mode and multi-mode optical waveguides [4], [5], and micro channels for bio applications [6].

Efforts have also been done to utilize SU-8 in lithographic processes for microwave and antenna applications. However, it has been mostly used as a supportive (or structural) material in the fabrication process. For example, SU-8 is employed as a core material to fabricate tall metallic transmission lines and inductors [7]. It is lithographically shaped to create a metallic waveguide filter and horn antenna [8], [9]. A micromachined SU-8 ring is also fabricated in [10] to produce a suspended patch antenna. Only a few researches, limited to transmission lines, utilized SU-8 as a microwave material [11], [12], [13].

In this section, radiation properties and impedance characteristics of lithographically patterned SU-8 structures are discussed [14]. Wideband operation is examined by merging the resonances of the SU-8 resonator antenna and an aperture antenna. The effects of SU-8 loss tangent and substrate permittivity on antenna gain and efficiency are addressed.

6.1.1 Hybrid SU-8/Aperture Antenna

To realize photoresist antennas, precise ultra thick SU-8 structures are fabricated based on the direct X-ray lithography fabrication method discussed in Chapter 4. Fig. 6.1 shows the final released structures and key parameters of the fabrication. The dielectric loss tangent and permittivity of the pure SU-8 photoresist, measured using the multilayer microstrip ring resonator technique discussed in Chapter 5, are 0.015~0.035 and 3.5~3.2 from 10 GHz to 30 GHz, respectively, as shown in Fig. 5.6. The SU-8 structure is fed by the slot-coupled excitation method shown in Fig. 3.16 and adjustments are performed using the parametric study in Section 3.3.4. The 2.4 mm wide 50 ohms microstrip line is designed on the bottom of a microwave substrate with a low permittivity of 2.2. The fabricated SU-8 resonator antenna excited by a $W \times S$ = 3.5 mm × 0.7 mm aperture on a 46 mm square ground plane is measured using an Agilent 8722ES

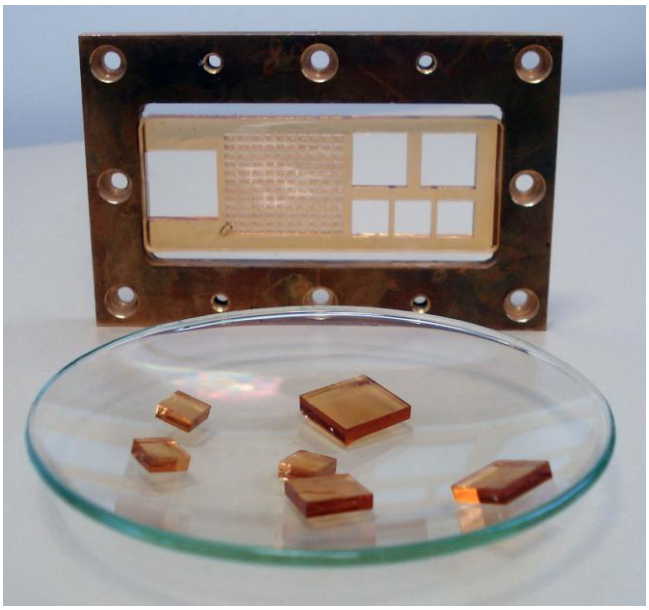

Fig. 6.1. SU-8 structures following 30 minutes development in PGMEA.
The photoresist layer is prepared using the double casting procedure. SU-8(10) is poured onto a metallic frame with sacrificial polyimide layer on the bottom side and soft baked at 95°C to reduce the solvent content to 4 and 10 percent for the first and second layer respectively. The prepared 2 mm SU-8 layer is exposed to X-rays through a titanium mask with square patterns [15]. A bottom dose of 10 J/cm^3 and a top-to-bottom dose ratio of 4 were maintained in this experiment.

vector network analyzer. Fig. 6.2 shows the reflection coefficient of the antenna along with simulation result. As discussed in Section 3.3.4, the first resonant mode is related to the aperture and the second mode is due to the SU-8 resonance. The measured -10 dB impedance bandwidth is more than 33 percent. Differences between measured and simulated results are mainly due to the RTV silicone adhesive which was used to assemble the SU-8 on the aperture.

6.1.2 Effects of SU-8 Loss on Antenna Gain and Efficiency

The electrical properties of SU-8 (i.e. permittivity and loss tangent) have been measured at millimetre-wave frequencies in the existing literature [11], [12], [13], [16]. However, these properties are affected by not only the frequency in which the measurement is performed but also the fabrication processing parameters (e.g. exposure dose and baking conditions) and different types of commercial SU-8 material (e.g. SU-8(5), SU-8(10), and SU-8(100)). Although permittivity

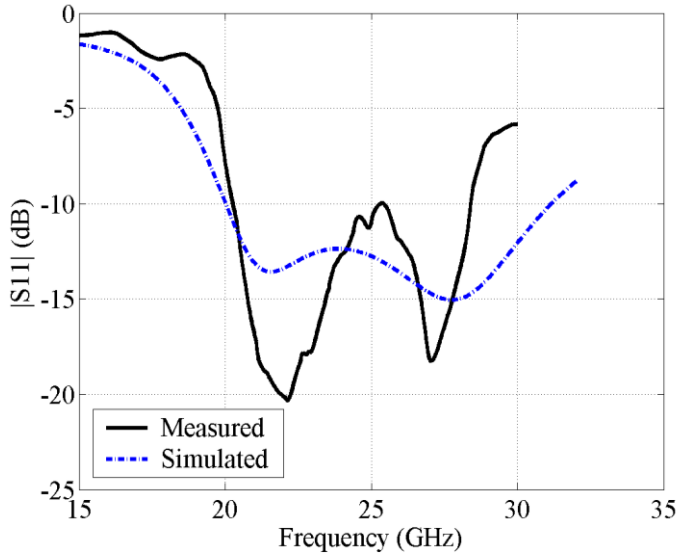

Fig. 6.2. Reflection coefficient of SU-8 resonator antenna. ($A \times B \times h$ = 5.7 × 5.7 × 2 mm, ΔL = 1 mm)

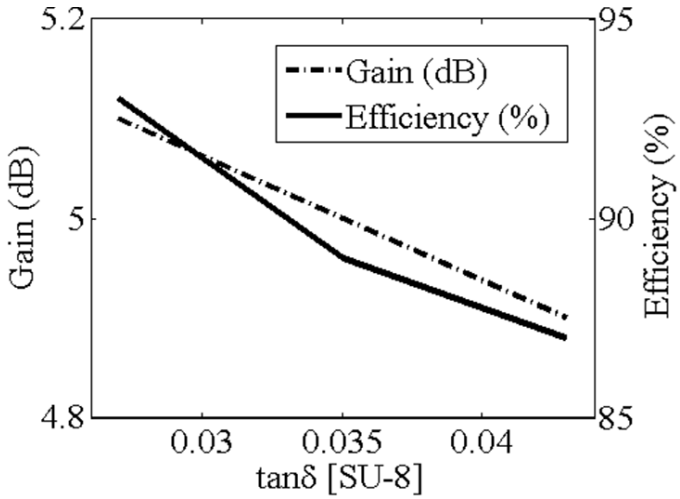

Fig. 6.3. Gain and efficiency vs. SU-8 loss tangent. ($A \times B \times h$ = 5.7 × 5.7 × 2 mm, ΔL = 1 mm)

variation of SU-8 does not considerably change the radiation properties of the SU-8 resonator antenna, variation of electric loss tangent can affect the gain and efficiency of the antenna. A possible range of SU-8 electric loss tangent from 0.027 to 0.043 is considered in simulations to investigate gain and efficiency variations of the antenna. As shown in Fig. 6.3, the antenna efficiency changes from 93 percent to 87 percent while the antenna gain reduces from 5.1 to 4.9.

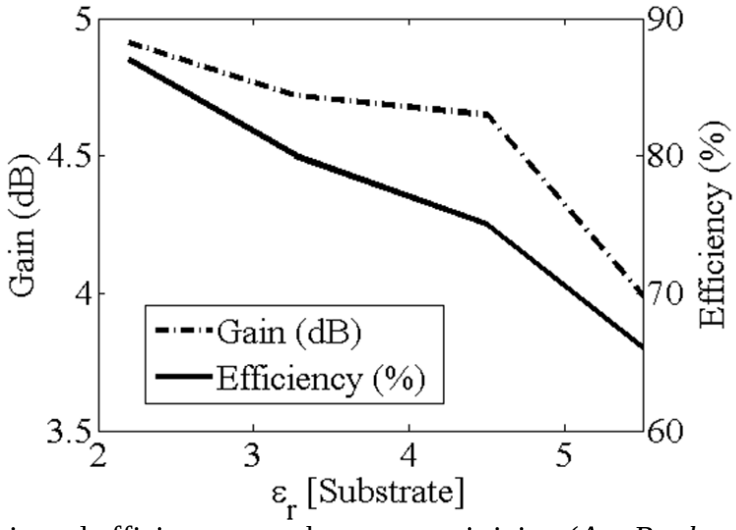

Fig. 6.4. Gain and efficiency vs. substrate permittivity. ($A \times B \times h = 5.7 \times 5.7 \times 2$ mm, $\Delta L = 1$ mm)

6.1.3 Effects of Substrate Permittivity on Antenna Gain and Efficiency

To show the effects of microwave substrate on the radiation properties of the SU-8 resonator antenna, the substrate permittivity is changed from 2.2 to 5.5. A 50 Ω microstrip line is designed for all cases and slot dimensions (W, S) and microstrip length variation (ΔL) are adjusted to achieve the best possible coupling for the SU-8 resonance. All other parameters such as antenna size and properties are kept constant. Fig. 6.4 shows the simulation results. The efficiency of the antenna drops from 87 percent for the permittivity of 2.2 to less than 70 percent for the permittivity of 5.5. Meanwhile, the antenna gain decreases from 4.9 to 3.9. This can be attributed mainly to the low permittivity of SU-8. Therefore, to preserve the high efficiency and gain of the SU-8 resonator antenna, low permittivity microwave substrates should be used.

6.2 Microcomposite Slot-Fed Antennas

Each combination of polymer and ceramic with tuned parameters is a new material with properties attributed not only to the source materials but also their interactions. The improved thermal stability of alumina-PEEK composite, for instance, is attributed to the mutual effect of ceramic particles and polymer matrix

[17]. Different distributions of ceramic micropowder can produce a wide range of dielectric constants. Compared to pure ceramics, they have lower density making them lightweight and suitable for mobile applications and also easier to machine. Due to these fascinating characteristics, polymer-ceramic composites have been proposed for a wide variety of applications.

Polymer-ceramic composites are utilized as dielectrics for high energy density and embedded capacitors [18], [19], microwave substrates for microstrip filters [20], and packaging material for electronic applications [21]. They have also been used in medical applications for the development of high performance transducers in which mechanical energy of the composites converts into electrical energy and vice versa [22].

Due to their remarkable electromagnetic and mechanical properties, polymer composites have attracted considerable interest for antenna applications as well. As a result, many composites are optimized and reported in research papers to demonstrate the superiority of these artificially modified materials in antenna performance. A composite of ceramic powder and an elastomeric polymer has been utilized to make pliable substrates and show conformal patch antennas [20]. In another attempt, electrically scanned microstrip antennas were fabricated on a substrate of modified polymer-ceramic composite [23]. A magnetic polymer composite has also been developed for miniaturization of microwave devices and consequently a miniaturized helical antenna loaded with the developed material was presented [24]. Moreover, a ferromagnetic composite was introduced in [25] and a magneto dielectric antenna was proposed for mobile applications. Polymer-metal is another kind of composite which has shown applications in smart antennas [26].

Polymer binders with different characteristics have been chosen in these applications to fulfil special requirements. For instance, Polydimethylsiloxane is used in [20] for its elastic behavior and Polytetrafluoroethylene in [21] for its dielectric properties and chemical resistances. In this work, X-ray sensitive

polymers were used to demonstrate lithographic fabrication of thick antenna structures with precise features. With optimized parameters, X-ray lithography can make small, three dimensional dielectric structures even with complicated shapes.

6.2.1 Prototype Preparation

To demonstrate microcomposite antennas with different weight percents of ceramics, SU-8(10) is mixed with alumina micropowder to achieve a homogeneous composite. A specific amount of the mixture is put into a metallic frame with 100 microns polyimide foil on the bottom side, to create a 2 mm thick polymer composite layer. After pre-baking at 95°C, the polymer composite is exposed to X-rays through a titanium mask (shown in Fig. 4.2) at ANKA storage ring. The sample is then developed at room temperature using propylene glycol monoether acetate (PGMEA). Fig. 6.5(a) shows structures during the development process. A post-baking procedure can be performed at the end with a very slow temperature ramp to further harden the structures. The scanning electron microscope (SEM) picture of the structure after development and post-baking processes is shown in Fig. 6.5(b), demonstrating the smooth and vertical sidewalls in the thick polymer composite. More descriptions on deep X-ray lithography fabrication of polymer composites and their structural quality can be found in Chapter 4.

In order to evaluate the impedance and radiation performance of the fabricated SU-8 microcomposite structures, they are released from the wafer, attached to a microwave substrate, and fed using the microstrip slot coupling method. The 2.4 mm wide 50 Ω microstrip feedline is machined on the bottom of a 0.787-mm thick Taconic TLY-5 substrate with dielectric constant of 2.2 and loss tangent of 0.0009. The polymer-based rectangular DRA with dimensions of 5.7 mm × 5.7 mm × 2.0 mm and permittivity of 4.2 is coupled by a 4 mm × 1 mm slot on a 35 mm × 35 mm rectangular ground plane. The antenna and the slot are symmetrical

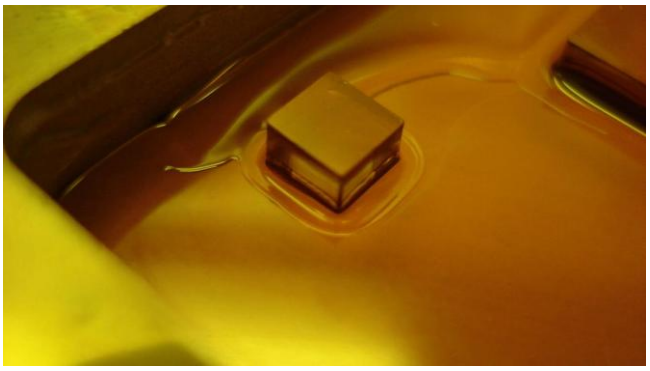

(a)

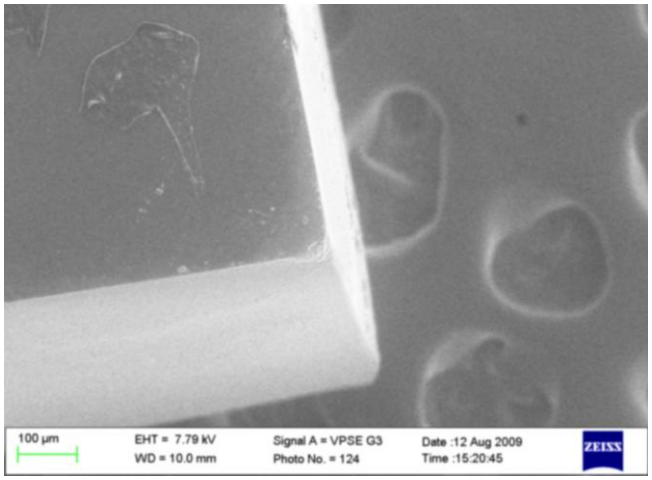

(b)

Fig. 6.5. (a) Development process using PGMEA in direct fabrication of the microcomposite elements; (b) SEM picture of the polymer-based structure.

under the microstrip line with ΔL = 1 mm. The DRA is glued to the ground plane by silicone adhesive sealant. The reflection coefficient is measured using an Agilent 8722ES vector network analyzer. The universal substrate test fixture WK-3001-G from Inter-continental Microwave and a 2.4 mm HP 85133 flexible test cable is used to directly measure the antenna without additional connectors. In order to de-embed the loading effect of the test fixture and the cable on the input impedance of the proposed antenna, a standard calibration was performed using the Agilent 85056A Calibration Kit over a 17 GHz to 30 GHz frequency range. The measurement setup and both sides of the antenna are shown in Fig. 6.6.

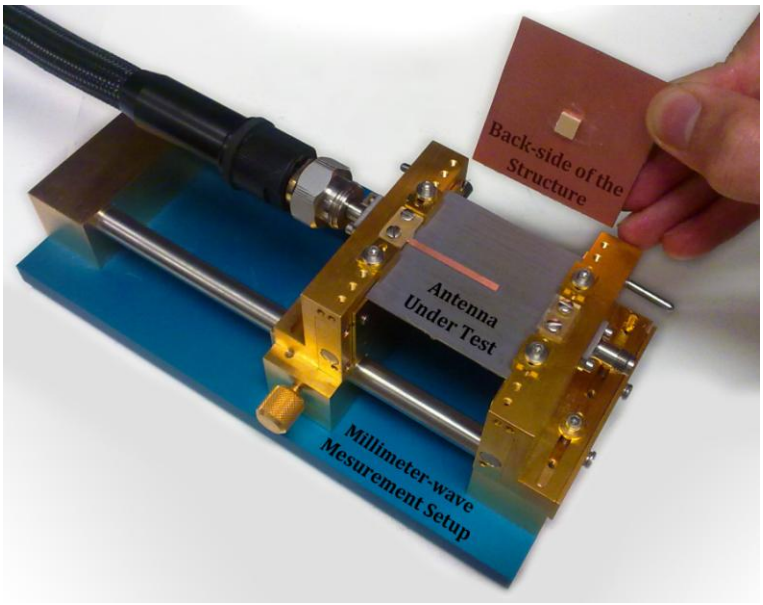

Fig. 6.6. Photograph of the reflection coefficient measurement setup.

6.2.2 Measurement Results

The measured and simulated reflection coefficients for the prototype antennas with 38 wt% and 48 wt% ceramic portions are shown in Fig. 6.7. For the 38 wt% composite antenna, impedance bandwidth of 32% from 21.25 GHz to 29.25 GHz is achieved in the measurement. The measured resonant frequency of the fabricated DRA is 26.1 GHz, which is within 0.8% from the simulation (HFSS: 25.9 GHz), and is consistent with dielectric waveguide model theory (DWM: 24.2 GHz). For the 48 wt% composite antenna, impedance bandwidth of 20% from 20.3 GHz to 24.7 GHz is measured. The measured, simulated, and theoretical resonant frequencies are 22.8, 22.9, and 22.4 GHz, respectively.

Excellent agreements between simulations and measurements, obtained at the resonant frequencies of the antennas, confirm the previously measured material properties of the microcomposite slabs as determined by the ring resonator technique. The 38 wt% antenna structure demonstrates wideband characteristics, while higher coupling and miniaturization are achieved for the 48 wt% antenna structure due to its higher permittivity. Minor discrepancies between measurement and simulation results are mainly due to the RTV adhesive which is used to attach

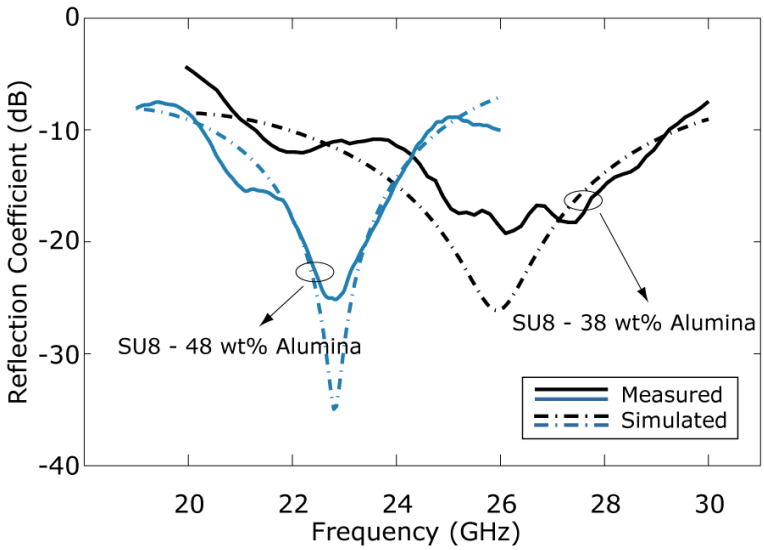

Fig. 6.7. Reflection coefficient of the X-ray lithography fabricated microcomposite antenna elements with different portions of ceramics. Dimensions are 5.7 mm × 5.7 mm × 2.0 mm.

the antenna elements on the slot-coupled feed circuit. This problem can be avoided by fabricating the antenna elements directly on the final substrate and feed circuits which is viable using X-ray lithography.

Fig. 6.8 shows measured gain for both polymer-based antenna element prototypes. The antenna element with higher percent alumina content demonstrates higher gain of 5.65 dBi compared to 4.85 dBi for the antenna element with lower alumina content. Based on Fig. 5.8, the average loss tangent of the 48 wt% SU-8 element in its -10 dB bandwidth is 0.012 which is less than half the loss tangent of the SU8-38 wt% element, and is responsible for the higher gain.

For comparison, a conventional non-lithographically fabricated ceramic DRA with dielectric constant of 10.2 is also measured. All the feeding parameters are the same as the previous antenna, except the slot dimension which is 3.2 mm × 0.7 mm in this case. The measured and simulated reflection coefficients are shown in Fig 6.9. The -10 dB impedance bandwidth of 9% is from 19.0 GHz to 20.7 GHz and agrees well with the simulation.

To ensure the functionality of the proposed polymer-based antenna, its radiation patterns are simulated and measured at the resonant frequency of the

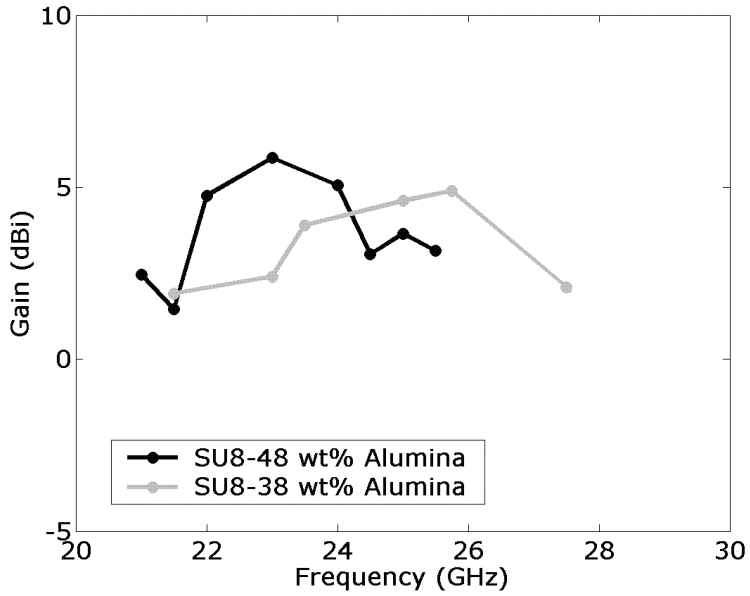

Fig. 6.8. Measured gain as a function of frequency for the X-ray resist-ceramic microcomposite antenna elements.

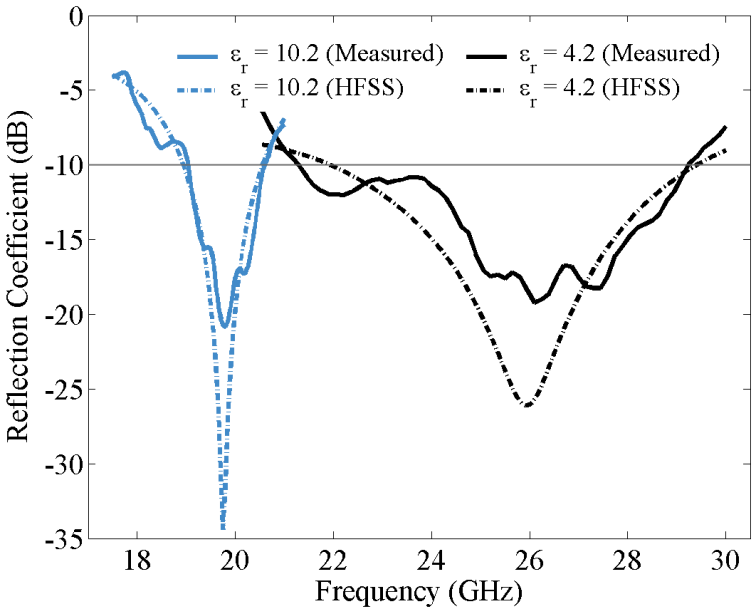

Fig. 6.9. Measured and simulated reflection coefficients of fabricated slot-coupled antennas. ($A \times B \times h = 5.7 \times 5.7 \times 2$ mm, $\Delta L \approx 1$ mm)

antenna. Fig. 6.10(a) and (b) show the radiation patterns at H-plane and E-plane. Low cross polarization levels are achieved for both cases. Symmetric and stable radiation patterns are observed in the H (xz)-plane while the slight asymmetry of

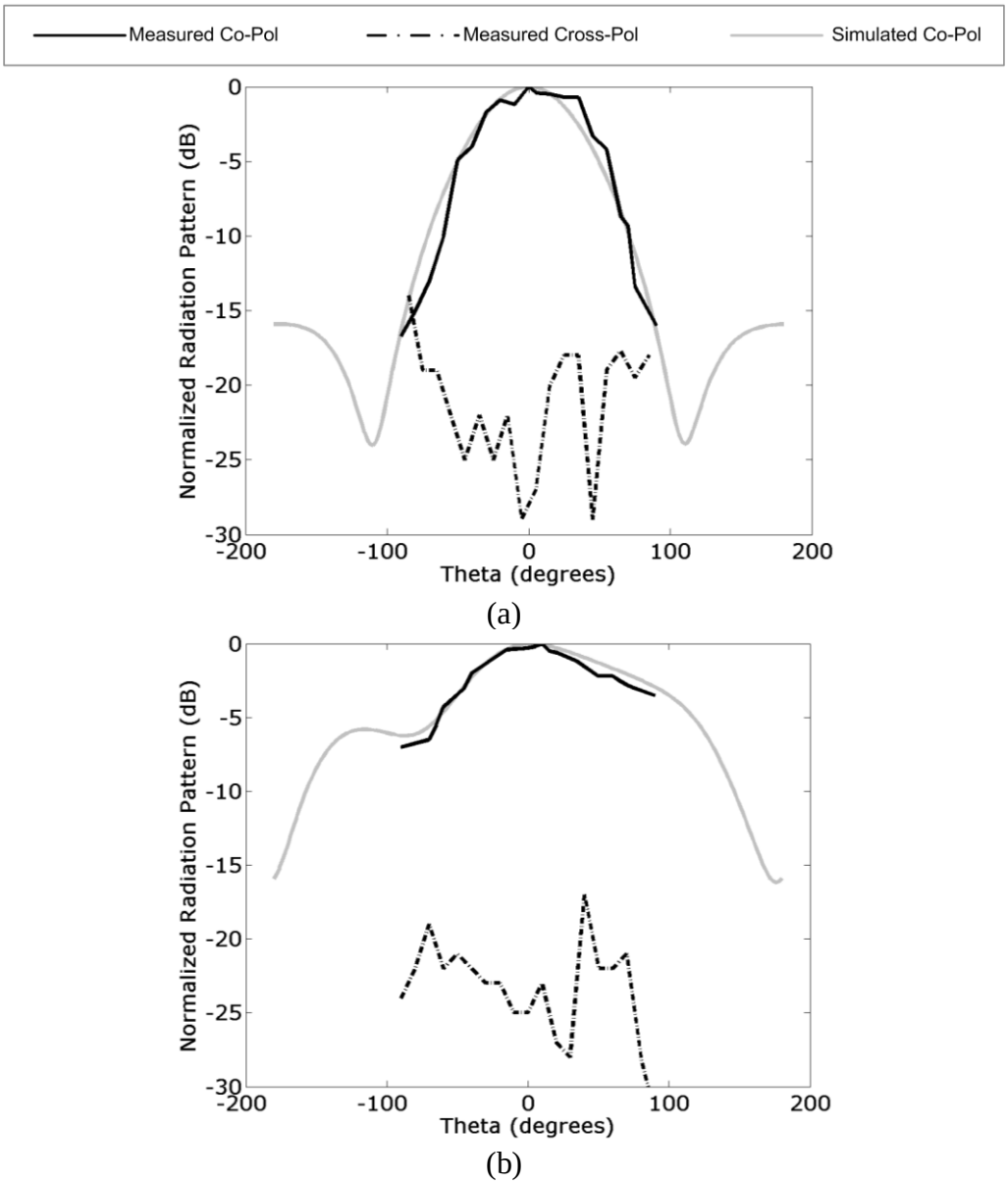

Fig. 6.10. Measured and simulated radiation patterns of the polymer-based slot-fed antenna structure. (a) H (xz)-plane at 26.1 GHz; (b) E (yz)-plane at 26.1 GHz.

the E (yz)-plane is primarily due to the small size of the ground plane, and shadowing from the microstrip feedline, connectors, and cables. The measured antenna gain at 26.1 GHz frequency is about 4.9 dBi.

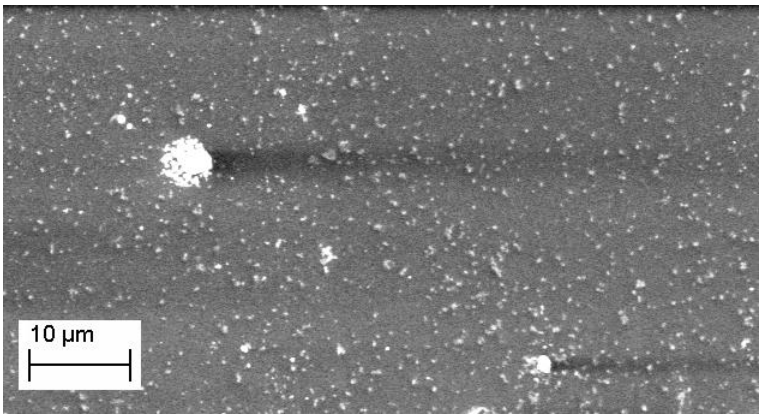

Fig. 6.11. SEM picture of the top surface of the hardened SU-8/alumina composite (38 weight percent micropowder) after X-ray exposure. The white alumina particles are distributed in the gray SU-8.

6.3 Microcomposite Strip-Fed Antennas

In this section, the theoretical achievements in Section 3.4 are utilized to fabricate a strip-fed microcomposite antenna with multimode operation [27]. The effect of the vertical strip on antenna miniaturization is investigated and antenna performance and improvements on fabrication process are discussed.

6.3.1 Prototype Preparation

A modified X-ray resist with 62 weight percent SU-8 and 38 weight percent alumina micropowder is used to realize the low permittivity strip-fed DRA. Alumina micropowder (with mean particle diameter of 0.8 microns) was mixed with SU-8(10) and stirred for about 1 hour. The resulting SU-8/alumina composite was irradiated for 18 minutes at the Angstroemquelle Karlsruhe (ANKA) electron storage ring, beamline Litho 2, using a bottom dose deposition of 200 J/cm^3. The layer was immediately developed to create the final structures. Fig. 6.11 shows the distribution of micropowders at the top surface of the hardened composite. A fairly homogeneous composite is produced; however, several agglomerations of the ceramic particles with size of a few microns are observed. It is also expected that the vertical particle distribution through the composite is not strictly constant, due to sedimentation of the heavier alumina

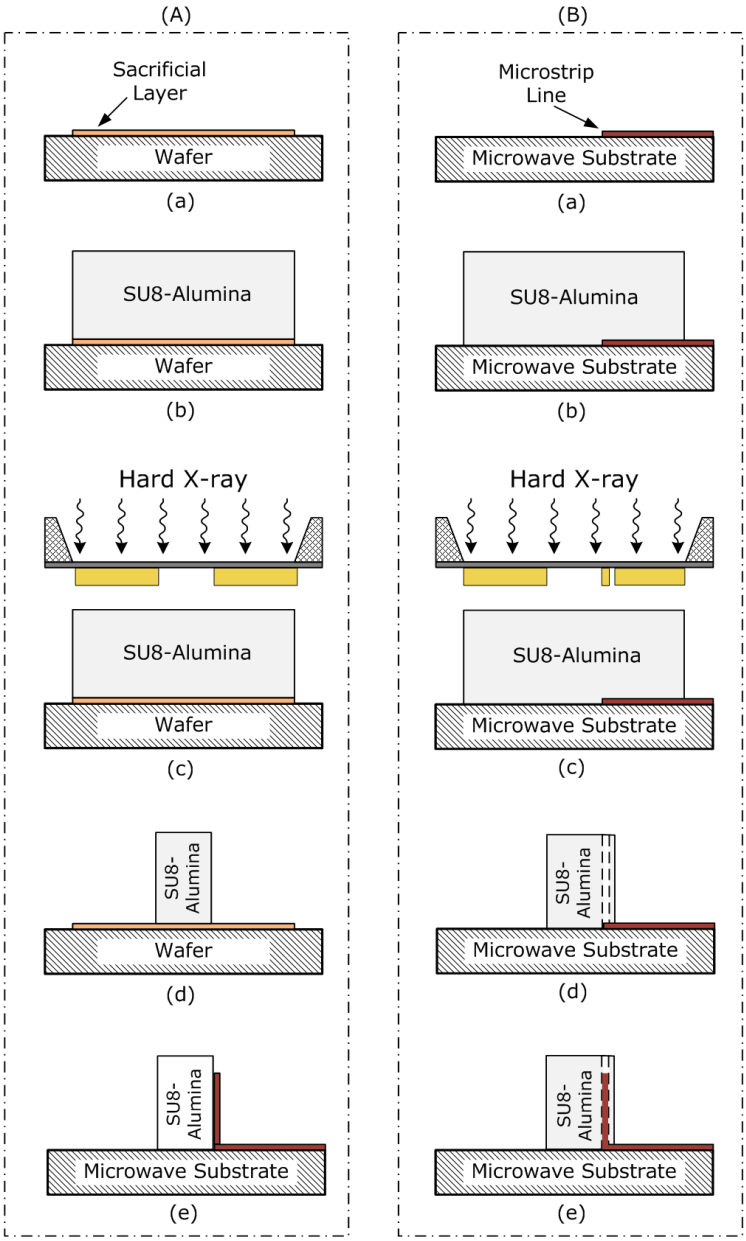

Fig. 6.12. (A) Summary of the fabrication process: (a) 100 μm polyimide sacrificial layer is applied on the substrate; (b) multiple casting of ceramic composite followed by baking at 95°C; (c) Deep X-ray exposure of resist through an X-ray mask; (d) development at room temperature for 30 minutes; (e) release of the structure due to the low adhesion of polyimide foil, gluing of the structure on the microwave substrate with microstrip line, and taping the vertical strip.
(B) Modified process for very small or complicated structures, integrated circuits or array configurations, and industrial batch fabrication: (a) preparing the feedline on the microwave substrate using UV lithography; (b), (c), and (d) are similar to the steps in block (A); (e) creation of the vertical strip with controlled length and shape using electroplating.

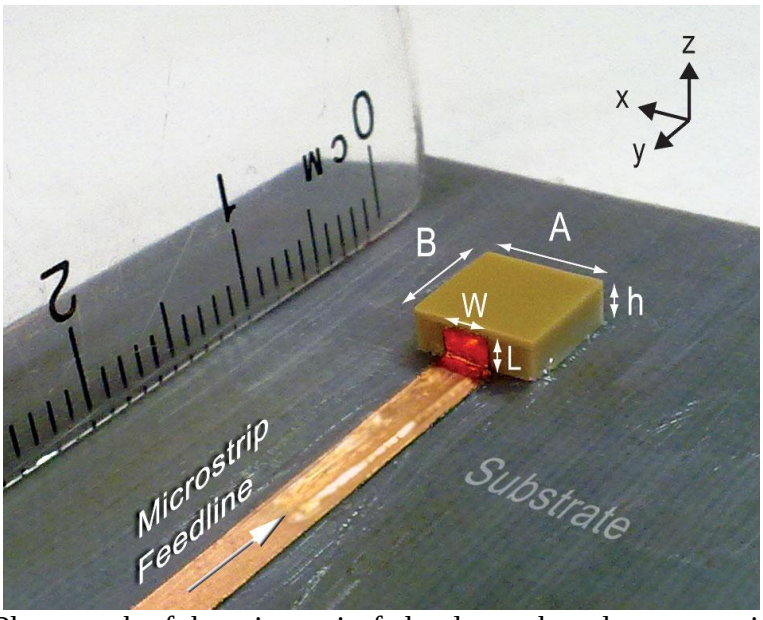

Fig. 6.13. Photograph of the microstrip-fed polymer-based antenna with a vertical open-ended strip. The structure is made using deep X-ray lithography fabrication.

particles. Detailed investigations on this property have yet to be performed, although a varying dielectric constant throughout the height could potentially enhance the performance, as in the case of multi-layer DRA structures. A summary of the fabrication procedure is depicted in Fig. 6.12, block (A). More details on deep X-ray lithography fabrication of polymer-ceramic microcomposites and their structural quality can be found in Chapter 4. The dielectric constant and loss tangent of the SU-8/alumina microcomposite are measured using the two-layer microstrip ring resonator technique and the results are shown in Figs. 5.7 and 5.8.

After X-ray lithography, development, and post-baking processes, the structure is released from the wafer (usually silicon) using the sacrificial carbon layer and mounted for testing on a 0.787-mm thick Taconic TLY-5 microwave substrate (ε_r = 2.2, $tan\ \delta_e$ = 0.0009 at 10 GHz) using RTV silicone adhesive sealant. The 50 Ω microstrip line, fabricated on a 30 mm × 30 mm ground plane, is 2.4 mm wide. The polymer-based rectangular DRA with dimensions of 5.7 mm × 5.7 mm × 2.0 mm is connected by a $L \times W$ = 1.5 mm × 2.4 mm vertical open-ended strip to the

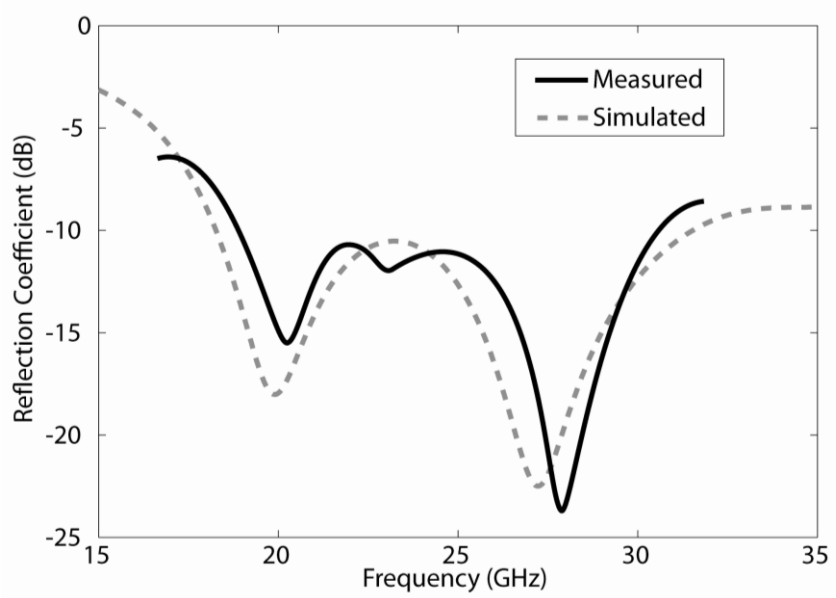

Fig. 6.14. Simulated and measured reflection coefficient of the prototype antenna. ($A \times B \times h$ = 5.7 × 5.7 × 2 mm, L = 1.5 mm, W = 2.4 mm)

microstrip line. Fig. 6.13 shows a photograph of the antenna configuration. The antenna, mounted on the universal substrate test fixture WK-3001-G from Inter-continental Microwave, is connected to an Agilent 8722ES vector network analyzer using a 2.4 mm HP 85133 flexible test cable to measure the reflection coefficient.

6.3.2 Measurement Results

The measured and HFSS^{TM} simulated reflection coefficients are shown in Fig. 6.14, where reasonable agreement between experiment and simulation is achieved. Dual-mode operation is due to the excitation of TE^{x}_{111} (dominant mode) and TE^{x}_{131}, as discussed in Section 3.4. It is found that the measured and simulated -10 dB impedance bandwidths of the antenna are from 18.8 GHz to 30.7 GHz and 18.3 GHz to 31.5 GHz, i.e. 48% and 53%, respectively.

Far-field radiation patterns of the fabricated antenna are measured and simulated at both TE^{x}_{111} and TE^{x}_{131} resonant frequencies. Figure 6.15 shows the results at *H* (*xz*) and *E* (*yz*) planes. The *H*-plane patterns are symmetrical about the broadside direction. The *E*-plane patterns are slightly tilted due to the small size of the

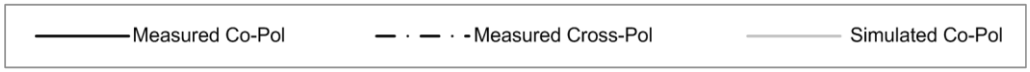

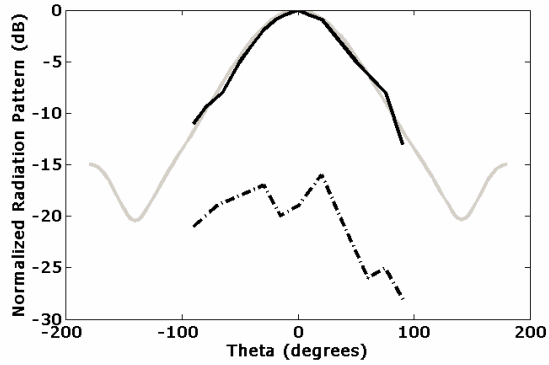

(a)

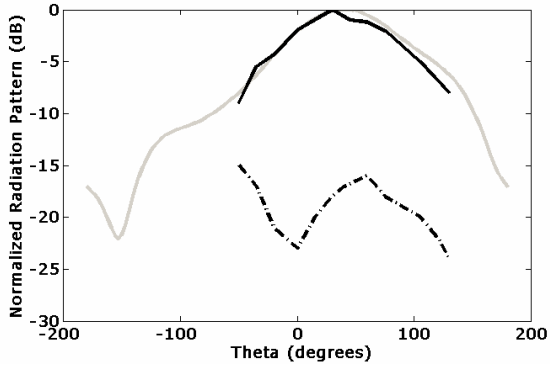

(b)

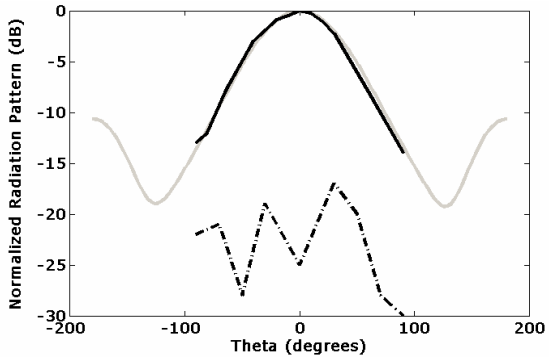

(c)

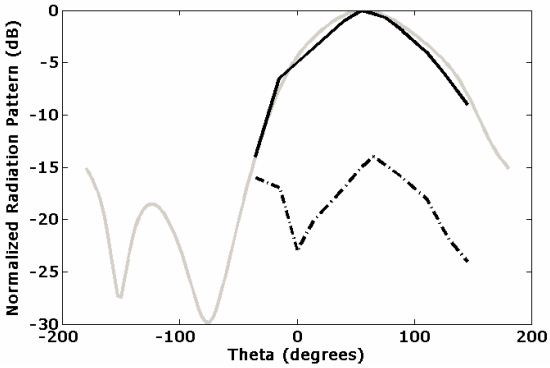

(d)

Fig. 6.15. Radiation patterns of the polymer-based antenna. (a) H (xz)-plane at 20.0 GHz (b) E (yz)-plane at 20.0 GHz (c) H (xz)-plane at 27.0 GHz (d) E (yz)-plane at 27.0 GHz.

Table 6.1 Comparison of theoretical and experimental resonant frequencies of the polymer-based resonator antenna.

Mode	Theory (DWM)	Simulated (HFSS^{TM})		Measured		Equivalent Dimensions (mm)	Size Reduction (%)
	Freq. (GHz)	Freq. (GHz)	Deviation (%)	Freq. (GHz)	Deviation (%)		
TE^{x}_{111}	24.2	20.0	-17.4	20.2	-16.5	5.7×12×2	52
TE^{x}_{131}	43.9	27.4	-37.6	27.8	-36.7		

ground plane and asymmetry of the structure with respect to the *xz* plane and the launch connectors and cables. The 3 dB beamwidths of the *H* and *E* plane patterns are 80 and 100 degrees for the first resonant mode at 20 GHz and 75 and 90 degrees for the second resonant mode at 27 GHz, respectively. The cross-polarization levels are at least 13 dB below the corresponding co-polarization levels in the range of 3 dB beamwidth. The low cross-polarization levels are primarily due to the similar radiations of TE^{x}_{111} and TE^{x}_{131} modes and lack of vertical open-ended strip radiation which should have different radiation patterns than those of the photoresist-based antenna. The maximum gain at the lower and upper resonant frequencies is roughly 4.5 and 5.0 dBi, respectively. The radiation patterns have similar properties over the entire -10 dB impedance bandwidth of the antenna.

6.3.3 Discussions and Improvements

- Miniaturization

The measured and simulated resonant frequencies of the fabricated polymer-based antenna are compared with the theoretical results of the dielectric waveguide model. These values are depicted in Table 6.1. Excellent agreements (within 1.5% error) achieved between simulated and measured resonant frequencies are in part due to the lithography fabrication of the structure which results in precise structural quality. On the other hand, the measured resonant frequencies are about 17% and 37% lower than those of theoretical frequencies of DWM model for the first and second resonant modes, respectively. This is mainly due to the

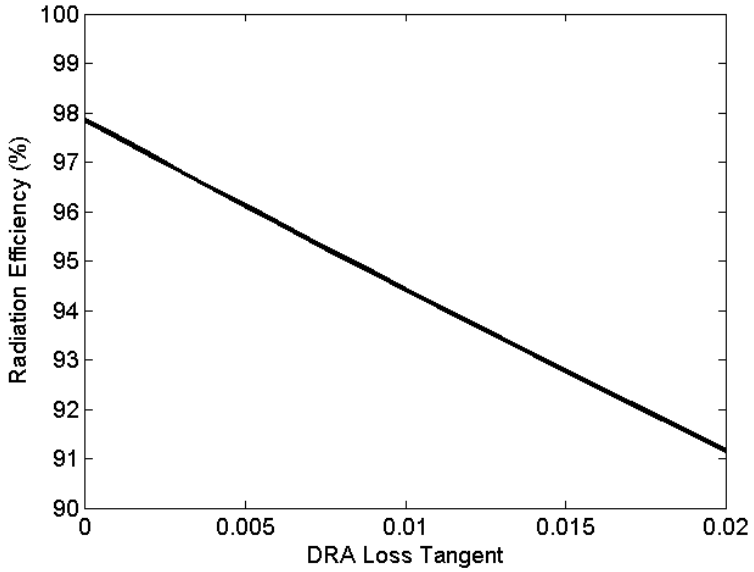

Fig. 6.16. Simulated radiation efficiency of the strip-fed DRA with different dielectric loss tangents. ($A \times B \times h$ = 5.7 × 5.7 × 2 mm, L = 1.5 mm, W = 2.4 mm)

existence of the wide open-ended strip on the sidewall of the antenna changing the effective dimensions of the polymer-based resonator. When the antenna dimensions are corrected in the theoretical model to match the results with measurements, it is found that the equivalent dimensions are 5.7 mm by 12 mm by 2.0 mm, showing 52% miniaturization due to existence of the metallic strip on the sidewall.

- Effects of Dielectric Loss on Antenna Efficiency

One of the benefits of using the ceramic composites as photodefinable materials is that their dielectric loss is lower than pure photoresists, as discussed in Chapter 5 for SU-8/alumina composites. However, it is still higher than sintered microwave ceramics. The impact of dielectric loss on antenna performance is investigated and shown in Figure 6.16 for the proposed strip-fed antenna. Antenna efficiency is derived by simulating the strip-fed antenna for different values of dielectric loss tangent ($0.0 < \tan \delta_e < 0.02$). In these simulations, it is supposed that the substrate is Taconic TLY5 with $\tan \delta_e = 0.0009$ and all metal components (i.e. microstrip line, vertical open-ended strip, and

ground plane) are annealed copper with conductivity of $\sigma = 5.8\times10^7$. The antenna efficiency varies from 98% for *tan δ* in the range for extremely low loss ceramics to 91% for *tan δ* in the range for SU-8 composites. It is worth mentioning that the radiation efficiency of the higher loss DRA is still better than the radiation efficiency of microstrip patch antennas which is typically around 80% [28].

- Fabrication Advantages and Corrections

Polymer-ceramic composites can introduce several advantages over pure ceramic materials for DRA fabrication. For instance, the softer nature of these composites simplifies conventional fabrication (e.g. machining and molding). Inhomogeneous distribution of ceramic powder can be used to make electrically anisotropic structures. Special features of polymers (e.g. flexibility [20]) can be utilized for particular applications. In this study, the X-ray sensitivity of a polymer was used to lithographically fabricate polymer-ceramic composite DRAs with multimode wideband characteristics. As shown in Fig. 6.12 block (A), the structures are shaped on a sacrificial layer, released from it, and mounted on a microwave substrate with microstrip line and the copper strip is taped to make the strip-fed polymer-based DRA. However, since SU-8 is hydrophobic and has low adhesion to metals, permanent bonding of the vertical strip to SU-8 is hard to realize. A future improved procedure, which can be more beneficial for very small structures in the sub millimeter range, complicated structures, array configurations, and/or industrial batch fabrication, is shown in Fig. 6.12 block (B). In this procedure, a narrow gap near the edge of the antenna is produced in the X-ray fabrication process (part (c) and (d)). This gap is then filled up to a specific height to produce the vertical open-ended strip. This procedure is performed using controlled metal electroplating with the microstrip line as a plating base to begin the process (part (e)). Electroplating of microstructures has been done for complicated structures with heights up to a few millimeters as the second step of the LIGA process [29].

6.4 Frame-Based Antennas

Since PMMA has poor X-ray sensitivity, it is difficult to shape very thick PMMA microcomposites directly by X-ray lithography. Although 1 mm-thick PMMA microcomposite structures with 20 wt% ceramic content were directly fabricated by X-ray lithography as discussed in Chapter 4, the exposure part took 7 hours with a very high bottom dose of 7000 J cm^{-3}. This experience could also be similar for sensitive SU-8 photoresist with high ceramic loading (more than 70 wt%) and therefore restricting the fabrication process to achieve better microwave properties. On the other hand, the permanent plastic mold, discussed in Section 4.3, can be one of the most promising methods to fabricate not only dielectric antenna structures but also other dielectric microwave components (e.g. filters) with precise features. In this method, a PMMA frame is fabricated by X-ray lithography and filled with a polymer microcomposite material. One of the advantages of this method is that the frame can be filled with non X-ray sensitive polymer composites as well. This provides more flexibility for different microwave applications. Since the plastic (PMMA) frame remains as part of the final structure, its effects on different output parameters of the application should be taken into account in the design procedure.

6.4.1 Effects of Polymer Frame on Antenna Properties

The effect of the PMMA frame for a special case in dielectric resonator applications is shown in Fig. 6.17. In this case the dielectric antenna element with PMMA frame is fed by a slot coupled feed circuit. The permittivity of the filling microcomposite material (ε_{r1}) is considered to be 4 or 10 while the loss tangent is kept constant at 0.01. The aspect ratio (height over frame thickness (h/t), see Fig. 4.6) of the PMMA frame is varied from 4 to 40 and its effects on impedance bandwidth, gain, efficiency, and resonant frequency are observed. It is found that due to the low permittivity of PMMA these effects are negligible for very high

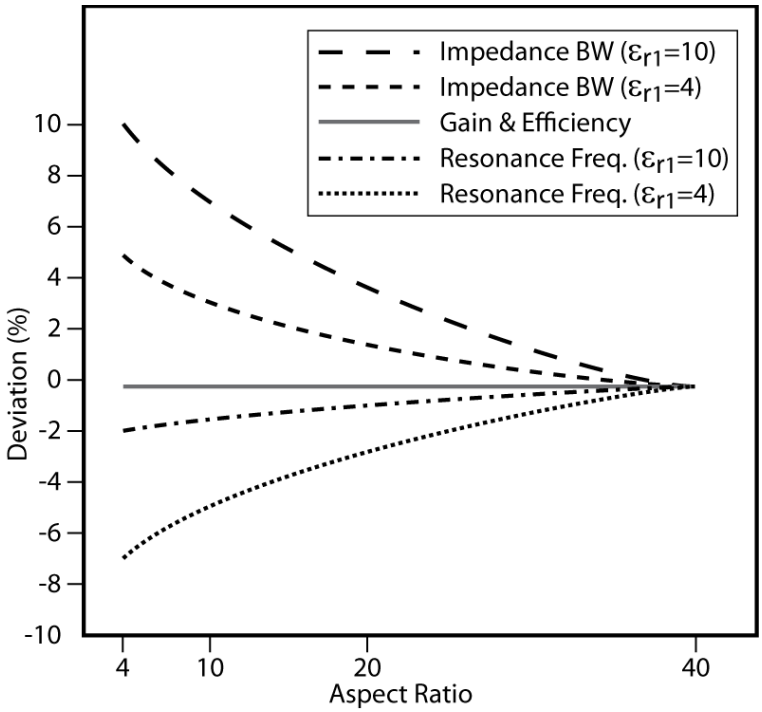

Fig. 6.17. Variation of impedance bandwidth, gain, efficiency, and resonant frequency of the frame-based microcomposite antenna elements with respect to the similar no frame elements for different aspect ratios (*h/t*) of the PMMA frame. The element height is kept constant at 2 mm. ε_{r1} is the relative permittivity of the composite filling material. ($A \times B \times h = 5.7 \times 5.7 \times 2$ mm, $\Delta L \approx 1$ mm)

aspect ratio frames. However when the aspect ratio decreases the frame becomes an important factor in some of the output parameters. For instance, impedance bandwidth increases by up to 10 percent and resonant frequency decreases by up to 7 percent for the aspect ratio of 4 with respect to the no-frame case. Furthermore, when the relative permittivity of the microcomposite increases from 4 to 10 it is realized that the impedance bandwidth of the antenna element shows more deviation. This can be mostly related to the fact that the effective permittivity of the frame-based structure with higher permittivity decreases more than that of the lower permittivity case with respect to their similar no-frame structures. Since the impedance bandwidth is proportional to the inverse permittivity, the bandwidth should increase more for the higher permittivity element. On the other hand, the resonant frequency of the higher permittivity element is less sensitive to change in dielectric constant and demonstrates less

deviation. High permittivity antenna elements are, however, very sensitive to dimension variations making the precise structuring of deep X-ray lithography very suitable. As shown in Fig. 6.17, gain and efficiency of the frame-based microcomposite elements remains steady. In fact, these parameters widely depend on the loss tangent of the filling microcomposite which is considered constant for all cases. Simulation results for other structures with different permittivities have confirmed the above conclusions.

6.4.2 Prototype Preparation

After sputtering of a 100 nm sacrificial carbon layer on a silicon substrate, a 1.8 mm-thick high molecular weight PMMA sheet is attached to the silicon wafer using a casting resin. The resin is a solution of 85% MMA and 15% PMMA which is mixed in the vacuum condition with very small portions of BPO, DMA, and MEMO. The PMMA sheet is exposed with a bottom dose of 4000 J/cm^3 and top to bottom ratio of 4 through a mask with rectangular frame patterns. The PMMA frame structures are produced after development of the wafer in GG-developer at room temperature for 12 hours. In the next step, a mixture of 48 wt% alumina micropowder and 52 wt% PMMA is injected into the frame using a JR 2200-JANOME robotic machine. Final polymerization is performed at 110 degree centigrade in a vacuum oven to further harden the structure.

The structure is released from the wafer and excited using a 1 mm by 4 mm slot on a 0.787 mm thick TLY5. The measured results are discussed in the following subsection.

6.4.3 Measurement Results

Fig. 6.18 shows the reflection coefficient of a fabricated sample along with the simulated results. The resonant frequency of the frame-based element is shifted by about 1 GHz from the similar no-frame element. Excellent agreement between the resonant frequencies of the simulated and measured frame-based antenna

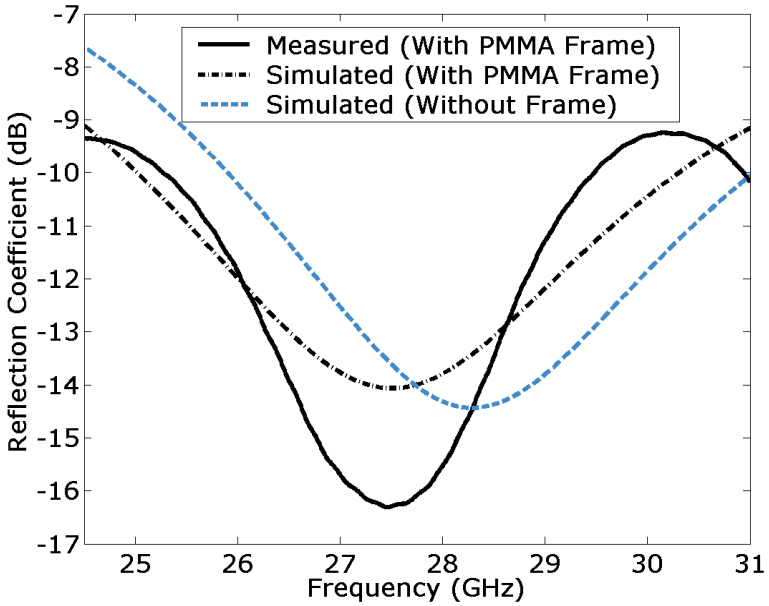

Fig. 6.18. Reflection coefficient of the PMMA-38 wt% alumina microcomposite antenna element with and without PMMA frame. The 500 micron-thick PMMA frame is 1800 microns high and fabricated by deep X-ray lithography processing. The cross section is 5.7 mm × 5.7 mm.

elements is achieved. The bandwidth is slightly changed for the frame-based structure with respect to the no-frame structure. The measured and simulated radiation patterns in the H and E planes at the frequency of minimum reflection (27.5 GHz) for the frame-based structure are shown in Fig. 6.19 (a) and (b). The frame-based antenna element radiates like a horizontal magnetic dipole in its dominant mode, similar to common dielectric antennas. The E-plane asymmetry which also exists in the no-frame case is primarily an effect of the presence of the feedline circuit structure and the small size of the ground plane and is intensified in the measured results by the connectors and cables. The gain at 27.5 GHz frequency is roughly 5.85 dBi. This is about 1 dB higher than the gain for the SU8-38 wt% alumina element and also slightly above the gain for the SU8-48 wt% alumina element. This performance improvement is a result of the lower loss tangent of PMMA-38 wt% alumina (Fig. 5.11) which remains below 0.01 at the operating frequencies.

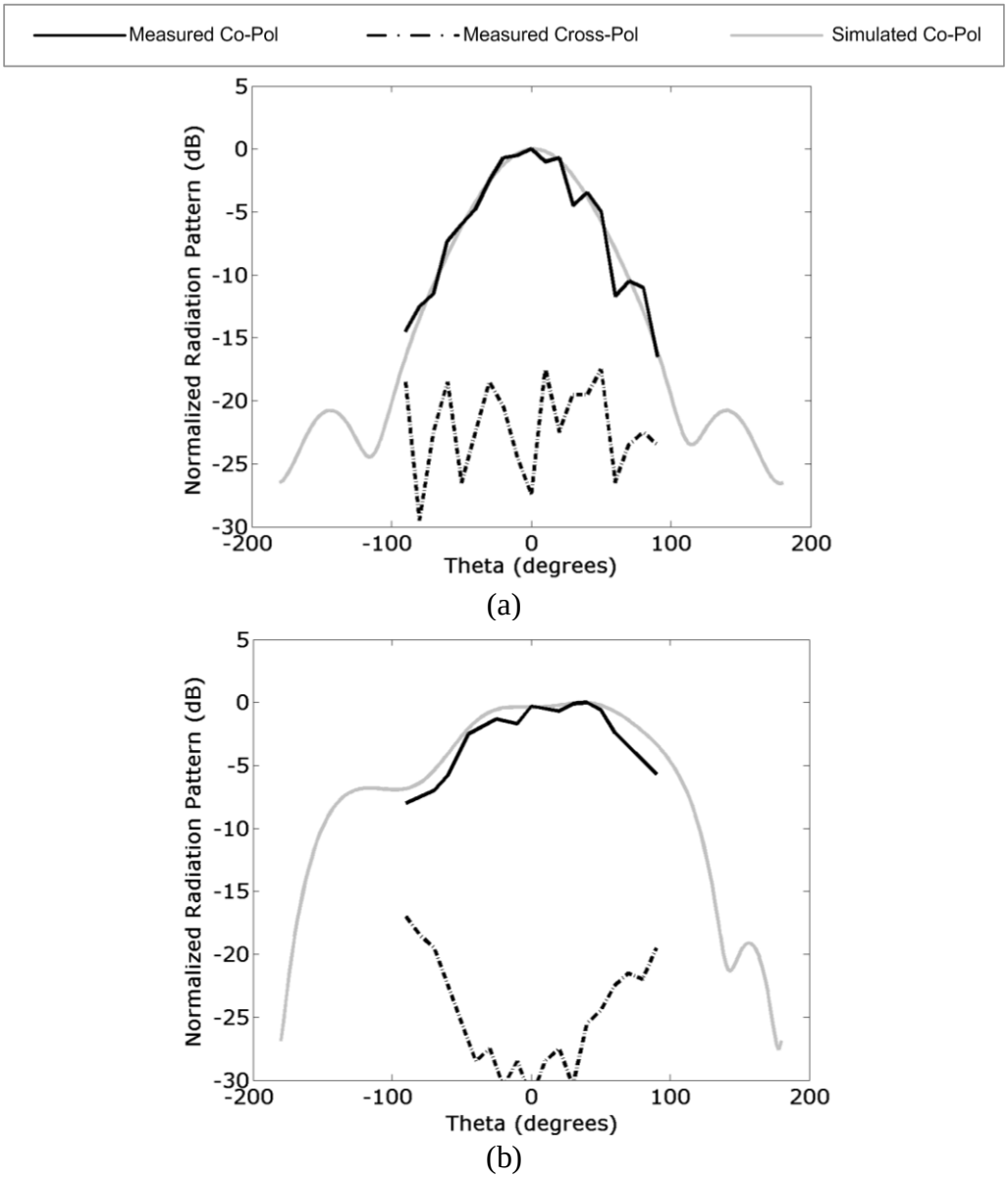

Fig. 6.19. Radiation patterns of the microcomposite antenna element with 500 micron-thick PMMA frame at 27.5 GHz. (a) H plane and (b) E plane.

6.5 Summary

Various photoresist-based polymer resonator antennas, including frame-based elements, are lithographically fabricated using different methods discussed in Chapter 4 and their characteristics are examined and analyzed based on measured electrical properties discussed in Chapter 5.

Pure SU-8 photoresist was investigated as a radiating material. The variational effect of electrical properties of the SU-8 and the substrate on the antenna performance was examined. It was shown that an SU-8 resonator antenna can achieve high radiation efficiency with proper selection of substrate material. More than 33 % impedance bandwidth was measured for the fabricated antenna.

A photoresist-based polymer resonator antenna fabricated by deep X-ray lithography and excited by a vertical open-ended strip was shown to have multimode wideband characteristics. The open-ended strip introduces about 50% miniaturization which can compensate the size expansion due to the very low permittivity of the material. The prototype antenna offers a -10 dB impedance bandwidth of 48% from 18.8 GHz to 30.7 GHz and gain in the range of 5 dBi.

Direct lithographic fabrication of a 48 wt% alumina SU-8 microcomposite slot-fed antenna demonstrated a decrease in resonant frequency from 26 GHz to 23 GHz and an increase in maximum gain by 0.8 dB compared to a 38 wt% element, due to the higher permittivity and lower dielectric loss of the microcomposite. To achieve higher structural quality, an indirect fabrication method with a permanent PMMA frame can be used to construct PMMA microcomposite antenna structures. Effects of the PMMA frame on antenna characteristics were investigated and it was shown that high aspect ratio frames, which can be fabricated with high precision by deep X-ray lithography, may have minimal impact of less than 1% on output antenna parameters.

References

[1] J. M. Shaw, J. D. Gelorme, N. C. LaBianca, W. E. Conley, and S. J. Holmes, "Negative photoresists for optical lithography," *IBM J. Res. Develop.*, vol. 41, no. 1/2, pp. 81-94, Jan. 1997.

[2] V. Nazmov, E. Reznikova, J. Mohr, A. Snigirev, I. Snigireva, S. Achenbach, and V. Saile, "Fabrication and preliminary testing of X-ray lenses in thick SU-8 resist layers," *Microsystem Tech.*, vol. 10, pp. 716-21, 2004.

[3] A.J. Gallant, D. Wood, J.A. Levitt, M. Kaliteevski, M.C. Petty, S. Brand, R.A. Abram, and J.M. Chamberlain, "The fabrication of high aspect ratio THz metamaterials," *Proc. Of Metamaterials for Microwave and (Sub) Millimetrewave Applications,* pp. 117-120, Sep. 2006.

[4] M. Nordström, D.A. Zauner, A. Boisen, and J. Hübner, "Single-mode waveguides with SU-8 polymer core and cladding for MOEMS applications," *J. of Lightwave Tech.,* vol. 25, no. 5, pp. 1284 – 1289, 2007.

[5] Y. Chen, C. Yang, Y. Cheng, H. Chen, Y. Chen, Y. Chu, and T. Hsieh, "10 Gbps multi-mode waveguide for optical interconnect," *Proc. of Electronic Components and Tech. Conf.*, pp. 1739-1743, May 2005.

[6] J. Carlier, K. Chuda, S. Arscott, V. Thomy, B. Verbeke, X. Coqueret, J.C. Camart, C. Druon, and P. Tabourier, "High pressure-resistant SU-8 microchannels for monolithic porous structure integration," *J. Micromech. Microeng.,* vol. 16, pp. 2211–2219, 2006.

[7] J. Yook and Y. Kwon, "Spiral inductors using polymer-core conductors," *IEEE Microw. Wireless Comp. Lett.*, vol. 17, no. 7, pp. 495 – 497, 2007.

[8] A. Ismail, M.S. Razalli, M.A. Mahdi, W.N.I. Darman, R.S.A. Abdullah, M.M. Isa, "Micromachined W-band integrated rectangular waveguide filter utilising SU-8," *Proc. of Asia-Pacific Microwave Conf.*, pp. 1-4, Dec. 2007.

[9] J.L. Hesler, K. Hui, R.K. Dahlstrom, R.M. Weikle, T.W. Crowe, C.M. Mann, and H. B. Wallace, "Analysis of an octagonal micromachined horn antenna for submillimeter-wave applications," *IEEE Trans. Antennas Propag.*, vol. 49, no. 6, pp. 997 – 1001, 2001.

[10] S. K. Pavuluri, C. H. Wang, and A. J. Sangster, "A high-performance aperture-coupled patch antenna supported by a micromachined polymer ring," *IEEE Antennas Wireless Propag. Lett.*, vol. 7, pp. 283 – 286, 2008.

[11] R. Osorio, "Micromachined transmission lines for microwave applications," Ph.D. dissertation, Univ. Freiburg, Germany, 2003.

[12] F. D. Mbairi and H. Hesselbom, "High frequency design and characterization of SU-8 based conductor backed coplanar waveguide transmission lines," *Proc. of Intl. Symp. on Advanced Packaging Material*, pp. 243-248, March 2005.

[13] J. R. Thorpe, D. P. Steenson, and R. E. Miles, "High frequency transmission line using micromachined polymer dielectric," *Electron. Lett.*, vol. 34, no. 12, pp. 1237-1238, June 1998.

[14] A. Rashidian, D. M. Klymyshyn, M. Tayfeh Aligodarz, M. Boerner, and J. Mohr, "SU-8 resonator antennas," *IEEE Int. Symp. on Antennas Propag. and USNC/URSI National Radio Science Meeting (AP-S/URSI)*, Toronto, July 2010.

[15] M. Boerner, F. Gosch, B. Matthis, J. Mohr, E. Reznikova, "Double sided X-ray transparent membranes for different HARMST applications," *8th Intern. Workshop on High-Aspect-Ratio Microstructure Technology*, pp. 15-16, Saskatoon, Canada, June 2009.

[16] A. Rashidian, M. Tayfeh Aligodarz, D. M. Klymyshyn, M. Boerner, and J. Mohr, "Photodefinable microcomposites for antenna applications," *IEEE Int. Symp. on Antennas Propag. and USNC/URSI National Radio Science Meeting (AP-S/URSI)*, Toronto, July 2010.

[17] R. K. Goyal, A. N. Tiwari. U. P. Mulik, and Y. S. Negi, "Novel high performance Al2O3/poly(ether ether ketone) nanocomposites for electronics applications," *Composites Science and Technology*, vol. 67, no. 9, pp 1802-12, July 2007.

[18] J. Borchardt, J. Alexander, and K. Slenes, "Ceramic-polymer composite for high energy density capacitors," *IEEE Pulsed Power Plasma Science Conference*, pp. 140, 2007.

[19] Y. Rao, J. Yue, and C. P. Wong, "Material characterization of high dielectric constant polymer-ceramic composite for embedded capacitor to RF

application," *Active and Passive Elec. Comp.*, vol. 25, no. 1, pp. 123-129, 2002.

[20] S. Koulouridis, G. Kiziltas, Z. Yijun D. J. Hansford, and J. L. Volakis, "Polymer-ceramic composites for microwave applications: fabrication and performance assessment," *IEEE Trans. Microw. Theory Tech.*, vol. 54, no. 12, pp. 4202-4208, Dec. 2006.

[21] G. Subodh, C. Pavithran, P. Mohanan, M. T. Sebastian, "PTFE/Sr2Ce2Ti5O16 polymer ceramic composites for electronic packaging applications," *Journal of the European Ceramic Society*, vol. 27, no. 8-9, pp. 3039-3044, 2007.

[22] H. L. W. Chan, "Smart 1-3 composites for ultrasonic transducer applications," *Proceedings of the IEEE Hong Kong Electron Devices Meeting*, pp 5-6, 2001.

[23] Y. Yashchyshyn and J. W. Modelski, "Rigorous analysis and investigations of the scan antennas on a ferroelectric substrate," *IEEE Trans. Microw. Theory Tech.*, vol. 53, no. 2, pp. 427-438, Feb. 2005.

[24] Y. Shirakata, N. Hidaka, M. Ishitsuka, A. Teramoto, and T. Ohmi, "Low-loss composite material containing fine Zn–Ni–Fe flakes for high-frequency applications," *IEEE Trans. Magn*, vol. 45, no. 10, pp. 4337-4340, Oct. 2009.

[25] P .B. A. Fechine, H. H. B. Rocha, R. S. T. Moretzsohn, J. C. Denardin, R. Lavı´n, and A. S. B. Sombra, "Study of a microwave ferrite resonator antenna, based on a ferrimagnetic composite $(Gd_3Fe_5O_{12})GdIG_X$–$(Y_3Fe_5O_{12})YIG_{1-X}$," *IET (IEE) Proceedings Microwaves, Antennas and Propagation*, vol. 3, no. 8, pp. 1191-1198, 2009.

[26] A. Mahanfar, C. Menon, and R.G. Vaughan, "Smart antennas using electro-active polymers for deformable parasitic elements," *IET (IEE) Electronics Letters*, vol. 44, no. 19, pp. 1113-1114, Sep. 2008.

[27] A. Rashidian, D. M. Klymyshyn, M. Tayfeh Aligodarz, M. Boerner, and J. Mohr, "Photoresist-based polymer resonator antennas: lithography fabrication,

strip-fed excitation, and multimode operation," to be published *IEEE AP Magazine*, Summer 2011.

[28] Q. Lai, G. Almpanis, C. Fumeaux, H. Benedickter, and R. Vahldieck, "Comparison of the Radiation Efficiency of the Dielectric Resonator Antenna and Microstrip Antenna at Ka Band," *IEEE Transactions on Antennas and Propagation*, vol. 56, no. 11, pp. 3589-3592, November 2008.

[29] W. Menz, J. Mohr, and O. Paul, *Microsystem Technology*, Weinheim, Wiley-VCH, 2001.

Chapter 7

Conclusion

7.1 Summary and Contributions

Over the past decade, vast investigations are performed by numerous research groups in the world to enhance the performance of DRAs. These antennas are resonant structures predominantly fabricated from sintered ceramics. DRAs, even without any modifications, show superior antenna characteristics over their metallic counterparts, but difficult fabrication due to constructing three dimensional structures from extremely hard ceramics. Most of modifications proposed by researchers have targeted complicated ceramic shapes which will be limited to prototype production since they are extremely costly and time consuming for high volume commercial applications. In the current research, improvements were achieved based on simple structures and/or soft materials (e.g. polymers) to make these antennas more applicable. Besides improving properties of dielectric resonator antennas, the goal of this dissertation was to investigate feasibility of X-ray lithography in batch fabrication of dielectric antenna structures.

Different approaches were examined to improve the antenna characteristics. Microstrip-fed high-permittivity high-aspect-ratio DRAs with dual-mode characteristics were presented. The two resonance modes were merged with proper design for bandwidth optimization. The nearly identical radiation characteristic of these modes allows preservation of the radiation patterns and polarization over the entire bandwidth. These antennas show a bandwidth approximately 2 times more than and a volume 2 times less than a conventional

DRA with dielectric constant of 10. Using a proper design procedure, enhancements in impedance bandwidth may be also achieved by two segmented DRA techniques. Several prototypes of high aspect ratio and two segmented DRAs were fabricated, tested, and compared to each other in various aspects. More than 70 percent cross section miniaturization and 50 percent volume miniaturization, along with wideband operation of high aspect ratio structures make them a strong alternative for array applications.

It was shown that low permittivity (polymer-based) resonator structures with permittivity as low as 4 can be utilized as wideband antennas with various fabrication advantages. Resonant frequency and impedance bandwidth of DRAs in the polymer region ($3 < \varepsilon_r < 5$) were discussed and compared with higher permittivity areas. Slot-coupled excitation was used to feed the low permittivity resonators and realize polymer-based resonator antennas.

A polymer-based resonator antenna excited by a vertical open-ended strip was shown to have multimode wideband characteristics. It was observed that the open-ended strip has four important effects on the polymer-based antenna. First, it enables effective excitation of the very low permittivity (as low as 4) material which may be difficult using other excitation methods. Second, it removes unwanted even modes (i.e. TE^{x}_{121}, TE^{x}_{141}, etc.) to preserve stable radiation patterns and low cross polarization levels. Third, it introduces a new degree of freedom for the antenna designer to adjust the second resonant frequency to achieve the desirable coupling and bandwidth, without significant effect on the first resonant frequency. Last but not least, it introduces about 50% miniaturization which can compensate the size expansion due to the very low permittivity of the material.

The possibility of utilizing softer materials like polymers as very low permittivity dielectrics in the fabrication of millimetre-wave DRAs facilitates simple fabrication processes for conventional structures, and also enables fabrication of small structures with fine features and complex geometries through

lithographic batch fabrication. Besides, numerous polymer composites (e.g. ceramic-polymer composites) having exceptional properties can be involved in the process to fulfill special requirements for different applications.

High structural quality photoresist and photoresist composite antennas were constructed using three different procedures of deep X-ray lithography fabrication. In the first fabrication method, the antenna structures are constructed using an X-ray exposure of SU-8 composites while in the second and third methods a very precise plastic (PMMA) frame, fabricated by X-ray lithography, was filled with composite polymers. Further simplification was performed in the third method by eliminating the demolding step and consequently keeping the plastic frame in the final structure. The quality of the structures was investigated by SEM micrographs.

A novel approach based on the ring resonator technique in a multilayer microstrip configuration was presented to measure the dielectric constant and loss tangent of photoresist microcomposites from 2 GHz to 40 GHz. The main advantage of the proposed technique was in its simplicity for use with a wide variety of prepared samples in a non-destructive way. By fabricating only one ring resonator, one can measure electrical properties of as many materials as desired. Using a few ring resonators, the electrical properties of the samples can be measured at numerous points over a broad frequency range. This can also be used to increase the reliability of the results when the measured points for different rings coincide in frequency. The method is not specific to sample thickness and is capable of measuring test slabs with any thickness and dimension as long as the sample completely covers the superimposed ring. There is no need for metalizing the samples under test to measure their electrical properties. This is especially important with specific materials that are difficult to metalize, for instance due to low adhesion (e.g. various polymer materials). Besides, metalization and circuit fabrication on each slab (which is required for the stripline and direct microstripline methods) add several more steps to the already complicated

fabrication process. Complex and inaccurate equations to calculate the conductor and radiation losses are removed in the proposed method since they do not introduce any significant error. They appear almost identical before and after slab insertion on the microstrip ring resonator circuits, as shown in Fig. 5.12, and therefore cancel each other out. The conductor loss has a great impact on stripline and direct microstrip methods especially in higher microwave frequencies. In the direct microstripline case the radiation loss must be calculated as well, which is not only significant at high frequencies, but also difficult to calculate theoretically. The proposed technique can also be used to measure materials in non-substrate forms such as powders and liquids which cannot be measured using stripline and direct microstrip methods.

SU-8 photoresist was investigated as a radiating material. The lithographic fabrication process was utilized to fabricate 2 mm-thick SU-8 resonator antenna structures. The variational effect of electrical properties of the SU-8 and the substrate on the antenna performance was examined. It was shown that an SU-8 resonator antenna can achieve high radiation efficiency (more than 90 percent) with proper selection of substrate material. More than 33 % impedance bandwidth was measured for the fabricated antenna.

Alumina micropowder (up to 48 wt%) was introduced to SU-8 and PMMA resists to modify the electrical properties (decrease the dielectric loss and increase the permittivity) and simultaneously maintain the X-ray sensitivity of the resulting microcomposite. A modified X-ray resist (62 wt% SU-8 and 38 wt% alumina micropowder) having a permittivity of ~4 was used to lithographically fabricate slot-fed photoresist microcomposite antenna structures. For comparison, a ceramic antenna with similar dimensions and permittivity of 10.2 was conventionally fabricated and measured. It was observed that the microcomposite antenna results in an impedance bandwidth which is 3.5 times more than the impedance bandwidth of the ceramic antenna. A 48 wt% alumina SU-8 microcomposite antenna element demonstrated a decrease in resonant frequency

from 26 GHz to 23 GHz and an increase in maximum gain by 0.8 dB compared to a 38 wt% element, due to the higher permittivity and lower dielectric loss of the microcomposite. A strip-fed photoresist composite antenna with square cross section presented a -10 dB impedance bandwidth of 48% from 18.8 GHz to 30.7 GHz and gain in the range of 5 dBi while the antenna with rectangular cross section could show 2:1 ultra wideband performance.

To achieve higher structural quality, the indirect fabrication method with a permanent PMMA frame was used to construct PMMA microcomposite structures. Effects of the PMMA frame on antenna characteristics were investigated and it was shown that high aspect ratio frames, which can be fabricated with high precision by deep X-ray lithography, may have minimal impact of less than 1% on output parameters.

7.2 Future Work

Application of a photoresist-based material enables deep X-ray lithography fabrication of the thick structure which leads to precise dimensions and high structural quality and facilitates the batch fabrication of complicated antenna structures. To demonstrate the superiority of this fabrication method, an X-ray mask with 20 micron thick gold absorbers in complicated patterns on a titanium membrane was designed and fabricated. Fig. 7.1 shows two kinds of structures, star and fractal shapes, fabricated using this newly developed mask. A picture of a 3×3 array resonator antenna is also shown in Fig. 7.2. Preliminary simulation results demonstrate promising improvements [1]. Future work can be concentrated on feeding these structures and implementing other photoresist-based microwave components for use in integrated microsystems providing filtering and feed array structures for these antenna elements. The low temperature processing of polymer composites will facilitate the integration process.

An additional topic of future investigation is the incorporation of a wide variety of composite materials in the microfabrication process. To achieve higher

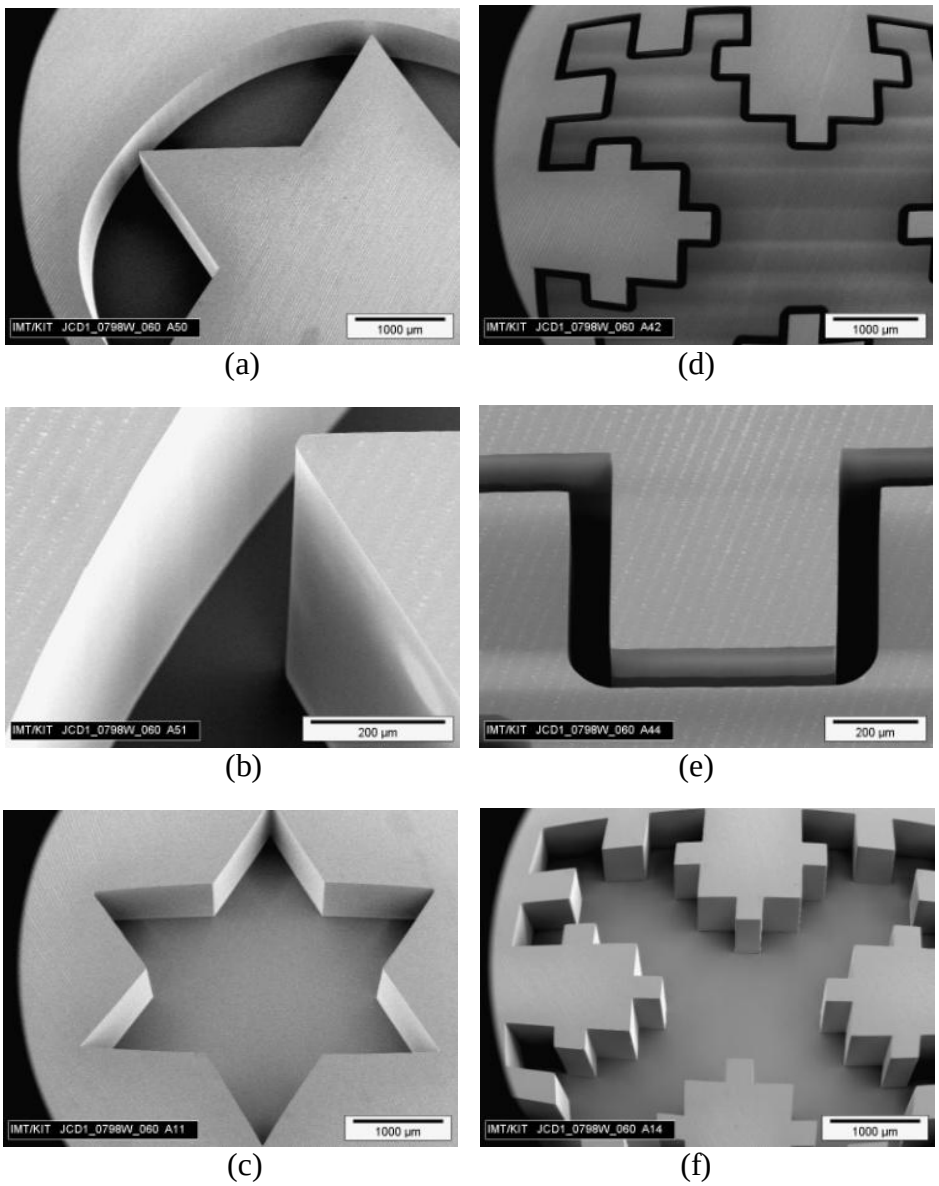

Fig. 7.1. SEM micrographs of polymer-based 1.8 mm-thick structures for future antenna applications fabricated with X-ray lithography. (a) star geometry; (b) details of the star; (c) negative star; (d) modified Koch curve fractal; (e) fractal details; (f) negative fractal.

permittivity microcomposites, ceramic powders with higher permittivities could be used, and lower dielectric loss might be obtained using pre-sintered ceramic powder [2]. Special attention will be paid to superior characteristics of nanomaterials to introduce a new class of microwave components. Particular fillers such as carbon nanotubes and CdS nanowires, active ferroelectric materials, and conductive polymers can be used to achieve extraordinary performances.

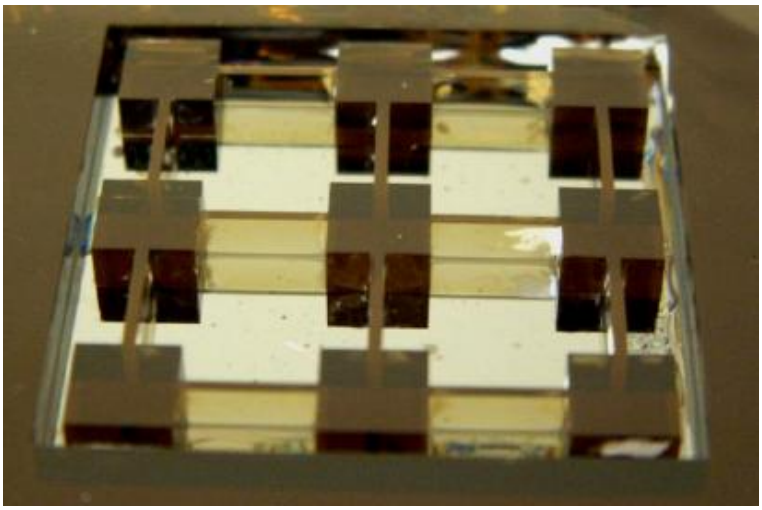

Fig. 7.2. 3×3 resonator array test structure fabricated in 2.3 mm thick SU-8 using a single deep X-ray lithography exposure.

Tuneability, photoactivity, and self-powering capability are just a few examples of what we can expect from such composites to make smart microwave devices. The biocompatibility of resulting polymer-based systems provides attractive applications not only in the telecommunications but also in flourishing fields of biomedical and environmental engineering.

References

[1] D. M. Klymyshyn, M. Tayfeh Aligodarz, A. Rashidian, M. Boerner, and J. Mohr, "Photoresist-based resonator array," *German Microwave Conference (GeMiC)*, Darmstadt, Germany, March 2011.

[2] Z. Taşdemir and G. Kızıltaş, "Flexible ceramic-polymer composite substrates with spatially variable dielectrics for miniaturized RF applications," *Proc. Material Research Society Symp.*, Warrendale, PA, USA, 2009.

List of Publications

Publications Related to this thesis

Journal Papers

[J1] A. Rashidian, D. M. Klymyshyn, M. Tayfeh Aligodarz, M. Boerner, and J. Mohr, "Photoresist-based polymer resonator antennas: lithography fabrication, strip-fed excitation, and multimode operation," to appear in *IEEE Antennas and Propagation Magazine*.

[J2] A. Rashidian, D. M. Klymyshyn, M. Tayfeh Aligodarz, M. Boerner, and J. Mohr, "Development of polymer-based dielectric resonator antennas for millimeter-wave applications," *Progress in Electromagnetics Research C (PIER C)*, vol. 13, pp. 203−216, 2010.

[J3] A. Rashidian, D. M. Klymyshyn, M. Boerner, and J. Mohr, "Deep x-ray lithography processing for batch fabrication of thick polymer-based antenna structures," *J. of Micromechanics and Microengineering*, 11 pp., vol. 20, no. 2, Feb. 2010 (IOP select paper).

[J4] A. Rashidian and D. M. Klymyshyn, "On the two segmented and high aspect ratio dielectric resonator antenna for bandwidth enhancement and miniaturization," *IEEE Transactions on Antennas and Propagation*, vol. 57, no. 9, pp. 2775-2780, Sep. 2009.

[J5] A. Rashidian and D. M. Klymyshyn, "Microstrip-fed high aspect ratio dielectric resonator antenna with dual-resonance, broadband characteristics," *IET (IEE) Electronics Letters*, vol. 45, no. 2, pp. 94-95, Jan. 2009.

[J6] A. Rashidian, D. M. Klymyshyn, M. Tayfeh Aligodarz, M. Boerner, and J. Mohr, "Characterization of photoresist-based microcomposites for polymer resonator antennas," to be submitted to *IEEE Transactions on Antennas and Propagation*.

Conference Papers

[C1] D. M. Klymyshyn, M. Tayfeh Aligodarz, A. Rashidian, M. Boerner, and J. Mohr, "Photoresist-based resonator array," *German Microwave Conf. (GeMiC)*, Darmstadt, Germany, March 2011.

[C2] A. Rashidian, M. Tayfeh Aligodarz, D. M. Klymyshyn, M. Boerner, and J. Mohr, "Photodefinable microcomposites for antenna applications," *IEEE Int. Symp. on Antennas Propag. and USNC/URSI National Radio Science Meeting (AP-S/URSI)*, Canada, July 2010.

[C3] A. Rashidian, D. M. Klymyshyn, M. Tayfeh Aligodarz, M. Boerner, and J. Mohr, "SU-8 resonator antennas," *IEEE Int. Symp. on Antennas Propag. and USNC/URSI National Radio Science Meeting (AP-S/URSI)*, Canada, July 2010.

[C4] A. Rashidian and D. M. Klymyshyn, "Very low permittivity slot-fed dielectric resonator antennas with improved bandwidth for millimeter-wave applications," *European Conference on Antennas and Propagations (EuCAP)*, Berlin, Germany, March 2009.

[C5] A. Rashidian and D. M. Klymyshyn, "A novel approach to enhance the bandwidth of miniaturized microstrip-fed dielectric resonator antennas," *European Conference on Antennas and Propagations (EuCAP)*, Berlin, Germany, March 2009.

[C6] A. Rashidian and D. M. Klymyshyn, "Strip-fed excitation of very low permittivity dielectric resonator antennas," *Asia-Pacific Microwave Conf. (APMC 2008)*, Hong Kong, Dec. 2008.